UNIVERSITÀ DEGLI STUDI DI SALERNO

DIPARTIMENTO DI SCIENZE ECONOMICHE E STATISTICHE

SCUOLA DOTTORALE INTERNAZIONALE "ANTONIO GENOVESI"

DOTTORATO DI RICERCA IN
INGEGNERIA ED ECONOMIA DELL'INNOVAZIONE

XI CICLO

TESI DI DOTTORATO

# DISK LASER WELDING OF METAL ALLOYS FOR AEROSPACE

## VITTORIO ALFIERI

| TUTOR | COORDINATORE |
|---|---|
| **Ch.mo Prof. Fabrizia Caiazzo** | **Ch.mo Prof. Alessandra Amendola** |

ANNO ACCADEMICO 2011/2012

# CONTENTS

PREFACE V

INDEX OF MAIN SYMBOLS IX

INDEX OF ABBREVIATIONS IX

**1 LASER WELDING 3**
**1.1** Introduction **3**
**1.2** Applications **4**
**1.3** Comparison with other welding technologies **4**
**1.4** Diagnostics in laser welding **6**
**1.5** Laser safety **7**
**1.6** Welding robots **8**

**2 LASER OPTICS AND QUALITY 11**
**2.1** Introduction **11**
**2.2** Principles of laser emission **11**
**2.3** Beam delivery systems **15**
**2.4** Resonator modes **15**
**2.5** Laser beam geometry **17**
  2.5.1 Rayleigh range **19**
  2.5.2 Beam dependence on the focusing optics **21**
**2.6** Beam quality **22**
**2.7** Laser efficiency **25**
**2.8** Thin disk laser concept **26**
  2.8.1 Architecture **27**
  2.8.2 Gain medium **28**
  2.8.3 Advantages **30**
  2.8.4 Disk laser vs fibre laser **32**

**3 PROCESSING DYNAMICS 35**
**3.1** Introduction **35**
**3.2** Laser welding modes **36**
**3.3** Key-hole instability **38**
**3.4** Gas supply **41**
  3.4.1 Gas choice **43**
  3.4.2 Gas supply devices **44**
**3.5** Focusing **45**
**3.6** Beam angle **46**

**4 BEAD CHARACTERIZATION 49**
**4.1** Introduction **49**
**4.2** Seam geometry **49**
**4.3** Non destructive tests **51**

**4.4** Sample preparation **52**
4.4.1 Cutting **52**
4.4.2 Mounting **53**
4.4.3 Mechanical preparation **54**
4.4.4 Chemical etching **55**
**4.5** Imperfect shape and dimensions **56**
**4.6** Assessment of the heat affected zone **58**
**4.7** Energy dispersive spectrometry **59**
**4.8** Tensile tests **60**

**5 MODELING AND OPTIMIZATION 63**
**5.1** Introduction **63**
**5.2** DOE principles **63**
**5.3** Testing schemes **65**
**5.4** Regression models **67**
**5.5** Desirability **68**

**6 WELDING ALUMINUM ALLOY 2024 73**
**6.1** Introduction **73**
**6.2** Aluminum welding **74**
**6.3** Experimental procedure **74**
**6.4** System set-up **75**
**6.5** General issues in laser-material interactions **77**
**6.6** Porosity evolution **79**
6.6.1 Thermal input dependence **84**
6.6.2 Defocusing effect **85**
**6.7** Softening in the fused zone **86**
**6.8** Optimization of butt welded joints **88**
**6.9** Optimization of lap welded joints **94**
**6.10** Conclusions **100**

**7 WELDING TITANIUM ALLOY TI-6AL-4V 103**
**7.1** Introduction **103**
**7.2** Arrangement of the experimental plan **104**
**7.3** Experimental details **105**
**7.4** Results and discussion **106**
7.4.1 Micro structure **108**
7.4.2 Main effects **110**
**7.5** Optimization of the responses **112**
**7.6** Conclusions **114**

**8 DISSIMILAR WELDING HAYNES + INCONEL 117**
**8.1** Introduction **117**
**8.2** Super alloys welding **119**
**8.3** Arrangement of the experimental plan **120**
**8.4** Experimental details **122**

8.4.1 Pre welding procedures **122**
8.4.2 Post welding procedures **123**
**8.5** Results and discussion **124**
**8.6** Optimization of the responses **127**
8.6.1 Modeling the response variables **127**
8.6.2 Constraint criteria for optimization **128**
**8.7** Mechanical assessment of the optimal processing condition **129**
8.7.1 Vickers micro hardness tests **130**
8.7.2 Tensile tests **131**
**8.8** Conclusions **133**

**9 DISSIMILAR WELDING HASTELLOY + RENÉ 135**
**9.1** Introduction **135**
**9.2** Arrangement of the experimental plan **136**
**9.3** Experimental details **137**
**9.4** Results and discussion **139**
**9.5** Optimization of the responses **141**
**9.6** Vickers micro hardness tests **144**
**9.7** Conclusions **144**

**ACKNOWLEDGEMENTS 147**

**REFERENCES 149**

# PREFACE

*Laser welding is the logical processing solution to accomplish different needs. Improvements at the design stage are actually aimed to remove any mechanical fastening, thus moving towards a technology which would not increase the joint thickness; moreover, a number of benefits in comparison with conventional welding methods are provided when considering laser beams, since deep penetration is achieved and the energy is effectively used where needed, thus melting the interface to be joined rather than excessively heating up the base metal, which would suffer from thermal distortion and degradation of metallurgical properties otherwise.*

*Further advantages are achieved in laser welding with thin disk sources, since high output power, high efficiency and good beam quality are simultaneously delivered, unlike traditional laser systems; costs are significantly reduced in comparison with lamp-pumped laser systems. As a consequence, specific interest is shown in aerospace where strict specifications apply.*

*Nevertheless, a number of issues must be addressed, depending on the material to be welded, as many variables and sub processes concerning fusion and vaporization are involved in laser welding and a delicate balance between heating and cooling is in place within a spatially localized volume. Therefore, extensive studies are required to manage both the stability and the reproducibility of the overall process, before introducing any change in industrial environments. Methods, experimental results and discussions concerning laser welding of common metal alloys for aerospace are provided in this Ph.D. thesis.*

*A general view of applications and basic advantages of laser welding is first given, with mention to diagnostics and safety. Hence, the principles of laser emission are examined, with respect to the architecture of the sources, beam geometry, quality and efficiency, in order to better portray the benefits of a thin disk laser concept.*

*Processing dynamics of laser welding are explained afterward, referring to conduction and key-hole mode, instability, gas supply and leading governing parameters such as laser power, welding speed, defocusing and beam angle to be considered in the experimental work. Procedures are provided for proper bead characterization, from preliminary examinations including non destructive* *tests such as fluorescent penetrant inspections and radiographic tests, to sample preparation and eventual mechanical assessment in terms of tensile strength and Vickers micro hardness in the fused zone.*

*A straightforward description of the design of experiment approach and the response surface methodology is given, so to introduce the testing method to be taken, as well as the steps for data elaboration via statistical tools.*

*Hence, four case studies about metal aerospace alloys are presented and discussed in their common seam configuration: autogenous butt and overlapping welding of aluminum alloy 2024; autogenous butt welding of titanium alloy Ti-6Al-4V; dissimilar butt welding of Haynes 188 and Inconel 718; dissimilar overlapping welding of Hastelloy X and René 80. All of the welding tests were conducted at the Department of Industrial Engineering at the University of Salerno; a Trumpf Tru-Disk 2002 Yb:YAG disk-laser source with a BEO D70 focusing optics, moved by an ABB IRB 2004/16 robot was employed. When needed, additional tests for the purpose of specific bead characterization were conducted by Avio and Europea Microfusioni Aerospaziali.*

*As general procedure for each topic, the operating ranges to be examined are found via preliminary trials in combination with the existing literature on the subject. Then, special consideration is given to the processing set-up, the resulting bead profile, possible imperfections, defects and overall features; consistent constraint criteria for optimization of the responses are chosen on a case-by-case basis depending on materials and seam geometry and referring to international standards as well as customer specifications for quality compliance. Optimal combinations of the input welding parameters for actual industrial applications are eventually suggested, based on statistical tools of analysis. Convincing reasons are provided to give grounds to improvements in real applications. Moreover, based on the results, a proper device for bead shielding, to be conveniently adjusted depending on both geometry and materials to be welded has been designed, produced and patented (SA2012A000016).*

*As concerning aluminum welding, a comprehensive description is given for laser-related issues: reflectivity and thermal conductivity influence on the material response is illustrated; the porosity evolution is discussed with respect to thermal input and defocusing; a theory for softening in the fused zone is provided through energy dispersive spectrometry and estimations of* *magnesium content in the cross-section. Optimization is performed for butt configuration of 1.25 mm thick sheets; the discussion about the interactions among the governing factors is deepen with reference to overlapping welding.*

*With respect to titanium welding, optimization is performed for 3 mm thick butt welding; the resulting micro structure in the weld is discussed since it is thought to be closely related to the mechanical properties. In particular, special care is taken of the grain size as a function of the governing factors.*

*Dissimilar welding of super alloys is considered for gas turbine components; for this specific purpose, laser welding is expected to offer a valid alternative to arc and electron beam welding, whose weaknesses are pointed out. Given their actual application in the engine, Haynes 188 and Inconel 718 are examined in butt welding configuration, whilst an overlapping geometry is preferred for Hastelloy X and René 80. Considerable tolerances are matched, thus promoting the suggested range of the operating variables.*

## INDEX OF MAIN SYMBOLS

| | |
|---|---|
| Laser beam angle | $\alpha$ |
| Beam divergence angle | $\theta$ |
| Laser wavelength | $\lambda$ |
| Beam parameter product | $BPP$ |
| Bead crown width | $CW$ |
| Beam diameter | $D$ |
| Excessive penetration | $EP$ |
| Focus position | $f$ |
| Focal length of the collimating lens | $f_c$ |
| Focal length of the focusing lens | $f_f$ |
| Extent of the fused zone | $FZ$ |
| Beam irradiance | $I$ |
| Incompletely filled groove | $IFG$ |
| Misalignment | $M$ |
| Beam propagation parameter | $M^2$ |
| Bead neck width | $NW$ |
| Laser power | $P$ |
| Penetration depth | $PD$ |
| Reinforcement | $R$ |
| Root concavity | $RC$ |
| Bead root width | $RW$ |
| Sagging | $S$ |
| Shape-factor | $SF$ |
| Welding speed | $s$ |
| Shrinkage groove | $SG$ |
| Thickness to be welded | $t$ |
| Undercut | $UC$ |
| Rayleigh range | $z_h$ |

## INDEX OF ABBREVIATIONS

| | |
|---|---|
| Analysis of variance | ANOVA |
| Bead-on-plate | BOP |
| Central composite design | CCD |
| Design of experiment | DOE |
| Electron beam welding | EBW |
| Energy dispersive spectrometry | EDS |
| Fluorescent penetrant inspections | FPI |
| Heat affected zone | HAZ |
| Yttrium aluminum garnet | YAG |
| Response surface method | RSM |
| Radiographic tests | RT |
| Transverse electromagnetic mode | TEM |
| Ultimate tensile strength | UTS |

# DISK LASER WELDING
# OF METAL ALLOYS FOR AEROSPACE

# 1

# LASER WELDING

## 1.1 INTRODUCTION

New materials and new processing methods are progressively tested for aerospace in order to meet the challenges of innovation and reduction of operating costs, but extensive studies are needed before introducing any change in industrial environments.

Mechanical assembly are generally preferred because a reduction in waste material is achieved compared with a similar component which is alternatively processed via machining; this trend leads to shorter lead times, as well as lower buy-to-fly ratio, which is a measure of how much material is actually required to manufacture the final flying part. Moreover, joining technologies which do not increase the joint thickness are usually preferred, such that weight reduction is benefited [1]. Hence, improvements at the design stage are aimed to remove any mechanical fastening such riveting in order to introduce welded assemblies.

Laser welding is the logical processing solution to accomplish different needs. As for any other welding technology involving fusion of the materials to be joined, the objective is to create a liquid melted pool, allow it to grow and then to propagate through the solid interface, thus joining the components [2]. Nevertheless, specific issues must be addressed, depending on the material to be welded. For instance, when referring to common alloys systems for aerospace, it has been pointed out that laser welding is hindered by reflectivity and excessive fluidity as well as affected by tendency to porosity in the case of aluminum [3, 4]; brittle phase formation and segregation issues in the case of heat resistant super alloys [5]; oxidation and detrimental grain growth when improper welding rates are used in the case of titanium alloys [6].

### 1.2 APPLICATIONS

A really wide range of applications are regarded to be laser suitable [5]. Laser welding is employed indeed in joining gas turbines components for aerospace, transformer laminates, bimetallic saw blades, stamped mufflers, cooker tops, fire extinguisher cylinders, layered shaving blades, as well as heat-sensitive components such as heart pace-makers; hermetically sealing electronic capsules; repairing of nuclear boiler tubes from the inside; underwater joining. Special consideration has also been given to dissimilar welding, for either the purpose of joining aerospace components which are made of different materials due to machining and operating reasons, or reducing the overall weight of structures. As a result, an effective way to save rare metals is thus provided [7].

Nevertheless, tailored blank joining for car industry [8] is the largest relevant application for laser welding: the process was actually conceived in the eighties and is accepted as the way to handle pressed products. Moreover, when merely considering a car, a wide range of components such as airbag sensors, valve lifters, heat exchangers, gear wheels, torque converters, exhaust pipes, tanks and roof scams are welded via laser beams [5].

### 1.3 COMPARISON WITH OTHER WELDING TECHNOLOGIES

A number of benefits are provided by laser welding in comparison with conventional technologies. For instance, the process can be performed in remote locations or inside three-dimensional components from single side access, where the introduction of electrodes would be impossible. Furthermore, new opportunities are offered in autogenously joining difficult materials including, but not limited to, aluminum and magnesium alloys without the need for filler metal [2]; no pre heating, neither mechanical finishing are required [9]; increased processing speed is achieved and, as a consequence, productivity improves [10].

Advantages come from the primary feature of narrowly focusing the heat source to a very small area [11], in the order of few tenths of millimetres: local precision treatment and extremely high cooling rates are benefited, in the order of $10^4$ °C/s whilst a rate of $10^2$ °C/s results in tungsten inert gas welding [12]. Compared with slower processes, grounds are then given to further advantages in dissimilar welding which traditionally is only feasible for certain combinations of the base elements. Indeed, irrespective of the alloys being joined, the properties of different materials are generally difficult to be matched [13] and the formation of brittle intermetallics occurs. Higher cooling rates of laser welding can restrain the issue, such that wider ranges of combinations of metal alloys are offered [5].

Since the welding bead is rarely wide and deep penetration is achieved, it can be seen that the laser energy is effectively being used where required, thus melting the interface to be joined rather than excessively heating up the base metal in the surrounding area, which would suffer from thermal distortion and degradation of metallurgical properties otherwise [2, 9]. In order to give a quantitative description of this concept, the joining efficiency $\eta$ is defined as:

$$\eta = \frac{s \cdot t}{P} \tag{1.1}$$

which is not true efficiency, because $s$ is the laser transverse speed, $t$ is the thickness to be welded and $P$ is the incident power, so units of joined square millimetres per supplied joules result. The higher the joining efficiency, the less energy is spent in unnecessary heating which may produce heat affected zones or distortion. Typical values of joining efficiencies of different welding processes [5] are listed in **table 1.1**: resistance welding is by far the best in this respect because the energy is mainly generated at the high resistance interface to be welded. Nevertheless, both laser and electron beams are in a class by themselves; furthermore, joint access is easier and slighter environmental

**TABLE 1.1** – Joining efficiencies of common welding technologies

| Process | Approximate joining efficiency [$mm^2\ kJ^{-1}$] |
|---|---:|
| Oxy acetylene flame | 0.2 ÷ 0.5 |
| Tungsten inert gas | 0.8 ÷ 2 |
| Manual metal arc | 2 ÷ 3 |
| Submerged arc welding | 4 ÷ 10 |
| Laser beam | 15 ÷ 25 |
| Electron beam | 20 ÷ 30 |
| High frequency resistant welding | 65 ÷ 100 |

impact is produced in terms of noise and fume compared with resistance welding. Therefore, although equipment costs may significantly rise, laser and electron beams are known to play important roles for high quality joints in aerospace, military, power plants and automotive industries [14]: a specific comparison is then worth drawing.

Electron beam welding (EBW) relies on high speed electrons whose kinetic energy is turned into heat upon impact on the piece to be joined. Hence, the process has to be performed in vacuo to prevent energy dissipation of the electron beam [11], whilst laser beam is capable of being used at atmospheric pressure, thus resulting in simple fixturing and reduced lead time [2, 11]. Moreover, X-rays emission arises in EBW and, when specifically considering metal welding, electromagnetic phenomena can produce beam wander affecting stability during material melting [5]; this is obviously excluded in laser welding, with far less tendency to incomplete fusion and spattering [11].

Nevertheless, laser welding systems are usually of higher capital cost compared with conventional welding devices; operating costs can further grow for applications where large flow of expensive shielding gases is required. High production rates and quality are then essential for the system to be competitive and cost effective [2]; in this case, an overall reduction of operating costs ranging from 40 to 50% is estimated in comparison with EBW.

### 1.4 DIAGNOSTICS IN LASER WELDING

Laser interaction is capable of being manipulated in order to optimize welding. For this purpose, computer control for laser power have been developed. The basic idea is that a variety of signals containing information about the process are generated during the process itself. Extraction and hence recognition of signals is the key to monitoring and adapting control [15, 16]. Actually, each single signal component is adaptable by individual programming via computer numeric controlling system.

With feedback from an optical, plasma or acoustic monitoring system, real time adjustments are hence made to the power level in order to compensate possible changes in the welding conditions. Imperfections which could result in rejection at quality checks are thus fixed. Such closed loop controllers rely on excellent understanding of the process; optimal welding is performed in turn without any operator intervention.

The most simple monitoring procedure is conducted visually, referring to direct imaging of the weld pool and the surrounding area on the work-piece during the process. Oscillations of the weld pool take the form of surface waves of appreciable amplitude, ranging between 200 and 300 Hz; referring to steel welding, frequency has been proven to dramatically increase to one order of magnitude more when unstable conditions are in place [2].

### 1.5 LASER SAFETY

Laser devices are potentially dangerous when improperly used [11, 9] because exposure under certain circumstances may result in damage for the human body. Classes of lasers, depending on both the power and the wavelength of the emitted radiation, are hence defined in ANSI Z136 for the United States and IEC 60825-1 internationally, based on the potential for causing immediate injury. Common lasers for welding and cutting are infrared indeed; therefore, since the beam light may be invisible to the human eye, precautions could be difficult to be taken; even more difficult could be convince people to take precautions against possible hazards they may not understand [17].

The main source of danger of a laser beam is the light radiation which could be easily reflected by the work-piece, especially when processing metals, and could quickly produce in mild skin burns as well as irreversible injury to skin and eyes. It is now widely accepted that the skin is far less vulnerable than the eye, the former being provided with an external protective layer of dead cells, whilst an ocular focusing effect applies when a mirror-like reflection enters the eye. Special shielding devices in the form of spectacles or goggles with proper filtering optics, to be labeled with both the optical density and the wavelengths they are suitable for, are then required to protect the eyes, according to international standards.

Opaque barriers are needed anyway for the purpose of safety around the processing area; although designed to offer a wide range of protection, barriers do not normally withstand high welding energy radiations for more than few seconds, without some damage including the production of smoke and open fire. Additional non beam hazards, which are associated with the use of lasers although not being directly dependent on the beam itself, can be life threatening. Since high energy levels are delivered, possible hazard of fire must be addressed; hence, any flammable material is required to be kept away from the processing area; also, any reflected beam could start fire in unexpected places.

Adequate ventilation is needed as fumes are produced during the process. Eventually, given that a relative motion is in place between the laser beam and the work-piece, moving bits are additional source of risk.

## 1.6 WELDING ROBOTS

Three-dimensional welding of car and aircraft components is often required. Since most welding processes are not capable of being well enough controlled for three-dimensional manipulation and monitoring, robot-assisted laser welding heads are usually employed to move the beam along the welding path [5, 18]. On the other hand, for the sake of competitiveness, manual welding in modern industries must be limited to few operations, due to many further reasons such as long set-up time, operator discomfort, safety issues and resulting costs. Additionally, the optimized welding condition must be maintained during the process and must be reproducible over a series of welds to be performed [2].

Therefore, industrial robots are essential components and specific tasks as assembly operations and materials handling are addressed in repetitive manner at acceptable cost and quality levels: in particular, it has been estimated that as much as 25% of all industrial robots are specifically employed to weld and the most active industry in their application is the automotive [10]. For safety reasons, welding robots become a need with laser sources which are recognized as being potentially dangerous.

Robotic welding has undergone severe evolution. A first generation of welding robots had been developed in the early sixties as two-pass system, since a first pass is needed in order to learn the seam geometry and the welding path, whilst the second pass is the actual welding one: the working space is properly structured such that the robots can easily move along predetermined paths. On the other hand, a second generation of welding systems had been introduced in the seventies to track the seam in real time, with simultaneous learning and welding, thanks to a combination of both mechanic and electronic devices to identify any possible obstacle within the working space. Further advantages had been achieved in the eighties with third generation welding robots which actively fix their movements and compensate any changes in position and orientation of the work-piece; they are capable of being used for point-to-point as well as continuous motion to be settled off-line, with additional high-level diagnostic capability to report about failures and maintenance [19]. In this case, great flexibility is accomplished, at the expenses of a considerable amount of programming work of high-skilled operators [10].

# 2

# LASER OPTICS AND QUALITY

## 2.1 INTRODUCTION

Laser sources of high reliability are required to weld metals on a commercial basis. In addition to typical benefits of laser beam welding above conventional technologies, several further advantages are achieved when using thin disk sources, because high output power, high efficiency and good beam quality are simultaneously delivered, unlike traditional laser systems [20]. Disk lasers had been pioneered in the nineties by Adolf Giesen at the University of Stuttgart and have been enhanced for serial production after being offered as commercial products from different companies [21]. One particularly successful implementation had been first developed by Volkswagen to weld the Passat rear shelf and has been given approval for serial production in December 2005: in a detailed examination of the economic viability of the process, the operating costs of the thin disk laser were significantly reduced in comparison with previous lamp-pumped systems [22].

## 2.2 PRINCIPLES OF LASER EMISSION

Laser is the acronym for light amplification by stimulated emission of radiation, since the beam is produced by an electromagnetic radiation emission in a specific solid, liquid or gaseous material which is called the gain medium, or the active laser medium, whose atoms are moved to higher energy levels as a consequence of absorbing stimulating energy.

Some external supply of energy in the form of bright light, electric current or chemical reaction is required to pump the gain medium. In particular, when light is injected to electronically excite the medium, optically pumped lasers are obtained [23]. In general, excited states are produced in the atoms, since the electrons which are in the nearest possible orbits to their nucleus move from the ground state to outer orbits. Excited states are generally not stable: therefore, when the electrons drop from a higher energy level to lower one, extra energy is emitted in the form of a photon and light is produced. The process occurs as spontaneous emission when the electron naturally decays into a lower level, without outside intervention; the photon is then emitted in a random spatial direction. Its frequency $\nu$ is shaped by the rules of quantum mechanics, being $E_1$ the energy of the lower level, $E_2$ the energy of the higher one and $h$ the Planck’s constant:

$$\nu = \frac{E_2 - E_1}{h} \tag{2.1}$$

The resulting wavelength $\lambda$ of the emitted photon is given by:

$$\lambda = \frac{c}{\nu} \tag{2.2}$$

where $c$ is the speed of light in vacuo. Stimulated emission takes place instead when the incoming input photons with suitable energy or optical frequency enhance the emission; in this case, any emitted photon has the same phase, wavelength and direction of the passing one [24, 25]. Therefore they are: coherent with respect to each other, with peaks and valleys moving together through time and space; monochromatic, consisting in one single color; and parallel with little spread. For such specific features, a laser beam differs from ordinary light.

As long as the lower energy states prevail over the higher states, stimulated emission is prevented, since emitted photons are absorbed to raise an electron from a lower energy configuration to a higher one, instead than stimulating a drop of energy. On the contrary, when the number of excited electrons exceeds the number of electrons in the ground state or in a less excited state, population inversion is achieved and higher energy configurations predominate, so spontaneously emitted photons are more likely to stimulate further emissions, thus generating a cascade of photons [24]. For this condition to be fulfilled, the gain medium must therefore be pumped over the lasing threshold; hence, the stimulated emission prevails against the spontaneous one, thus allowing an amplification of the incoming radiation [23].

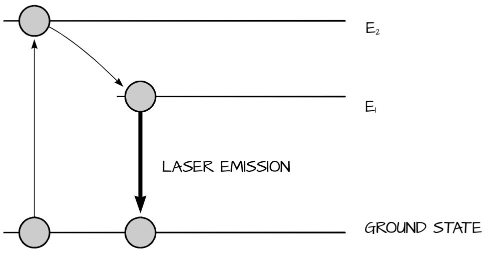

**FIGURE 2.1** – Three-level system for laser emission

The basic conceivable system has only two energy levels, which are not enough anyway for population inversion, because an eventual equilibrium is achieved between absorption and stimulated emission, with equal number of electrons on each energy state, resulting in optical transparency and actually no net optical gain. Three levels at least are then required to produce non equilibrium conditions: referring to **figure 2.1**, the gain medium is first excited to a short-lived high energy state which spontaneously and rapidly drops to a somewhat lower energy metastable state trapping and holding the excitation energy to be used for laser emission when further dropping to the ground state.

As light is emitted, electrons accumulate in the ground state, so the gain medium needs to be strongly pumped in order to keep population inversion. This difficulty is overcome with four levels, where an additional short-lived transition state is located before the ground one, as shown in **figure 2.2**. A rapid energy drop is in place between the lower laser level and the ground state, so population inversion between the higher laser level and the lower one

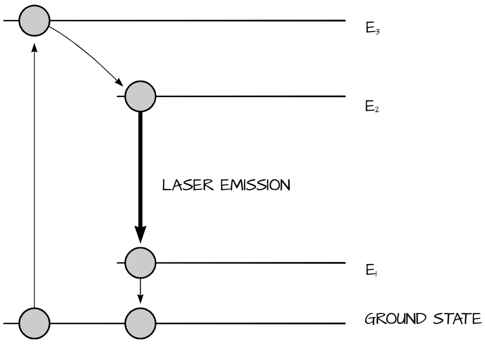

**FIGURE 2.2** – Four-level system for laser emission

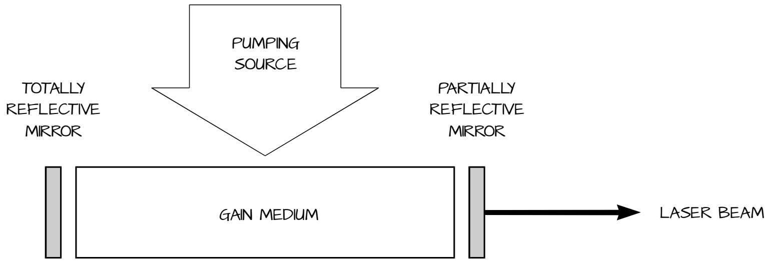

**FIGURE 2.3** – Resonant cavity scheme for laser emission

is heavier compared with three-level lasers. Furthermore, few atoms must be excited into the upper laser level to produce population inversion; therefore four-level lasers are much more efficient. A quasi-three-level gain medium provides an intermediate configuration, where high pumping densities are needed anyway because the lower laser level is close to the ground state which is formed by a certain number of thick sub levels. Notably, irrespective of the number of levels, the energy gap for pumping transition is greater than the energy gap of the laser transition, so when optically pumping the gain medium, the pumping light frequency has to be greater than the resulting laser one, both of them to be in agreement with equation (2.1), depending on the energy levels being considered. Consequently, the pumping wavelength is shorter than the laser one.

A resonant cavity which allows to build up light energy, increasing its intensity in order to generate a beam is required. Otherwise any gain medium would just be an optical amplifier to enhance light from an external source. As shown in **figure 2.3**, an optical resonator is composed by placing the gain medium between a pair of mirrors which face each other such that the emitted light is reflected back and forth, thus improving the uniformity of the emitted photons. One of the mirrors is generally only partially reflective, so to transmit a fraction of the incident light [24] to form a narrow beam which is suitable for several applications.

Basically, two emission modes make the relevant distinction between laser systems: continuous wave and single pulsed. When working in continuous wave emission, a stable adjustable average beam power is delivered; on the other hand, in case of pulsed operation the output takes the form of pulses of light on the time scale. Versatile lasers can be operated in both modes since a source whose output is normally continuous can be intentionally turned on and off at some rate in order to create pulses of light; nevertheless, specific lasers outputs are only pulsed because the gain medium cannot be run in continuous mode [23]. Customized pulse shapes are often useful in optimizing welding, particularly when spot welding aluminum alloys [2].

## 2.3 BEAM DELIVERY SYSTEMS

Two possibilities are allowed to eventually deliver the laser beam from the resonant cavity to the processing location: free space propagation through oscillating mirrors and lenses, or flexible optical fibre cables [9, 18, 26]; additional integrated beam switches are capable of managing up to six different outputs in the same delivery device [22].

When using high quality optics for free space propagation, laser quality is not significantly affected although any required device is complex, expensive, often bulky and difficult to maintain. Ideal delivering is therefore offered by fibre cables when considering complex processing paths or complicated manipulation of the optics; up to several hundred metres long cables are available, being them particularly suitable for assisting robots [27].

Whichever the chosen solution, the concept of laser sources and their beam delivery system as separate entities is abandoned in state-of-the-art equipments, in favour of an integrated approach which combines all of the elements for laser generation and beam delivery into a single system whose performances are optimized for the specific joining application [2].

## 2.4 RESONATOR MODES

The intersection between a generic plane and the laser beam produces the beam spot, which is a circle when the plane is orthogonal to the beam propagation axis and the beam shows circular symmetry for any possible cross-section. The architecture of the resonant cavity affects the light intensity distribution within the spot, because the energy is built up in specific locations at the expense of others; that is to say, it is possible to achieve a maximum value at the centre of the spot, or else to evenly allocate the energy.

The power of electromagnetic radiation per unit area is the radiative incident flux on a surface and is referred to as irradiance.

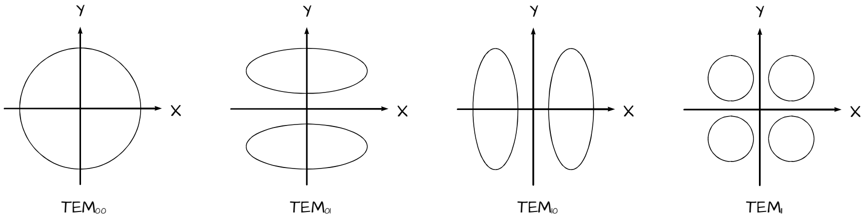

**FIGURE 2.4 –** Transverse electromagnetic modes, as resulting from Hermite-Gaussian solutions

Its profile in the beam cross-section is described through the resonator mode or transverse electromagnetic mode (TEM) which is normally denoted as TEM$_{mn}$ where subscripts $m$ and $n$ stand for the number of minimum values in the irradiance distribution along generic orthogonal $x$ and $y$ directions, respectively [9]. With this rule, possible profiles of irradiance resulting from the Hermite-Gaussian solutions to the equation of electromagnetic propagation [28] are shown in **figure 2.4**. The fundamental TEM$_{00}$ mode apply for any laser source featuring a beam with no minimum; its only irradiance peak locates on the beam propagation axis at the centre of the cross-section and a Gaussian transverse profile of irradiance is thus produced along any possible direction, thus regardless of the angular coordinate, as shown in **figure 2.5**. A laser operating on a single type of resonator mode, which is almost always a Gaussian one, is referred to as single-mode [23]. As a function of the $r$ position from the cross-section centre, the irradiance distribution in a polar coordinate system has the form:

$$I(r) = I_0 \cdot e^{-2\left(\frac{r}{R}\right)^2} \tag{2.3}$$

where $I_0$ the peak irradiance and $R$ the beam radius, which needs to be defined

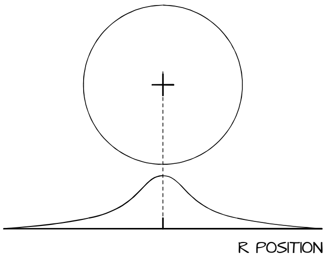

**FIGURE 2.5 –** Beam irradiance distribution as a function of distance from beam centre

in some way because the irradiance continuously decays to zero at a distance from the beam centre [28]. The common form (2.3) actually comes as a consequence of conventionally accepting the beam radius as being the finite distance where irradiance drops of $e^2$ with respect to its peak [29], based on the second moment of the intensity distribution [23]. Thus:

$$I(R) = \frac{1}{e^2} \cdot I_0 = 0.135 \cdot I_0 \tag{2.4}$$

Namely, the beam irradiance at the beam radius $R$ falls to 13.5% of its peak; therefore, as much as 86.5% of the total irradiance is held within a circle of radius $R$. The beam diameter is eventually defined as twice the beam radius.

## 2.5 LASER BEAM GEOMETRY

In order to compare different laser sources, a general understanding of the nature of the laser output is needed. As shown in **figure 2.6**, any laser beam draws a rotational hyperboloid of one sheet [9]: moving along the propagation axis, it shows convergent geometry towards the beam waist, which is intended to be the location where the minimum diameter $D_0$ or the beam focus diameter is achieved and the optical wave-fronts are flat [23]; then, the beam diverges again with symmetrical trend with respect to its focus.

A reasonable approximation of the asymptotic variation of the beam radius expanding from the waist towards the far field is provided by a conical shape whose aperture angle $\theta$ is considered to be the beam divergence angle or the angular spread. The beam expanding from its waist gives rise to a caustic curve whose analytical expression [9] has the form:

$$D^2(z) = D_0^2 + z^2 \cdot \theta^2 \tag{2.5}$$

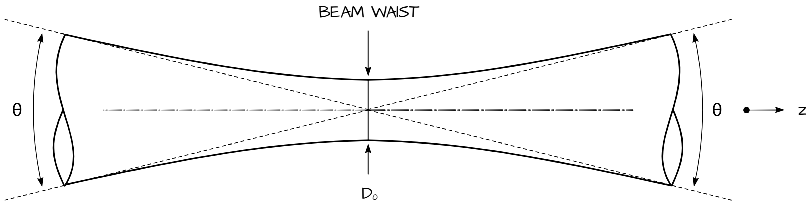

**FIGURE 2.6 –** Symmetrical trend of beam propagation with respect to its waist

which gives the beam diameter $D$ at a certain location $z$ from the focus point, on the propagation axis, depending on divergence angles in the order of tenths of radians. Nevertheless, considering the approximation in the far field, the beam diameter at proper distance from the focus point can be obtained from:

$$\frac{D_\infty}{2 \cdot z_\infty} = \tan\frac{\theta}{2} \tag{2.6}$$

Hence, for small divergence angles, this yields:

$$D_\infty = z_\infty \cdot \theta \tag{2.7}$$

If a lens focuses a laser beam, a new waist with different focus diameter as well as a new far field divergence angle are formed. This happens in a way that constancy is in place for their product, provided that ideal aberration free optics are used [5, 9]. Stronger focusing then leads to higher divergence angles [23]. In particular:

$$D_0 \cdot \theta = \frac{k \cdot \lambda}{N} \tag{2.8}$$

where $N$ is the refractive index of the material which light is travelling through; it is normally neglected for propagation through air [9], being it 1.0003. Therefore:

$$D_0 \cdot \theta = k \cdot \lambda \tag{2.9}$$

On the other hand, light wavelength $\lambda$ depends on the active gain for laser emission, whilst $k$ is a constant to take account of the irradiance distribution whose mode then affects the beam geometry. Light wavelength depends on the energetic levels of the specific gain medium; corresponding values for a number of lasers are listed in **table 2.1**. As for $k$, a Gaussian beam yields:

$$k_G = \frac{4}{\pi} \tag{2.10}$$

and lower values are not possible due to diffraction effects. As a consequence, the resulting divergence angle $\theta_G$ is:

$$\theta_G = \frac{4 \cdot \lambda}{\pi \cdot D_0} \tag{2.11}$$

**TABLE 2.1** – Operation wavelengths and pumping sources for a number of lasers

| Gain medium | Laser type | Pumping source | Operation wavelength [µm] |
|---|---|---|---:|
| Excimer | Gas | Electrical discharge | 0.193 ÷ 0.353 |
| Nitrogen | Gas | Electrical discharge | 0.337 |
| Gallium nitride | Semiconductor | Electrical discharge | 0.400 |
| Ruby | Solid state | Flashlamp | 0.694 |
| Ytterbium glass | Solid state | Laser diodes | 1.000 |
| Ytterbium YAG | Solid state | Laser diodes | 1.030 |
| Neodymium glass | Solid state | Laser diodes | 1.062 |
| Neodymium YAG | Solid state | Laser diodes | 1.064 |
| Oxygen iodine | Chemical | Chemical reaction | 1.315 |
| Thulium YAG | Solid state | Laser diodes | 2.000 |
| Holmium YAG | Solid state | Laser diodes | 2.100 |
| Erbium YAG | Solid state | Laser diodes | 2.940 |
| Carbon dioxide | Gas | Electrical discharge | 10.60 |

which is the lowest value a laser beam may ever achieve for a given waist diameter. Since a limit is thus imposed on the beam divergence, Gaussian laser beams are said to be diffraction-limited and are therefore deemed to be ideal.

### 2.5.1 RAYLEIGH RANGE

From the caustic equation (2.5), as well as from its asymptotic approximation in the far field (2.7), it is clear that low divergence angles allow to better restrain the diameter expansion along the propagation axis. Beams with very small angle spreads, such that their diameter is approximately constant over significant propagation distances, are called collimated beams. Nevertheless, in order to effectively weigh up the diameter constancy, a quantitative measure must be referred to. The Rayleigh range is usually considered, being it the distance from the beam waist, in the propagation direction, where the beam diameter expands although remaining below a threshold value $D_h$ which is given by:

$$D_h = h \cdot D_0 \tag{2.12}$$

where $h$ is positive arbitrary [9]. The corresponding Rayleigh range $z_h$ is therefore obtained from the caustic equation (2.5):

$$z_h = \frac{D_0}{\theta}\sqrt{(h^2 - 1)} \tag{2.13}$$

Given the symmetry of a laser beam, the total distance for the beam to be considered as collimated is the double Rayleigh range, which is measured across the focal point and is referred to as the depth of focus or, according to older literature, the confocal parameter [23]. Equation (2.13) suggests that, irrespective of $h$, high divergence angles are detrimental for the purpose of collimation; moreover, it is not possible to benefit from both small focus diameter and large depth of focus at the same time. The most common value for $h$ to determine the Rayleigh range is the square root of 2 because the doubling of the focus spot is thus produced. Then, equation (2.13) yields:

$$z_{\sqrt{2}} = \frac{D_0}{\theta} \tag{2.14}$$

and the caustic equation (2.5) alternatively becomes:

$$D^2(z) = D_0^2\left(1 + z^2 \cdot \frac{\theta^2}{D_0^2}\right) \Rightarrow D(z) = D_0 \cdot \sqrt{1 + \left(\frac{z}{z_{\sqrt{2}}}\right)^2} \tag{2.15}$$

A much more restrictive value of 1.05 is used sometimes for $h$ to calculate the distance over which the beam diameter spreads of 5% with respect to the focus. From a technological point of view, high depth of focus are desirable and often crucial for certain welding conditions because the threshold irradiance must be overcome through the entire thickness of the work-piece aiming to perform a deep penetrative welding; therefore, a depth of focus which is too short with respect to the thickness, may not be adequate to effectively perform the process [9].

As one may expect, the Rayleigh range is affected by the beam irradiance distribution also, since a dependence on the TEM profile is embedded in the Rayleigh range as a consequence of product constancy between $D_0$ and $\theta$, as shown in equation (2.9). Therefore equation (2.14) yields:

$$z_{\sqrt{2}} = \frac{D_0^2}{k \cdot \lambda} \tag{2.16}$$

The largest possible Rayleigh range is then achieved when considering a Gaussian beam, having it the lowest $k$ value:

$$z_{\sqrt{2}_G} = \frac{D_0^2}{k_G \cdot \lambda} = \frac{\pi \cdot D_0^2}{4 \cdot \lambda} \tag{2.17}$$

In this sense, the benefit of an ideal Gaussian beam is once again pointed out in terms of its depth of focus.

### 2.5.2 BEAM DEPENDENCE ON THE FOCUSING OPTICS

When a laser beam is delivered via optical fibre, as shown in **figure 2.7**, it expands as soon as it exits the cable, since it is no longer constrained by the internal light reflections within the fibre; therefore, it needs to be focused again. This is performed using a pair of lenses which are, in the order the beam meets them, a collimating one to align the beam and a focusing one to achieve smaller diameters [9]. With the assumption of aberration free optics, the product between the waist diameter and the far field divergence angle is the same when measured either at the collimating side or the focusing side. Being $D_F$ the fibre core diameter, which is actually the waist diameter at the collimating side, and $\theta_C$ the corresponding divergence angle, the constancy condition is written as:

$$D_F \cdot \theta_C = D_0 \cdot \theta \tag{2.18}$$

In the case of light sources at infinite distance or reduced beam divergence, the distance between the lens and its corresponding focus point is roughly equal to the focal length. As the beam diameter $D_L$ between the lenses is achieved in the collimating far field at a distance $f_C$ from the focal point, as well as in the focusing far field at a distance $f_F$ from the focal point, equation (2.7) yields:

$$D_L = f_C \cdot \theta_C \tag{2.19}$$

$$D_L = f_F \cdot \theta \tag{2.20}$$

Hence, the far field divergence angles are in inverse proportion to the corresponding focal lengths:

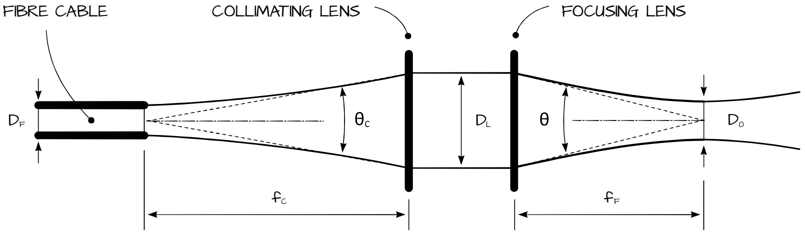

**FIGURE 2.7** – Beam delivering via fibre cable and corresponding focusing scheme

$$\frac{f_C \cdot \theta_C}{f_F \cdot \theta} = 1 \Rightarrow \frac{f_C}{f_F} = \frac{\theta}{\theta_C} \tag{2.21}$$

When combining this result with equation (2.18), the resulting downstream focus diameter $D_0$ is found to be dependent on both the focal lengths:

$$D_0 = \frac{f_F}{f_C} \cdot D_F \tag{2.22}$$

so the beam is delivered with the fibre core diameter if lenses with the same focal length are employed. Interesting additional conclusions are drawn when considering the impact of the focusing lenses on the Rayleigh range, which is then given by equation (2.14):

$$z_{\sqrt{2}} = \frac{D_0}{\theta} = D_0 \cdot \frac{f_F}{D_L} \tag{2.23}$$

This suggests that the proper focal length in the focusing optics must be chosen with respect to the process to be performed: as a consequence of equation (2.22), smaller focus diameters, and thus higher beam irradiances, are implied by a shorter $f_F$ which, on the other hand, imposes a shorter depth of focus and a higher angle spread.

## 2.6 BEAM QUALITY

Different ways are commonly used to refer to laser beam quality, which essentially is a measure of how tightly a laser beam can be focused with limited beam divergence. Indeed, narrow spots are crucial to prevent irradiance reduction for all of the applications such as printing, marking, welding, cutting and drilling where strong focusing of the beam is required [23], with the exception of variable gapped seams which are difficult to be tracked so that a wider beam would be easier and more reliable to be used [5]. On the other hand, surface treatments are less critical since larger spots are required; poor beam qualities are then satisfactory anyway.

The index which is normally used to refer to beam quality is the beam parameter product ($BPP$), being it the product of the beam radius $R_0$ at the beam waist with the far field beam divergence half-angle $\alpha$:

$$BPP = R_0 \cdot \alpha = \frac{D_0}{2} \cdot \frac{\theta}{2} = \frac{D_0 \cdot \theta}{4} \tag{2.24}$$

which makes sense because it has been proven that constancy is in place for any given beam for the product between the focus diameter and the divergence angle, although non ideal optics can spoil the beam quality and thus increase the $BPP$. Hence, considering equation (2.9):

$$BPP = \frac{k \cdot \lambda}{4} \tag{2.25}$$

Usual units for $BPP$ are millimetres times milliradians; non circular beams provide different values for $BPP$ depending on the considered direction to measure the spot contour. For the purpose of beam quality, the higher is the $BPP$, the lower is the beam quality. Alternatively, focusability $\varphi$ is intended to be the ability to achieve a small focus diameter with a given optical element; it is defined as the inverse $BPP$ [30]:

$$\varphi = \frac{1}{BPP} = \frac{4}{D_0 \theta} \tag{2.26}$$

Ideally, considering the divergence angle of a Gaussian beam in equation (2.11), the smallest possible value for BPP is given by:

$$BPP_G = \frac{D_0 \cdot \theta_G}{4} = \frac{D_0}{4} \cdot \frac{4 \cdot \lambda}{\pi \cdot D_0} = \frac{\lambda}{\pi} \tag{2.27}$$

Since the output from real lasers is unfortunately not truly Gaussian, although very close, an additional beam quality index, the so called $M^2$ factor or beam propagation parameter, is introduced to accommodate this variance [28, 29]. It is defined as the laser $BPP$ divided by the corresponding ideal $BPP$ of an equivalent Gaussian beam with the same wavelength; it is therefore a dimensionless quantity. Considering equation (2.27):

$$M^2 = \frac{BPP}{BPP_G} = \frac{BPP}{\frac{\lambda}{\pi}} = \frac{\pi \cdot BPP}{\lambda} = \frac{\pi \cdot k}{4} \tag{2.28}$$

In this sense, $M^2$ takes account of the deviation of a laser beam from a theoretical Gaussian one which yields:

$$M^2 = 1 \tag{2.29}$$

Lower values are not possible: for high energy lasers, the $M^2$ factor can be as high as 1000 [23]. A relation is drawn between $M^2$ and the divergence angle when combining equations (2.4) and (2.8):

$$\theta = \frac{4 \cdot \lambda \cdot M^2}{\pi \cdot D_0} \tag{2.30}$$

The laser spread then depends on the irradiance distribution: the higher is the $M^2$ factor, the lower is the beam quality, since higher divergence angles are obtained, other parameters being taken as constant. This has obvious impact on the Rayleigh range as well, which is decreased by the $M^2$ factor with respect to the corresponding value of a Gaussian one [23] for those beams with imperfect beam quality. Indeed, when considering its form in the equation (2.14), the Rayleigh range becomes:

$$z_{\sqrt{2}} = \frac{D_0}{\theta} = \frac{D_0}{\dfrac{4 \cdot \lambda \cdot M^2}{\pi \cdot D_0}} = \frac{\pi \cdot D_0^2}{4 \cdot \lambda} \cdot \frac{1}{M^2} = \frac{z_{\sqrt{2}_G}}{M^2} \tag{2.31}$$

Although smaller fibres for beam delivery produce less degradation of beam quality, it has been pointed out that the minimum fibre core diameter to be used is in direct ratio with the beam propagation parameter, any other factor taken as constant [27].

For certain industrial applications, the generation of high power is not enough, as high brightness is required [31]. With respect to laser technology, brightness $B$ is a measure of the maintenance of intensity while a beam propagates from its focus; it is intended in a quantitative sense and is generally understood as being equivalent to its radiance, which is the total power $P$ divided by the product of the focus area $A_0$ and the solid angle $\Omega$ in the far field [23]:

$$B = \frac{P}{A_0 \cdot \Omega} \tag{2.32}$$

Brightness is usually expressed in watts per square millimetres per steradians. It can be related to $M^2$ since:

$$B = \frac{P}{(\pi \cdot R_0^2) \cdot (\pi \cdot \alpha^2)} = \frac{P}{\pi^2 \cdot BPP^2} = \frac{P}{\lambda^2 \cdot M^4} \tag{2.33}$$

and is therefore considered to be a better indicator compared with raw power, because high brightness means high power at good beam quality. Hence, high quality is crucial when power is limited and high irradiances are required anyway [27]. Although the output power is lower than the pumping one, laser beams resulting from gain medium pumping show much higher brightness compared with the pumping source; in this sense, lasers are usually referred to as brightness converters [23].

## 2.7 LASER EFFICIENCY

Performances of optically pumped lasers are judged in terms of efficiency, and their power is compared [32]. When considering the total expense of a laser system in terms of electricity bill, the wall-plug efficiency has to be referred to, being it the total electrical-to-optical power efficiency. Taking the term seriously, the electrical power should be measured at the wall-plug, so that the efficiency includes both losses in the power supply and any power term for cooling, which can be significant for high power lasers. Hence, the demands on electrical installations and in turn the size of the overall system are reduced when higher wall-plug efficiencies are in place. However, it is common practice to account the wall-plug efficiency as based on the electric power to the laser diodes, thus neglecting the actual wall-plug [23].

Purely considering the optical features, the slope efficiency or the differential efficiency is alternatively defined as the slope of the curve of laser output versus pumping power; usually, once crossed the threshold pumping power, the curve is close to linear, so that slope efficiency as a single number effectively makes sense. The output power trend as a function of the pumping power is shown in **figure 2.8**. The threshold pumping power is 5 kW and the slope efficiency is 50%: this leads to 0.5 W additional output for each additional watt of pumping power above the threshold.

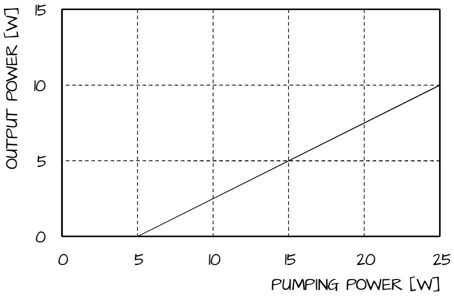

**FIGURE 2.8 –** Output power trend as a function of the pumping one

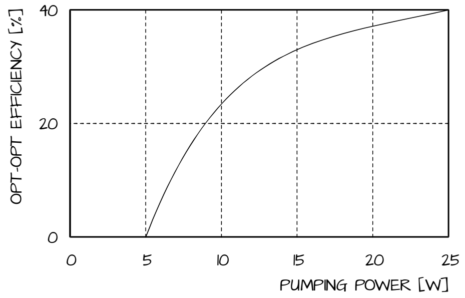

**FIGURE 2.9 –** Optical-to-optical laser efficiency as a function of the pumping power

However, non linear curves can result under certain circumstances, for example when considering a quasi-three-level gain medium; furthermore, a laser may even stop working for too high pumping powers, when the stability zone of the laser resonant cavity is left, due to excessive thermal lensing effect. In case of such non linear curves, the slope efficiency is often determined via approximation. The optimization of the laser output power for a given pumping power usually involves a trade-off between high slope efficiency and low threshold pumping power.

The raw ratio of the output power to the pumping power is the optical-to-optical laser efficiency; the resulting shape of the curve is given in **figure 2.9** and depends on the slope efficiency as well as on the threshold pumping power.

## 2.8 THIN DISK LASER CONCEPT

The thin disk laser is a diode-pumped solid state laser, since its base concept rely on a solid state gain medium which is pumped via diodes [20, 31]. As for any other high power solid state laser, the challenge in designing a successful device is how best to deal with the inevitable generation of waste heat as a consequence of the pumping process. Inadequate thermal management results in imposing a limit on the laser output power and deterioration of beam quality [31]. Indeed, non uniform deposition of heat is typical of diode-pumped solid state lasers, so temperature gradients are set up through the gain medium which is hotter on the beam axis, compared with the outer regions [32], typically causing some transverse variation in the refractive index which is temperature dependent [23]. A thermal lensing effect is then induced because the gain medium acts as a real lens, thus increasing the beam divergence. Additionally, thermal gradients are also reason for differential thermal expansion within the gain medium: bulging faces are produced in cylindrical rod or slab laser, with consequent enhanced lensing effect and thermal stresses which eventually lead to thermally induced fractures in the gain medium [31].

### 2.8.1 ARCHITECTURE

In order to mitigate the detrimental consequences of heating up the gain medium, intensive research over a number of years has been conducted both on geometry and materials. It has been pointed out that the distance the heat must flow through the gain medium must be reduced, as far as possible; moreover, a geometry which would minimize the effect of any optical change in the laser field must be chosen.

The thin disk laser design arises as natural consequence: the core concept of the principle is a thin and disk-shaped gain medium. A short axial dimension is achieved in comparison with the radial extent: the disk is 100 to 200 μm thick, depending on the specific material of the gain medium [20]; the diameter ranges from 10 to 20 mm instead, depending on the power level [22]. The pumping beam, whose spot diameter is significantly larger than the thickness of the disk [31], is incident on a large gold-coated parabolic mirror which provides longitudinal excitation of the disk and allows beam propagation downstream via its on axis hole.

A side view for the architecture of a thin disk laser system is shown in **figure 2.10**. The disk is fasten to a heat sink which provides cooling by water impingement thanks to several nozzles inside [33].

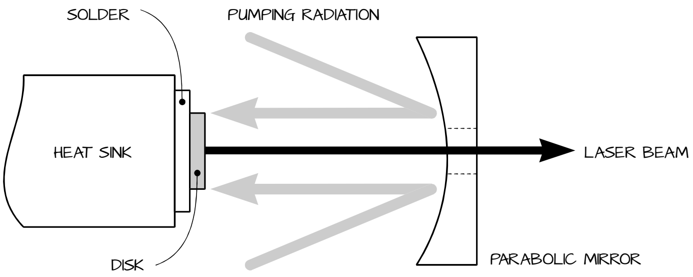

**FIGURE 2.10 –** Thin disk laser design: side view for architecture and pumping

Hence, cooling of the disk occurs through the back-side flat face which is also used as the ending mirror in the resonant cavity and is properly coated to be highly reflective at both the pumping and laser wavelengths, whilst the other face is provided with an anti reflective coating to both wavelengths [31], so that the disk behaves as an active mirror itself [23].

The advantage which naturally comes when cooling through a large face of a thin slice of material is that the ratio of the cooled volume to the cooling surface area results to be small, as indeed is the distance the heat must flow to reach the heat sink. In such this shape, the gain medium is aggressively cooled: since the direction of the heat flow is parallel to the short axis of the disk, the heat load is uniform in the transverse direction where, as a consequence, the excursions of temperature are minimized; this results in purely axial gradients which in turn imply the intra cavity field experiencing no thermal lensing [31]. Compared with a rod laser geometry, where cooling is essentially managed in the radial direction [32], variations in the refractive index profile are reduced by more than one order of magnitude [20], with minimal distortions of the wave-front [21].

Issues of thermal expansion within the gain medium are not removed at all because cooled and non cooled surfaces still experience different thermal fields, as a consequence of axial temperature gradients. This leads to bowing the disk and hence to a curved resonator mirror which is the dominant effect of the thermal distortion affecting the laser emission in the effective absence of classical thermal lensing effect [31]. It is clear that fastening of the disk to the heat sink is the key engineering step in the manufacture of the resonant cavity; it is equally clear that extensive discussions about the topic are not available in open literature. Nevertheless it has been suggested that indium-tin or gold-tin solders are being used in the highest power systems to join the disk to the heat sink: a very stiff fixation without deformation of the disk is obtained. Furthermore, in order to reduce any possible stress during and after the soldering process, the heat sink is made of a heat expansion matched Cu-W based alloy [33]. Additionally, in order to facilitate the joining, few dielectric layers are usually employed for back-side disk coating [31].

### 2.8.2 GAIN MEDIUM

Several materials were considered in research to manufacture the disk laser gain medium. Convincing results were achieved exploiting ytterbium (Yb), which is a bright, soft, silvery-white metal in the group of rare earth elements. Solid state gain medium with interesting optical properties are obtained when ytterbium is used as doping agent in a synthetic crystalline material such as yttrium aluminum garnet (YAG), thus resulting in Yb:YAG laser sources [31, 33] with 1.03 µm emitted wavelength (cf. **table 2.1**), which is therefore outside the visible spectrum for the human eye. A pumping wavelength of 0.94 µm is generally used [23]. Typical doping concentrations in rare earth doped crystal are specified in atomic molar percentage (at.%) of the doping element [23]; an optimal 9 at.% concentration was suggested for Yb:YAG disk-lasers [20, 31].

A primary advantage is achieved with ytterbium doping since heat loading in the gain medium is almost three times lower compared with neodymium (Nd) doping [31]; moreover, benefits result from no parasitic effects such as up-conversion fluorescence, which takes place when the emitted wavelength is shorter than the exciting one; and cross relaxation, which is due to part of the energy of an excited electron being transferred to another one in the ground state, so that both electrons end up into an intermediate level [23].

However Yb:YAG gain medium is a quasi-three-level system; therefore high power densities are needed for the pumping process to reach the lasing threshold [34]. Moreover, depending on the thickness and the doping level of the disk, only a small fraction of the pumping radiation is absorbed [34]. The specific architecture of the resonant cavity allows to overcome the issues and a scheme of multiple pumping beam passes through the disk is used. Indeed, thanks to steering optics, unabsorbed pumping radiation is collimated again on the opposite side of the parabolic mirror, then focused onto the disk, from another direction. Theoretically, the process can be repeated until all of the virtual positions of the parabolic mirror have been used, so that 16 to 32 passes of the pumping radiation through the disk are realized and more than 90% of the diode power is absorbed.

The limit for the possible number of pumping passes is given by the diodes beam quality which determines the beam diameter on the parabolic mirror and hence the number of positions on the mirror which can be effectively used for redirection. The better is the beam quality of the pumping diodes, the higher is the number of possible pumping passes and the higher the total optical-to-optical efficiency of the thin disk laser [20]; as a consequence, the thickness of the disk can be further reduced as well as the ytterbium doping concentration [20, 31].

### 2.8.3 ADVANTAGES

Each component of the optical beam path from the laser source to the focusing optics contribute to the overall reliability of the application in its specific industrial environment. In this sense, thin disk lasers provide higher level of reliability and are then integrated in many production lines [22]. Indeed, diode pumping is considered to be a prime key advantage over lamp-pumped lasers, as longer lifetime of the pumping devices is benefited [23].

Moreover, as a consequence of multiple pumping beam passes through the disk and the specific architecture of the resonant cavity, so that light leaks around the mirrors are not amplified, any loss within the optical resonator is reduced [24]. Therefore, lower electrical power supplies are needed: this results in high wall-plug efficiency, in the order of 25% for industrial lasers with 8 kW output power; more than 5.3 kW have been achieved with a maximum optical-to-optical efficiency of 65% [33].

With respect to a mere technical point of view, the raw output power must be considered and adequately improved. Power scaling in laser design involves any procedure to achieve substantially increase in the optical output [23]. As no classic thermal lensing effect is experienced in the disk, the primary thermal limitation to power scaling is removed [31]: since the first demonstration of the principle, the output power of one single disk could be increased to more than 5 kW in continuous wave operation indeed. By arranging a series of four disks in the same resonator, an output power extraction of more than 9 kW is benefited [20, 22].

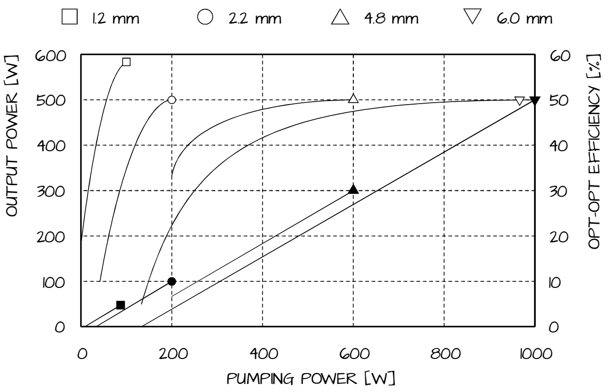

**FIGURE 2.11** – Laser output power and optical efficiencies as function of pumping spot diameters

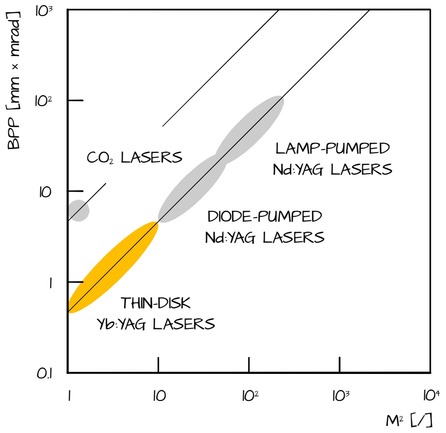

**FIGURE 2.12 –** Beam parameter product versus $M^2$ values for a number of lasers

However, in general, simple power scalability in single disk lasers sources is achieved just by increasing the pumping beam diameter, with no need for increase in diode brightness; laser power results for 16 pumping beam passes of different spot diameters between 1.2 and 6 mm onto a 9 at.% doped Yb:YAG disk are shown in **figure 2.11**. The slope efficiency and the optical-to-optical efficiency curves are similar among the examined conditions; nevertheless, being the lasing threshold proportional to the pumped area on the disk, it increases with increased pumping spot diameter [20].

In terms of beam quality, for a better comparison of laser sources, beam parameter product versus $M^2$ values for a number of laser types are shown in **figure 2.12**, so to simultaneously consider both the operation wavelength and the irradiance distribution. Due to longer wavelength, it is clear from equation (2.25) that $CO_2$ lasers have a larger $BPP$ than both ytterbium or neodymium solid state lasers, but still compare favourably with lamp-pumped systems [23]; anyway, thin disk Yb:YAG lasers noticeably offer the best $BPP$ to $M^2$ coupling. Larger Rayleigh ranges are then achieved: this allows to get a reproducible weld which does not depend on perfect control of the focus position [26]. Since working distances increase when compared with classical laser systems with insufficient focusability, thin disk lasers devices enable highly productive techniques such as remote welding where rapid beam deflections are used to reduce any non productive idle time during laser movements from one welding spot to the next one [20]; increased production speed is then achieved and the total processing time is estimated to decrease by a factor of three [22].

**TABLE 2.2 –** Technical data and resulting quality features for comparison of laser devices

| **Trumpf Haas HL-2006 D**<br>**BEO D25 focusing optics** | | **Trumpf Tru-Disk 2002**<br>**BEO D70 focusing optics** |
|---|---|---|
| Nd:YAG | Gain medium | Yb:YAG |
| Lamp-pumping | Exciting source | Diode-pumping |
| 1.064 | Operation wavelength [µm] | 1.030 |
| 2.0 | Maximum output power [kW] | 2.0 |
| 30 | BPP [mm × mrad] | 8 |
| 90 | Beam propagation parameter $M^2$ | 24 |
| 2.2 | Brightness [$10^5$ W mm$^{-2}$ sr$^{-1}$] | 33 |
| 600 | Delivery fibre diameter [µm] | 300 |
| 200 | Focal length of the collimating lens [mm] | 200 |
| 100 | Focal length of the focusing lens [mm] | 200 |
| 300 | Focus diameter [µm] | 300 |
| 0.75 | Rayleigh range [mm] | 2.8 |

Furthermore, larger working distances also allow to protect the optics against debris and fumes [23]. It has also been suggested that a higher beam quality allows to use small compact optics which are helpful in processing any part in locations which are difficult to access as well as in assembly lines. To eventually quantitatively translate these conclusions, technical data with resulting quality features for two laser welding devices are listed in **table 2.2**. Beams are both delivered via optical fibre; different gain medium and focusing optics are used, the Trumpf Tru-Disk 2002 with BEO D70 optics having an edge on the other in terms of beam quality.

### 2.8.4 DISK LASER VERSUS FIBRE LASER

Both cutting and welding application in laser material processing had been dominated by $CO_2$ sources, before thin disk and fibre lasers spread over [26, 35]. Marked advantages are benefited, although a number of aspects are involved in a detailed comparison of thin disk versus fibre, since specific features can be essential in some cases but insignificant in others [23].

In fibre lasers, a rare earth element is doped into the core of an optical fibre; as an example, a Yb:quartz gain medium results. The emission is thus produced within the fibre itself using a semiconductor diode as pumping source. Hence, although the basic architecture is different, both the thin disk laser and the fibre laser are diode-pumped solid state; moreover, both are delivered via optical fibre, both are compact with small footprint and both have excellent BPP and wall-plug efficiency in similar order of magnitude, although it has been reported [23] that a diffraction-limited Gaussian beam is closely approached by fibre lasers.

For industrial applications, both the systems are capable of being used in non monolithic shape, since the beam is delivered through plug-and-play process fibre. Nevertheless, only the disk laser is truly modular with open architecture, so upgradability is feasible with no splicing and there are no potential failure modes which require factory repair. Thousands of splices, such as single emitter diodes and beam combiners, are needed in fibre lasers instead and, although it has been suggested that an easier coupling to the beam delivering fibre is benefited [26], repairing is affected because some failure modes can only be repaired at the factory, thus leading to extended downtime; in addition, due to peculiar architecture, the system is sensitive to back reflection from metals with low absorptance. Eventually, the best choice is deemed to be application driven.

# 3

# PROCESSING DYNAMICS

## 3.1 INTRODUCTION

Laser welding is the result of a delicate balance between heating and cooling within a spatially localized volume. A number of parameters are involved. The leading variables are laser power and welding speed because they determine the rate of the energy input to the work-piece [2]. The power to speed ratio is usually referred to as the thermal input, with the assumption of laser input power being fully absorbed; reflection and transmission effects are usually neglected [8].

Basic relationships are in place among laser power, welding speed and penetration depth. In particular: any increase in laser power at constant welding speed yields a proportional increase in penetration depth; any increase in welding speed at constant laser power results in a corresponding decrease in penetration depth or even lack of fusion [10]; for a given penetration depth, the welding speed scales with laser power. These rules are analytically summed up [2] in simple regression in the form:

$$\frac{P}{s \cdot PD} = a + \frac{b}{s} \tag{3.1}$$

where $P$ is the laser power, $s$ the welding speed, $PD$ the penetration depth, $a$ and $b$ fitting parameters which depend both on the material and the laser source. Wider descriptions are needed in order to prevent inaccurate predictions; unfortunately, the correlation is usually found on a case-by-case basis and takes account of additional factors to be discussed in the following.

## 3.2 LASER WELDING MODES

Once the beam energy is absorbed in the material, an increase in temperature is obtained and a weld pool is produced. The evolution of the process depends on the irradiance being supplied and two fundamental modes of laser welding are possible: conduction welding and key-hole or deep penetrative welding.

The surface of the weld pool remains unbroken during conduction welding, whilst it opens up to allow the laser beam to deeply enter the material in key-hole welding mode [2]. Significantly different bead cross-sections are thus produced, as shown in **figure 3.1**. Conduction welding is commonly used both for metals and polymers; on the other hand, although being the most diffused mode in any welding technology where high heat input sources are employed, key-hole is specifically carried out on metals [9]. Referring to conduction welding, when low irradiance is delivered, the weld pool is similar to the corresponding one in conventional technologies such arc welding or oxy acetylene welding; given the relative movement between the beam and the work-piece, the weld pool seems to travel with the beam along the welding direction. The bead cross-section is nearly half circular, with resulting equal depth and width, as a consequence of the specific heat transfer mode which is in place during the process [2]. The convective patterns resulting in the weld pool are usually neglected, given the small amount of fused metal. High conductivity is normally preferred as general requirement in order to ease the heat transfer [9].

A higher irradiance produces a key-hole welding mode where vaporization occurs in addition to fusion. Therefore, a deep narrow hole is produced within the material [9], the fused walls sealing up behind it [5] as a consequence of high vapor pressures. The absorption of the laser beam significantly increases due to multiple reflections inside the hole, thus providing efficient welding even when considering highly reflective metals [10].

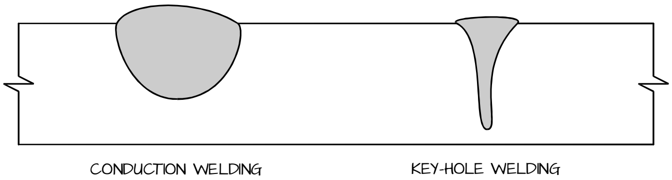

**FIGURE 3.1 –** Cross-section as produced in conduction welding and key-hole welding

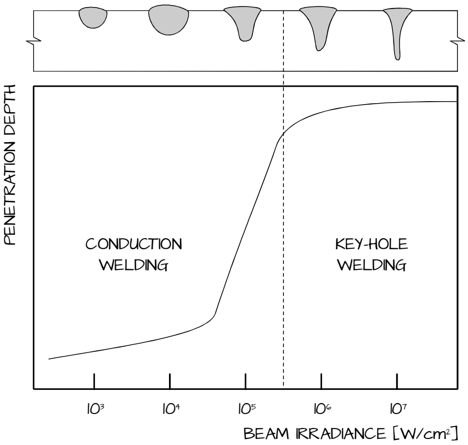

**FIGURE 3.2** – Penetration depth as a function of beam irradiance: conduction to key-hole transition

Heat is transmitted in depth through Fresnel absorption, which takes place within the fused material, and inverse bremsstrahlung absorption of plasma. In particular, on the top of the key-hole, the absorbed intensity is mainly decided by inverse bremsstrahlung, whilst Fresnel absorption rules at the key-hole tip [36, 37]. Bead quality is enhanced because vigorous mixing occurs in the molten metal as welding develops. Convective patterns in vortex structure start from the top of the weld surface heading towards the tip [5]: much more uniform chemical compositions are then achieved in the weld pool compared with conduction welding.

Once the beam has left the welding zone, quick solidification of the material occurs. The resulting bead shape-factor, which is commonly defined as the depth to width ratio, is significantly higher compared with the conduction mode; values of 10:1 are not uncommon [9]. Nevertheless, intermittent closure of the key-hole during the process may result in porosity as a consequence of gas entrapment [38]; in this sense, conduction welding offers less perturbation to the system [2].

Since vaporization occurs once a threshold temperature is overcome, a specific irradiance is required for the conduction to key-hole mode transition. In order to better describe the process, the evolution of the welding process when increasing irradiance is being supplied as a consequence of increasing laser output power, must be considered. In particular, the conduction welding mode is in place with low irradiance, the bead cross-section exhibiting low shape-factor; the bead size increases both in depth and width with increasing laser power, so no significant changes result in the shape-factor. Nevertheless, a sudden increase in depth is produced with no simultaneous increase in width once a threshold irradiance is overcome: the key-hole welding mode has then started, this leading to higher shape-factors. Threshold values do not depend on the welding speed which, in turns, scales the bead shape; on the other hand, although a dependence is expected on the material being welded, it has been found that a $10^6$ W/cm$^2$ irradiance has to be provided for steels to be key-hole welded [9] and the same value is usually considered for transition when welding aluminum and titanium alloys [38, 39] also. A qualitative trend for penetration depth as a function of irradiance is then shown in **figure 3.2**.

A change from one welding mode to the other can be produced by tailoring the laser irradiance, while the process is being carried out: the weld can be started in the conduction mode and then later converted to key-hole; computer control of laser power allows to manipulate the interaction in order to optimize the properties of the weld [2]. The transition comes with noticeable phenomena, since yellow and red light turns into a white and blue one when key-hole welding prevails over conduction [9].

### 3.3 KEY-HOLE INSTABILITY

A key-hole is basically an unstable structure which may result in spiking, that is the occurrence of unwanted fluctuations in penetration depth [40]: the highly non linear nature of the interaction between laser and material lead to rapid growth of the amplitude of the fluctuations [2].

Several models have been proposed in order to describe how these instabilities arise. As initial simplification, the motion of the key-hole through the work-piece is neglected and a stationary key-hole is then considered; furthermore, a blind hole is referred to [2], so a condition of incomplete penetration is modeled. As the welding process develops, the equilibrium is maintained through a pressure balance. Metal vapor acts with its vaporization or ablation pressure $p_v$ on the liquid phase; radiation pressure $p_i$ is produced by direct laser irradiation on the metal: they both tend to keep the key-hole open, whereas restoring additional pressures must be held back. Indeed, being $p_g$ the hydrostatic pressure which results as a consequence of fluid action on a generic surface, $p_h$ the hydrodynamic pressure which is provided by liquid motion around the key-hole, and $p_\sigma$ the surface tension to expand a liquid, the pressure balance is written in the form:

$$p_v + p_i = p_g + p_h + p_\sigma \tag{3.2}$$

all of the terms depending on penetration depth and hole radius. The contributes of radiation, hydrostatic and hydrodynamic pressures are small when considered in their functional form, being them two order of magnitude lower compared with both the vaporization pressure and the surface tension [41]. The balance then yields to:

$$p_v \approx p_\sigma \tag{3.3}$$

and determines the stability condition of the key-hole. Let $\sigma$ be the surface tension coefficient, $\rho_1$ and $\rho_2$ the principal key-hole radii of curvature; hence $p_\sigma$ is given by:

$$p_\sigma = \sigma \cdot \left(\frac{1}{\rho_1} + \frac{1}{\rho_2}\right) \tag{3.4}$$

Here $\rho_1$ is the equilibrium key-hole radius, whilst $\rho_2$ has to be measured on the hole surface which lays in the direction of laser propagation. The latter is larger, except when measured at the tip of the key-hole, where both radii are small and hence comparable; therefore the surface tension term actually reaches its highest at the tip of the key-hole, both radii being at their smallest, and then decreases with increasing $\rho_1$ along the key-hole axis towards the beam entrance [40].

The evaluation of a trend for vaporization pressure is not easy, due to the formation of a Knudsen layer, whose thickness is several mean free paths, where redeposition of material may occur thus effectively reducing the vaporization rate, as a function of temperature [2]. Nevertheless, self-consistent solutions have been numerically obtained [41]: it has been found that the vaporization pressure first increases with increasing key-hole radius which allows more of the incident power to enter the hole and enhance the ablation; then, due to the assumed Gaussian beam profile, the vaporization pressure decreases once a certain radius is achieved as a larger key-hole allows the laser beam to pass through the hole without effectively heating the walls, hence reducing vaporization [2]. Based on these conclusions, a deeper discussion on the pressure balance is now possible.

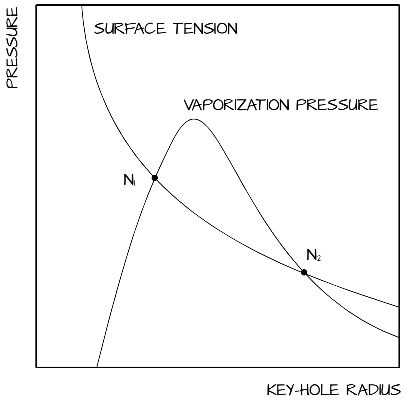

**FIGURE 3.3** – Key-hole pressure balance: surface tension and vaporization pressure trends

Referring to equation (3.3) and **figure 3.3** where surface tension and vaporization pressure trends are shown as a function of key-hole radius, two solutions are found.

Point $N_1$ represents a condition of unstable equilibrium: indeed, a decrease in the key-hole radius yields an increase in surface tension whilst vaporization pressure decreases, such that the overall tendency is in closing the hole, thus hindering the process; similarly, an increase in the key-hole radius yields an increase in vaporization pressure as well, while surface tension decreases and the hole continues to expand. Conversely, point $N_2$ represents a condition of stable equilibrium because any change in its nearness results in a restoring force. Therefore, any motion in the key-hole walls affects the interaction with the incident beam and the pressure variation. It has to be expected the key-hole radius to oscillate towards its stable solution. Actually, a range of characteristic mechanical vibration modes occur, depending on the gas flow within the hole, both key-hole diameter and depth, total liquid amount, material features, instability in laser intensity as well as boundary conditions both at the key-hole input and exit [2].

The range between the solution points depends on the power to depth ratio [41] and no solutions are possible below a threshold value, due to the threshold irradiance which is required for the key-hole to develop instead of a conduction welding mode. As the power to depth ratio decreases towards this minimum, the solutions become increasingly unstable as the $N_1$ to $N_2$ gap approaches zero: in this range, the penetration depth would fluctuate.

Although several assumptions are in place, many of the properties of the key-hole in laser welding at low speeds are successfully reproduced by this model and the dynamic effects of perturbations on the solution can be effectively estimated. It has to be considered that when referring to higher speeds which are quite common in laser welding processes, the hole rotational symmetry about the laser propagation axis is lost: in this case, the leading edge of the key-hole differs from the trailing one and curves back towards the weld [2]; a bent and elongated hole results, as theoretically determined by means of polynomial fitting [36].

## 3.4 GAS SUPPLY

Three gases are required in general to address different tasks in laser welding: the shielding gas for air displacement on the welding zone to prevent atmospheric contamination of the fused metal before solidification and consequent severe loss of ductility; the assisting gas to remove plasma; and the compressed air cross-jet to be blown at the laser beam exit, at a proper height which would not interfere with fusion and gas shielding, in order to protect the optics from vapors and metal spatters [18]. Additionally, root shielding is required for the back-side when deep penetrative welds are produced [10]; however, when welding inside narrow devices, bead shielding may naturally result from metal vapor itself, so no supplementary flux would be needed [18].

A basic scheme for the suggested set-up is shown in **figure 3.4**; minor changes apply depending on the metal being welded and the joint geometry. The

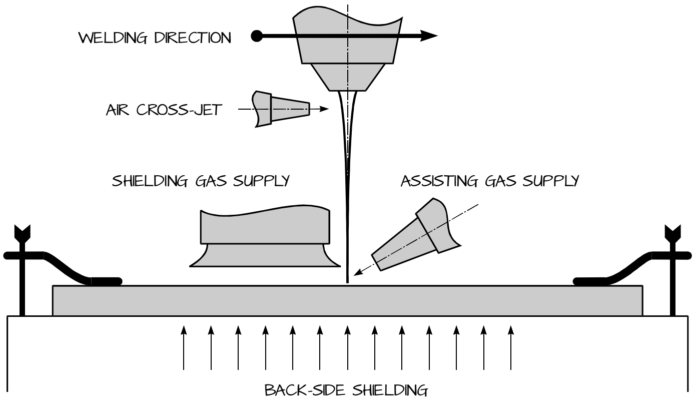

**FIGURE 3.4** – Basic scheme for laser welding set-up

extent of the welding zone to be gas shielded must be increased for reactive metals such as titanium, niobium or zirconium, being them particularly sensitive to air contamination when in fused state.

When providing high irradiances as required for metal welding, laser beams interact with both the metal vapors and the shielding gas, thus inducing a cloud of plasma above the joint. This plume may hinder the optimal energy transfer from the beam to the pieces to be welded [10]. Plasma is indeed a thermally excited state of matter where a certain portion of molecules or atoms are ionized as a consequence of heating up [42]; the required energy to remove electrons and produce plasma is typically measured in electron volt units and is referred to as the ionization potential. In this sense, it is deemed to be an indicator of reactivity. It depends on the atomic orbital; in particular, the first or initial ionization potential is required to remove the most loosely bound electron from a gaseous atom and has therefore to be considered in order to compare the aptitude to produce plasma. Values of first ionization potential for common gases and metal vapors [5] which are often involved in laser welding are listed in **table 3.1**.

Suppression of plasma over the welding zone is critical in order for the laser beam to reach the joint with minimal interruption, thus improving the bead quality and enhancing uniformity in penetration depth. Otherwise, the beam energy would be absorbed outside of the key-hole [43] because a highly grown

**TABLE 3.1 –** Values of first ionization potential for common gases and metal vapors

| **Material** | **First ionization potential [eV]** |
|---|---:|
| Helium | 24.46 |
| Argon | 15.68 |
| Neon | 15.54 |
| Nitrogen | 15.51 |
| Carbon dioxide | 14.41 |
| Water vapor | 12.56 |
| Oxygen | 12.50 |
| Iron | 7.83 |
| Magnesium | 7.61 |
| Nickel | 7.61 |
| Manganese | 7.41 |
| Chromium | 6.74 |
| Aluminum | 5.96 |

plume affects the refractive index over the specimen being welded, so that the laser beam is consequently defocused, deflected, refracted or inclined [44]. Not surprisingly, it has been proven that a reduction in penetration depth would result from very low speeds, due to enhanced vaporization with consequent amount of plasma and attenuation in the incident laser beam [10].

Therefore, several techniques have been developed to remove plasma from the welding zone or, alternatively, to reduce it. Pulsing laser power at high frequencies above 1 kHz was proven to be effective in reducing plasma formation with $CO_2$ lasers [10]. However, common feature in laser welding systems is an auxiliary jet of gas flowing coaxially with the laser beam or impinging on the laser focus from the side [2, 5]. It is not unusual to have both coaxial and side copper nozzles [2, 45]. Under certain conditions, the transverse flow of assisting gas may also act for plasma blow [18].

### 3.4.1 GAS CHOICE

A gas which is even slightly reactive with the weld metal may result in a thin oxide film [5]. Inert high purity gases such as argon, helium and nitrogen are therefore required for the sake of beam quality. Since low impurities are usually residual, a code is considered to designate the gas supply: the chemical symbol of the gas is followed by two figures, the first one accounting for how many 9 write the purity volume percentage, plus the last figure of the percentage itself [18]. As an example, He 4.6 is the code for 99.996% in volume pure helium.

Interestingly, the bead cross-section is strongly influenced in shape by the specific gas [18], as shown in **figure 3.5** for key-hole welded metals. It is clear anyway that any gas to be supplied for shielding or assistance must be chosen referring to its ionization potential and the processing temperatures. Helium is preferred, in spite of its price, as the best choice in laser welding, having it a

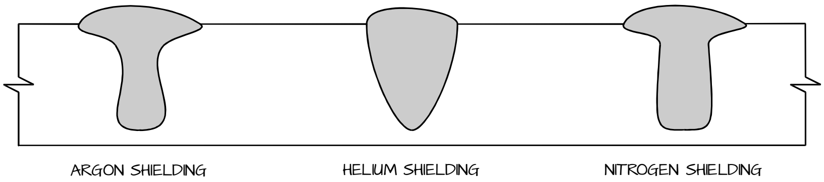

**FIGURE 3.5** – Shielding influence on bead cross-section for typical inert gases

higher ionization potential, thus being more resistant to plasma formation [2]: the plume hence only consists in metal vapors from the key-hole inlet, whilst additional shielding gas plasma is formed when using argon or nitrogen [44]. Conversely, underneath shielding in deep penetrative welding beads is performed with cheaper gases such as argon, nitrogen or carbon dioxide since no interaction is in place between the laser beam and the gas [5]; helium must be preferred when possible anyway, as it raises to the surface of the work-piece when introduced from below [2]. Nevertheless, argon normally provides an ideal compromise between effectiveness and economic needs in industrial environments. Counterproductive low density affects high ionization potential gases, so high consumption rates result as they rapidly spread compared with heavier gases [18]; furthermore, they may not be adequate for effective air displacement under certain welding conditions where the process is being conducted at high speeds. Therefore, mixture of different gases, such as 90% helium with additional 10% argon, are usually employed in critical processing conditions [46].

### 3.4.2 GAS SUPPLY DEVICES

Special care is normally required for nozzle positioning and geometry for gas supply when designing a shielding and assisting device for laser welding [47]. In particular, any system for gas supply must give total coverage of the bead; laminar fluxes which would not result in vortexes or waves on the weld pool must be provided, otherwise air would be driven into the welding zone, thus affecting the bead quality [5, 18].

Flow effects are a strong function of nozzle geometry; therefore a variety of designs for nozzle have been developed [2]; furthermore, a variation in the environment pressure of both the assisting and shielding gas has a significant effect on penetration, particularly at very low pressures [5]. The assisting gas is usually delivered with a tilting angle of approximately 30 to 60° with respect to the work-piece surface [10]; flow rates commonly range from 10 to 40 l/min, depending both on the material being welded and the processing speed; the highest rates are usually employed for high speed welding, up to 150 mm/s [2].

In order to perform optimal shielding, a proper waiting time must be set before starting the welding process, so to allow the gas to adequately prepare the welding zone. Once the laser beam has been switched off, gas shielding must be further supplied for additional but shorter waiting time, as to prevent oxidation of the weld pool. Beam discoloration is deemed to be a good indicator [48]: no shielding at all on titanium alloys results in grey discoloration, whilst blue or yellow spots reveal improper flow rate or device positioning; appropriate shielding produces uniform, smooth and shiny beads [18].

## 3.5 FOCUSING

When focusing the beam at the surface of the work-piece, good results and welding performances are expected because the highest possible irradiance is supplied. However, this is often not the case [2]. There are suggestion indeed that welding in defocused conditions may result in lower porosity or enhanced penetration depth [2, 5] since the beam focus locates inside or outside the upper surface of the joint to be welded. In particular, welding is told to be carried out with positive or negative defocusing when the beam focus is above or beneath the upper surface of the work-piece, respectively.

Although a laser beam is symmetrical about its waist, different material responses are achieved when the same defocusing shift is set in positive or in negative direction [4]. Once the supplied irradiance approaches the threshold value to start a key-hole, the actual material response depends on the size of the weld pool, whose surface is depressed towards the hole tip by the recoil force of evaporation. When positively defocusing, the beam inside the hole is divergent and the depression moves the liquid surface away from the focus point, so the irradiance decreases and the cavity is hindered from further growth; conversely, when negatively defocusing, the beam is convergent inside the hole and the depressed liquid surface is further exposed to increasing irradiance. Therefore, once a shallow key-hole is produced with negative defocusing, it has a clear tendency to grow into a deeper one [49]. It has also been suggested that an increase in penetration depth with negative defocusing also occurs due to enhancement in multiple reflections [2, 44]. Obviously, optimal focusing depends on the material to be joined, although defocusing ranges are usually in the order of few millimetres anyway.

Nearly the same results are often obtained at locations near the focus: this is especially true when the focusing system has a large depth of focus [2], such that the beam divergence is effectively low and the diameter expansion is restrained along the propagation axis. Hence, focusing becomes critical with any optical system with short depth of focus, because even a small change in the focus plane position results in large changes in beam irradiance.

However, it is good practice to check the focus position via preliminary procedures before conducting any welding test, irrespective of the focusing optics being used for the process [4]. Different methods of focus positioning are suggested in literature to locate the focus plane: the basic idea is to analyze the beam profile on both sides of the focus point because the beam irradiance decreases along the propagation axis in either direction away from the focus, as a consequence of beam divergence [2]. Beam profilers with different measurement principles with cameras or rotating knife edges or slits, as well as Shack-Hartmann sensors which consider wave-front properties so to find the beam waist where the wave-front is planar, are usually employed [23].

As an alternative which is capable of being carried out without any special assisting device, an array of welding spots is performed via rectangular pulses on an anodized aluminum sheet, by moving the laser head along the beam propagation direction, with constant peak pulse power and time. Welding parameters are tuned in order to only produce vaporization of the upper layer: the distance between the laser head and the sheet is changed from one pulse to the next one; therefore, spots of different extent are produced. Resulting diameters are measured via optical microscopy: the idea which drives the procedure is that the focus point exactly locates on the surface of the sheet when the minimum diameter is achieved on the corresponding welding spot [18]. Similarly, the procedure is capable of being carried out on thermal paper to fine tune the measurements. This procedure eventually checks the focus position or, alternatively, finds which basic position has to be considered to further defocus the beam.

### 3.6 BEAM ANGLE

Tilting the laser head, as shown in **figure 3.6** with usual convention of positive anticlockwise angles, or alternative tilting of the work-piece, in the order of few degrees, is common practice for highly reflective metals such as aluminum and copper, so to prevent back reflections from entering the optics train [2, 5]. Indeed, for a law of reflection, the angle which an incident ray makes with the normal to a reflective plane equals the angle which the reflected ray makes with the same normal, so a specular reflection results with respect to the normal [25]; hence, a normal incident beam which is not absorbed on the metal surface is back reflected into the optics.

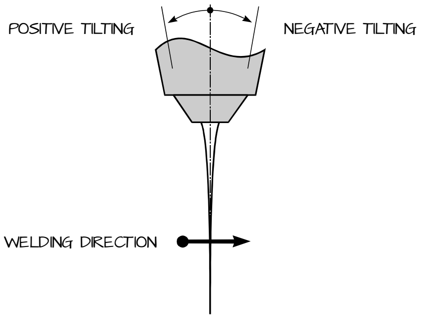
POSITIVE TILTING
NEGATIVE TILTING
WELDING DIRECTION

**FIGURE 3.6 –** Laser head tilting: angle convention

Nevertheless, it has also been reported that a forward or backward tilting irradiation with respect to the welding direction may change the amount of metal dropping at the back-side in deep penetrative welds, as well as alter the formation of spattering on the top surface of the sheet when welding steel [50]. A side angle has been found to be crucial in increasing both the penetration depth and the bead width [51].

# 4

# BEAD CHARACTERIZATION

## 4.1 INTRODUCTION

Discontinuities in the weld or possible deviations from the intended geometry are welding imperfections, whose classification and extensive description are provided by international standards, which in general do not include metallurgical defects because they must be discussed on a case-by-case basis. Reference quality levels are usually settled depending both on the material and the welding application: imperfections which do not meet the standard, result in being welding defects. Six groups of imperfections are defined [52]: cracks, cavities, solid inclusions, lack of fusion and penetration, imperfect shape and dimensions, miscellaneous imperfections such as discoloration or spattering which cannot be included in previous groups.

In order to compare different welding conditions, specific procedures are performed to examine the imperfections via non destructive tests; moreover, the beads are then sectioned to allow measurements on their shape and cross-section, as well as the evaluation on their metallurgical and micro structural properties [2]. Energy dispersive spectrometry, mechanical destructive tensile and bending testing eventually assess the quality.

## 4.2 SEAM GEOMETRY

Flexibility in laser beam positioning allows new possibilities for joint design. Nevertheless, similarly to any other welding technology, a number of basic seam geometries to be laser welded can be identified, as shown in **figure 4.1**.

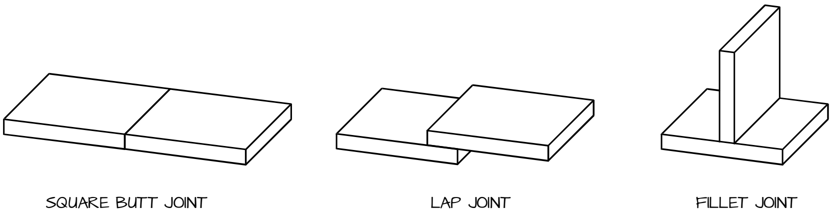

**FIGURE 4.1** – Basic seam geometries in laser welding

Square joints in butt configuration are common in several application. Beveling is not performed, but primary fit up is critical, given the need to minimize any gap between the plates. In this sense, tight focusing of laser beams has its drawbacks since even small misalignments of the surfaces to be joined can cause significant changes in the welding conditions as a consequence of reduced heating efficiency. It has been suggested that the laser beam should overlap both sides of a butt joint and should not wander off the centre-line by more than 10% of the beam diameter [2]. Therefore, clamping to maintain fit up is critical; also, it helps as the welding process develops because two abutting plates have clear tendency to misalign during fusion due to thermal stresses and distortion.

Lap joint is the second main configuration and is required in aerospace industry as well as in consumer goods such as cars or washing machines. Two plates are joined while overlapped in parallel planes. Clamping is less critical, although special care must be taken in order to prevent gaps between the overlapping plates, as burn-through may occur otherwise [53]. With respect to this geometry, riveting and adhesively bonding are traditional methods in aerospace, whilst resistance spot welding by the use of force and current is the choice in automobile industry, due to economic reasons, although being primarily employed on steel sheets [54]. Because of natural aging, both riveted and adhesively bonded aircraft lap joints can be affected: cracks from rivets, voids or corrosion usually occur [55].

When plates are joined with a 90° angle, T-joints or corner joint are produced. Because the welding bead is basically used to fill the area where the plates meet, the geometry is also referred to as fillet weld. Beveling is suggested such that a proper preparation allows the welding process to better penetrate the joint.

A separate mention is given to bead-on-plate (BOP) welding which are normally performed before starting a proper experimental plan: fusion is achieved on the upper surface of the metal being investigated, with no actual joining, aiming to both set a range for the processing parameters and portray a general response in the most simple condition, with no complication of fixturing and joint alignment.

## 4.3 NON DESTRUCTIVE TESTS

Visual inspections are normally conducted just after welding to check the joint penetration and the effectiveness of shielding, considering possible bead discoloration on top- and back-side surfaces [56]. Oxidation-affected or fusion-lacked beads are thus excluded from further procedures of characterization.

Then, much more accurate testing methods, which do not impair any future usefulness of the component to be examined, must be carried out. A number of techniques are available [57], although only some of them are specifically used when testing welded joints. In particular, surface-breaking defects in the bead such as cracks, pores or leaks are detected via dye penetrant inspections [58] which are simple and low-cost. Generally feasible for non porous materials even after casting or forging, the method is based on the principle of capillary action. A low surface tension fluid seeps into any breaking discontinuity, and once adequate time has been allowed for the liquid to effectively penetrate the surface, the excess penetrant is removed; flaws are drawn by a proper developer, ultraviolet or white light depending on the dye being used, fluorescent or non fluorescent, respectively. Fluorescent penetrant inspections (FPI) are generally preferred because the dye is particularly sensitive to smaller flaws compared with any other non fluorescent one.

Nevertheless, penetrant inspections are limited to surface imperfections, so they only offer a first stage analysis. Further checks are then performed via radiographic tests (RT). An X-ray machine or a radioactive isotope is used as source of radiation; the beam is directed through the part to be examined, which is placed between the source and the detecting film device. Rules for positioning and exposure apply [59]. The energy which is not absorbed by the part being examined exposes the film; therefore, the result is a two-dimensional X-ray transmitted image of the part onto the processed film: discontinuities such as inclusions or pores are detected by shape and variation depending on the amount of radiation in each area, similarly to medial radiography for broken bones; eventually, a permanent film record for weld quality is provided. Pores, wormholes, elongated cavities and solid inclusions are detected. Acceptance levels for each type of internal indication are decided in accordance with the referred normative [60, 61], depending on the material to be examined.

## 4.4 SAMPLE PREPARATION

Metallography is the referred science and art to prepare a metal surface for proper analysis. A series of operations on representative specimens are conducted with specific tools and procedures, depending on the material to be examined [62]. In sequence, the overall procedure includes cutting, mounting, mechanical preparation via grinding and polishing, then etching and eventual microscopic examination. A compromise must usually be taken between time, resources, and the purpose of the investigation. As an example, a research laboratory can significantly benefit from an extremely time consuming vibratory polishing, which would not be suitable, on the other hand, at quality control stages in industrial environment [63].

### 4.4.1 CUTTING

A plane surface, with as little deformation as possible, is required to facilitate and expedite further preparation. A cut of the bead cross-sections is generally produced when investigating the welding output.

Abrasive cutting wheels or precision saws are commonly used: blades are much thinner than abrasive wheels; as a consequence, loads are much lower. Nevertheless, abrasive cutters are the most widely used, provided that the correct wheel for the specific application is selected. Moreover, face-centred metals readily deform and work harden; consequently, any aggressive sectioning method introduces considerable damage which are unlikely to be removed in the subsequent steps of preparation [64].

As modern engineering materials develop, so does the demand for proper technologies for cutting. Diamond and boron nitride abrasive wheels are capable of sectioning through hard metals as well as composite materials, glass, plastics and mineral fibres. Whether a diamond or a boron nitride wheel is to be used, essentially depends on the hardness or brittleness of the sample

[62]. Since a heat-damaged zone may significantly alter the metal structure, suitable cutting fluids must be supplied: cooling both prevents sample deformation and washes metal debris away; surface roughness is reduced and the operating life of the wheel is extended in turn.

### 4.4.2 MOUNTING

Metallographic specimens are typically embedded in resins. The procedure is of mere convenience to handle the sample to be observed; moreover, the back of the mount is an ideal surface for labels to record the testing conditions [64]. The process is performed via hot or cold mounting: whichever the mounting procedure, any specimen must be properly degreased and dried to ensure adequate adhesion of the mounting media [63].

Thermosetting polymers in form of powder are used in a typical hot mounting cycle: the examination surface is face-down placed in the mounting ring, as shown in **figure 4.2**, where the polymer compound is poured; compression up to 30 MPa and heating up to 180 °C apply. Thermoplastics can be alternatively considered as mounting media, but longer heating and cooling times are required for polymerization, although the mounting mean can be melted again at any time, unlike thermosetting polymers [62]. Mounting presses which automatically cool back the specimen to room temperature when under pressure, are capable of reducing the occurrence and degree of shrinkage gaps, such that best edge retention is achieved [64]. Specimens which are very sensitive to pressure or temperature are cold mounted; usually the procedure

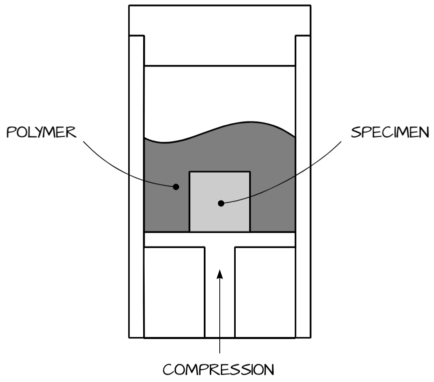

**FIGURE 4.2 –** Mounting ring for hot mounting cycle

is favoured when samples of irregular shape and size must be embedded and the acquisition of a mounting press is not economically justifiable. However, use of an improper mounting media can produce rounding of the interface between the mount and sample, thus resulting in poor edge retention [63].

### 4.4.3 MECHANICAL PREPARATION

Mounting provides a safe, standard and ergonomic way to hold a specimen during mechanical preparation, which consists in grinding and polishing operations to be carried out to reveal the metal structure for microscopic evaluation. Many detailed steps are required, the first ones being equipment dependent, the last being driven by the needs of the investigator [63].

Abrasive silicon carbide (SiC) papers are used in successively finer steps to remove material from the surface of the specimen until the required quality is achieved. As a rule, when moving from one grinding step to the next one, half the grit size of the previous stage must be used. Standard designation for grinding paper as a function of the grain size [62] are listed in **table 4.1**, according to both the Federation of European Producers of Abrasives (FEPA) and the American National Standards Institute (ANSI).

Samples should be turned 90° after each stage in manual preparation, until any

**TABLE 4.1** – Standard grain size for grinding paper: FEPA and ANSI designation

| FEPA designation | Grain size [μm] | ANSI designation | Grain size [μm] |
|---|---|---|---|
| P60 | 269 | 60 | 268 |
| P80 | 201 | 80 | 188 |
| P120 | 127 | 120 | 116 |
| P180 | 78 | 180 | 78 |
| P240 | 58 | 240 | 52 |
| P320 | 46 | | |
| P400 | 35 | 320 | 34 |
| P600 | 26 | | |
| P800 | 22 | 400 | 22 |
| P1000 | 18.3 | 500 | 18 |
| P1200 | 15.3 | 600 | 15 |
| P1500 | 12.6 | 800 | 12 |
| P2500 | 8.4 | | |
| | | 1200 | 6.5 |
| P4000 | 5.5 | | |

grinding mark resulting from the previous step is no longer visible; hence, frequent observation via optical microscopy are suggested from step to step. On the other hand, when semi or fully automatic grinding, the change in direction results from the relative motion between the rotating platen and the sample holder, such that omni directional grinding patterns and superior flatness are produced. Unless specimens are porous or contain cracks, simple washing between the grinding steps is adequate; otherwise ultrasonic cleaning with suitable solvent is required [64].

After correctly performing the grinding steps, polishing is conducted in the traditional preparation method, with different diamond suspensions from 9 µm down. The time for each run ranges from 60 to 120 s; the wheel speeds are generally lower compared with grinding processing [64]; cleaning between the polishing steps must be carefully performed. Fine polishing is accomplished with 0.3 and 0.05 µm alumina abrasive sizes. Nevertheless, various methods are recommended. Vibration is the suggested solution for research, although processing times from 1 to 16 h are usually required. A scratch-free mirror finish, with minimal deformation resulting from the metallographic preparation process is eventually achieved. An optimal cutting at the previous stages of the procedure allows the specimen to be prepared in fewer steps and shorter time; as for example, most ordinary metal samples which have been properly sectioned are effectively ground with single 220 grit finish followed by a 9 µm diamond suspension [63].

Since the preparation should be accomplished systematically and according to reproducible methods, specific procedures with adequate grinding abrasive papers and polishing cloths have been developed, depending on the material to be prepared. Care must be taken so that the hardness of the surface to be tested afterward is not affected [65].

### 4.4.4 CHEMICAL ETCHING

A number of choices are possible to favour the relevation of either the metal microstructure or the bead boundaries. Therefore, both the chemical etchant and the proper etching time depend on the alloy and its starting heat treatment condition. As general rule, it has to be considered that a shorter etching time reveals more details, whereas a longer one ends up in more contrast; therefore, as the etching time increases, details are lost in contrast. Underetching is deemed to be better than overetching [63]. Moreover, it is also critical not to swab the specimen after etching because any contact would disturb the surface; blow drying with compressed air jet is preferred.

The fused zone is clearly noticeable in the cross-section after chemical etching, and the imperfections and the heat affected zones can then be examined. The macro structural examination then provides useful information about the general response of the material in the process; micro structural examination reveal grain shapes as well as possible segregation and precipitation instead, although the analysis is usually quite complex due to the potential for a variety of phases which can be formed by heat treatment of welding.

### 4.5 IMPERFECT SHAPE AND DIMENSIONS

An assessment of the geometry of the bead cross-section usually starts with the evaluation on the crown width ($CW$) and the root width ($RW$) at top- and back-side, respectively; additionally, the extent of the fused zone ($FZ$) is measured, as shown in **figure 4.3**. In fully penetrative welding conditions, the bead width at the top-side is generally larger than the one at the back-side [2].

Several designations for the imperfections in the shape of the cross-section are provided in the referred literature about welding [52]. Although the actual bead profile strongly depends on the shielding conditions and the metal being welded, a number of common imperfections must be addressed, as shown in **figure 4.4**. Undercuts are irregular grooves at the weld toe; when visible at each side of the root side they are intended to be shrinkage grooves. Reinforcement is any excess weld metal at the bead crown; when measured at the root side it has to be intended as excessive penetration or drop-through. Incompletely filled groove or low weld results from longitudinal continuous or intermittent channel at the bead crown due to insufficient deposition of weld

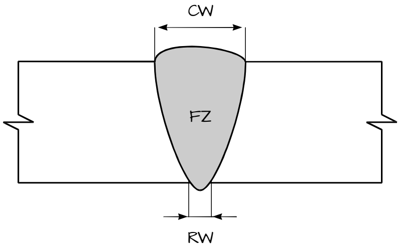

**FIGURE 4.3 –** Designation for crown width, root width and extent of the fused zone

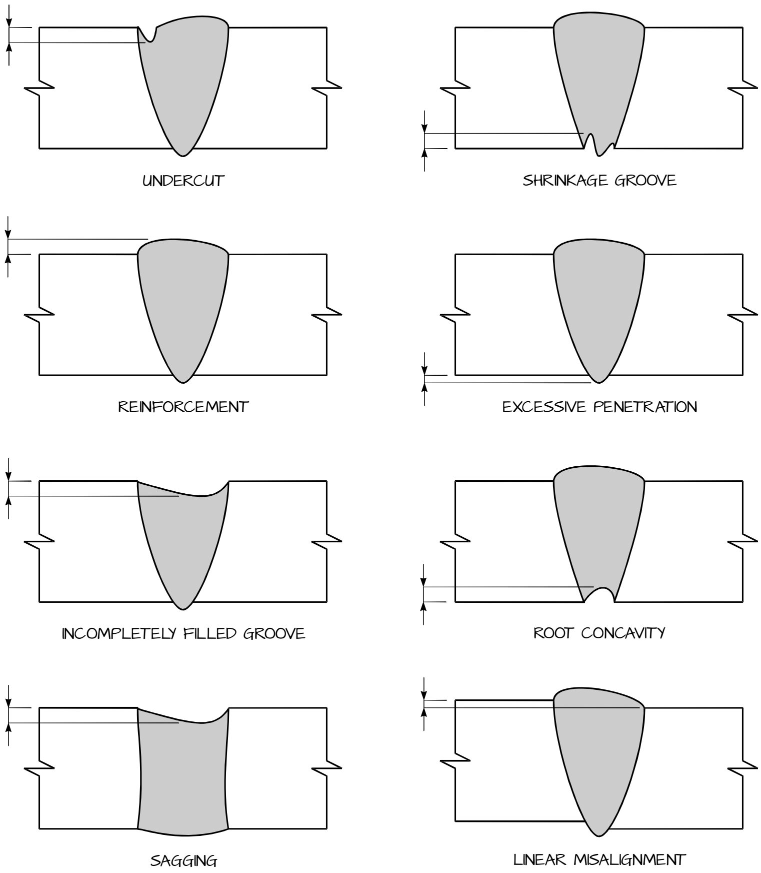
UNDERCUT
SHRINKAGE GROOVE
REINFORCEMENT
EXCESSIVE PENETRATION
INCOMPLETELY FILLED GROOVE
ROOT CONCAVITY
SAGGING
LINEAR MISALIGNMENT

**FIGURE 4.4** – Common imperfections for bead quality assessment

filler material; shallow groove due to shrinkage of a butt weld at the root side is root concavity or under-fill. Weld collapse due to gravity, so that incompletely filled groove is produced as a consequence of melt-through, is considered to be sagging. Linear misalignment may result from improper clamping, rather than from inadequate processing conditions.

The ranges to be fulfilled for each imperfections depend on the category to be matched. It would normally be hoped that the same quality level would cover the limits for any imperfection in the same joint; nevertheless, certain applications such as fatigue loading or leak tightness allow different categories to be specified in the same bead, so that the overall joint quality level could be defined by the application standard on a case-by-case basis in conjunction with the concerned parties [66].

## 4.6 ASSESSMENT OF THE HEAT AFFECTED ZONE

Welding thermal cycles, with rapid heating and cooling, result in changes in the original structure of the material [43]; therefore, new properties and micro structures are expected across the welding zone and a number of distinct regions are identified. Interestingly, due to phase transition at high temperatures, any welding process is expected to produce a heat affected zone (HAZ) at the interface between the fused zone and the base metal, as shown in **figure 4.5** for a generic welding bead in butt joint configuration. The HAZ is therefore intended to be any fraction of base material which has not been melted, but has been altered in turn by the heat source of welding.

The actual extent of the HAZ is a consequence of both the processing condition and the diffusion phenomena. It must be quantified in order to consider possible undesirable micro structural changes in the material; residual stresses are usually found and brittle intermetallic phases may be produced also.

Depending on the metal alloy being examined, a reasonable highlight of the HAZ usually results as a consequence of proper chemical etching; nevertheless, as general method for persuasive assessment, the Vickers micro hardness is measured across the welding zone. The basic idea is that, as softening or hardening occurred, the indentations are affected in size and a trend in micro hardness is therefore expected to be noticed compared with the base metal.

According to the referred specification [65], tests can be conducted in the form of both row indentations or individual ones, at room temperature unless otherwise specified. A suitable indenting load and an efficient number of indentations are required to ensure that the unaffected base metal is effectively tested to clearly define the hardness trend. Nevertheless, when row testing the welding zone, in order to prevent the influence of deformation which is possibly induced by previous indentations, a minimum distance of not

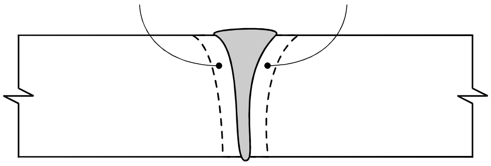

**FIGURE 4.5** – Heat affected zone in butt welding cross-section

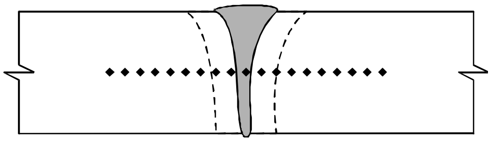

**FIGURE 4.6** – Vickers testing row for micro hardness testing in the cross-section

less than 3 times the mean diagonal must be allowed between the centres of consecutive indentations [67]. Moreover, for specimens whose thickness is below 4 mm, rows of indentations must be produced at mid thickness. The resulting Vickers testing row is shown in **figure 4.6**. Hardness values are thus recorded as a function of the corresponding position of the indentation, and the trend is discussed with reference to the local micro structure.

## 4.7 ENERGY DISPERSIVE SPECTROMETRY

A valuable tool to investigate the bead cross-section from a chemical point of view is energy dispersive spectrometry (EDS). A site of interest on the specimen is chosen and the corresponding elemental composition is examined [68, 69]. Volumes which are as small as 1 µm in diameter are capable of being explored. When referring to welding, this allows to investigate on possible loss of the alloying elements as a consequence of heating and vaporization.

An EDS system works as an integrated feature of a scanning electron microscope (SEM) and an electron beam is employed to scan the exposed specimen: any vacating position of the ejected electrons of the inner shell is eventually taken by the electrons of higher energy from the outer shells, thus resulting in energy emission as X-rays. The amount of released energy depends on which shell the transferring atom comes from; hence, depending on the element, a specific energy release occurs and the identity of the emitting atom can be easily established. A silicon or germanium crystal is used for X-rays detection and is kept in vacuo at liquid nitrogen temperatures.

The output of an EDS is a two-dimensional continuous EDS spectrum: each peak corresponds to the energy levels the X-rays are received from. Each peak is hence unique to an atom: a qualitative analysis is first performed to find which elements are present; a quantitative one then measures the specific concentration of the elements, based on the assumption that the higher a peak is in the spectrum, the more concentrated is the element in the specimen.

EDS is best suited for metal alloys, ceramics and minerals. All of the elements from atomic number 4 to 92 can be detected in principle, although the instruments are not generally equipped for light elements below 10. Moreover, since a shallow depth is involved in the electron probe analyses, the specimens should be adequately polished such that the surface roughness does not affect the results. The preparation of the sample is hence essentially as for reflected light microscopy, provided that only vacuum compatible materials are used; opaque samples are embedded in epoxy resin blocks; for transmitted light viewing, polished thin sections on glass slides are prepared.

## 4.8 TENSILE TESTS

In order to test a square butt joint configuration, flat specimens with proper shoulders to be placed between the jaws of the testing machine must be milled from pre welded samples. Standard dimension apply, in accordance with the referred specification [70, 71], although the total length is chosen to suit the testing machine.

Machining must be performed in such a way that the welding axis remains in the middle of the parallel length of the specimen, as shown in **figure 4.7**. No change in the properties of the metal are acceptable in the extraction of the sample; therefore, shearing or thermal cutting are excluded in general. Moreover, no heat treatment is allowed unless otherwise specified by the relevant application standard; surfaces shall be free from scratches or notches.

Then, usual procedures for tensile testing are conducted [72], with an increasing load which is continuously applied in perpendicular direction with respect to the welding bead, until rupture occurs; both load and displacement

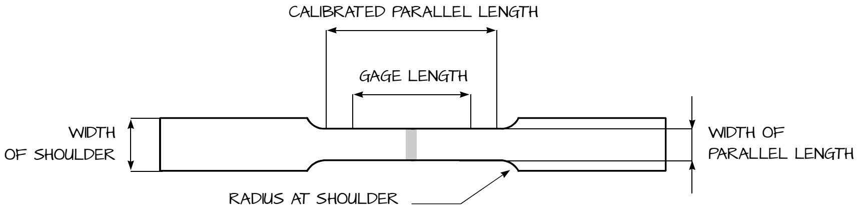

**FIGURE 4.7** – Tensile specimen for square butt joint testing

are measured, then usually converted to stress and strain, respectively. Non welded specimens with the same dimensions are tested also, for a comparison of the results. The location of fracture, the ultimate tensile strength (UTS), the yield point and the percent elongation at break are reported. Possible existence of any imperfection within the fracture surfaces which may have adversely affected the test have to be recorded, including their type, size and quantity.

# 5

# MODELING AND OPTIMIZATION

## 5.1 INTRODUCTION

Many variables and sub processes concerning fusion and vaporization are involved in laser welding. A primary goal of research is therefore to identify the adequate ranges for the processing parameters in order to manage both the stability and the reproducibility of the overall process [2]. Moreover, to accurately predict the welding geometry, various methods to obtain the desired output variables throughout models development have been suggested. Among them, the design of experiment (DOE) is deemed to be the most important and efficient procedure for a systematic study to yield valid and objective conclusions and has been therefore adapted for many applications in different areas [13].

As general rule for a new process to be effectively portrayed, a series of structured tests are designed so that planned changes are made to the input variables; the effects are then investigated. Both the governing factors and the crucial responses to be discussed are defined in advance [73]. The choice is usually based both on literature and past experience on similar subjects.

## 5.2 DOE PRINCIPLES

The most simple way to build an experimental plan is testing with one-factor-at-a-time approach, such that changes are made to only one factor, the others being hold as constant. This may lead to find one input variable to have a significant effect on the response, while failing to perceive any dependence or interaction among the governing factors; also, several runs would be needed for adequate precision to be achieved in the estimation of the effect [74]. A much more efficient method to study two or more factors affecting an output is their simultaneous variation. Hence, the one-factor-at-a-time approach is usually rejected in favour of a DOE: a judgement on the input variables acting in combination with one another is addressed. Therefore, designed factorial experiments are required when dealing with general issues such as searching for the main contributing factor or the best parameters combination to minimize the variation in a response, with the aim of robust design as defined by Genichi Taguchi as well.

For each input variable, a number of levels are defined within a range where the effect is desired to be known. Design description and analyses are then referred to coded factor, such that each range is reduced to a common scale, irrespective of the actual relative magnitude. Typical coding shifts the outer limits of the governing factor so to range them from -1 to 1, with 0 as the intermediate level.

In terms of resources, the exact length and size of the experiment are set in advance. When considering two levels, an implicit assumption is made in considering the response to be linearly dependent on the input factors. Three or more equally spaced levels are then usually employed.

Actually, in order to draw the highest amount of information, a full matrix is required to contain all of the possible combinations of factors and levels. When this leads to many experimental runs to be performed, fractions of the matrix are considered, depending on which the interesting effects are, aiming to reduce the amount of testing; fractional plans hence result. Nevertheless, the fewer are the runs, the less information is available to take reasonable account of any interaction. As usual practice, three rules are suggested [73]: replication, randomization and blocking. Tests are replicated to naturally evaluate the statistical dispersion, whilst measurements are replicated on the same item when assessing the experimental error in performing data analysis. Randomization in both sample allocation and run order is needed to restrain any possible systematic error, thus satisfying the statistical requirement of independence of the observations. Moreover, when placing tests into blocks whose experimental runs are similar with respect to a certain factor, a reduction in noise effects is achieved; this is deemed to be significantly helpful when all of the experiments cannot be carried out in one single day or with a single batch of material.

## 5.3 TESTING SCHEMES

Many solutions are available to arrange an experimental plan [73]. A central composite design (CCD), provides a solid statistical foundation for the estimation of a curvature and, hence, a response surface map [75].

Referring to a fractioned 3-factor study, the combinations to be tested are placed on the vertexes of a cubic scheme, plus the central point condition; this structure effectively addresses a first order model. In addition, a group of star points or axial points are equally placed in the domain, as shown in **figure 5.1**, aiming to develop a second order model. An extended range with five levels is then investigated.

Specific schemes are obtained from this basic structure, depending on the distance between the centre and the star points. In particular, a circumscribed CCD results when considering a distance which is equal to the square root of the number of factors; hence, a spherical testing plan is achieved since the vertexes and the star points locate on a spherical surface. Rotability of the design is benefited, as the variance of the responses remains unchanged upon rotations of the design points about the center; this feature is generally useful when an optimization has to be carried out afterwards on the responses, since the location of the optimum is unknown before, and a plan with equal precision in any direction is preferred [73]. Alternatively, when no interest is addressed to the outer domain due to possible limits of the system, a distance which is equal to half the cube side length is considered: a face-centred CCD, as shown in **figure 5.2**, is obtained; rotability is clearly lost, although the

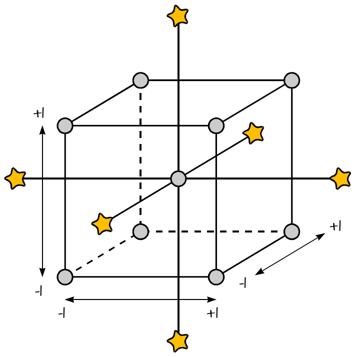

**FIGURE 5.1** – CCD structure: testing condition in a fractioned 3-factor study

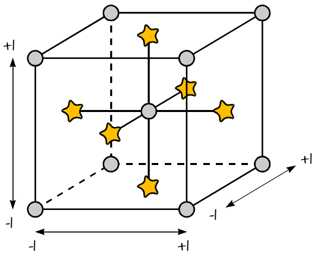

**FIGURE 5.2 –** Face-centred CCD structure: testing condition in fractioned 3-factor study

effectiveness of the plan is not significantly affected. Nevertheless, irrespective of the structure, three to five additional runs must be planned for the cube central point condition, so to benefit from a much more stable variance of the responses and effectiveness in estimating any second order effect [75] because a proper number of degrees of freedom are thus provided to statistically test the model. For the same reason, specific points of the design are suggested to be additionally run when a better estimation of the response is required in the corresponding area of the testing domain.

When combinations of the outer limits of the processing ranges yield to prohibitively expensive or demanding conditions on the cube vertexes because of possible physical constraints of the process, a Box-Behnken plan is alternatively suggested instead of a CCD scheme: the testing point conditions are placed on a cubic scheme anyway, although only the intermediate combinations of the levels are considered, such that the vertexes are not included, as shown in **figure 5.3**. Namely, the testing points are placed on a spherical surface whose radius is equal to the square root of 2; rotability is benefited although only three levels are involved.

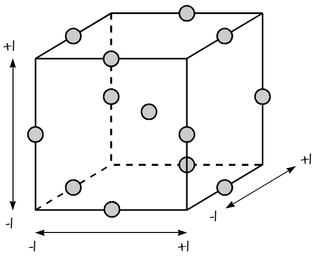

**FIGURE 5.3 –** Testing condition in a Box-Behnken plan

## 5.4 REGRESSION MODELS

The response surface methodology (RSM) is employed to develop proper models to portray the effects of the input parameters on the referred results. The approach was first introduced in the fifties and then grew in physics, chemistry and engineering. With respect to welding, a comprehensive literature review of the application of RSM is available [76]; the bead size, the weld strength and the cost optimization are generally addressed. The main goal is to generate a map of response, either in the form of contours or as a 3D rendering [75]. For the purpose of the procedure, polynomials are fitted to the experimental data to obtain the regression equation of the responses. Each dependent output $Y$ can then be written as:

$$Y = f(x_1 , x_2 , \dots , x_k) + \varepsilon \tag{5.1}$$

since a number of $x_i$ values of $k$ factors are combined to give the response; a residual $\varepsilon$ accounts for the difference between the actual value and the prediction [77]. The most common fitting function $f$ takes either a linear or a quadratic form. The general expression of a quadratic model is:

$$Y = a_0 + \sum_{i=1}^{k} b_i \cdot x_i + \sum_{i=1}^{k} c_i \cdot {x_i}^2 + \sum_{i=1}^{k} \sum_{\substack{j=1 \\ j \neq i}}^{k} d_{ij} \cdot x_i \cdot x_j + \varepsilon \tag{5.2}$$

where linear, square and interaction terms are involved, respectively. Namely, when different groups of input changes are considered, the response variable is capable of being influenced by single effect, resulting from the input variables acting alone, or interaction as well, resulting when combinations among the input variables are in place. A full model should include the interactions in the form of cross-products; higher order components are generally less significant, so fractional plans are effective in portraying the process as a second order one. As a guide, the number of coefficients which are required to be estimated in linear, quadratic and cubic models for a given number of factors are listed in **table 5.1**.

To select the best model via automatic procedures, a collection of sequential statistical tests to be performed are provided by the analysis of variance (ANOVA) in its most simple form; a step-wise regression approach results. The observed variance for a certain variable is partitioned into several components and each one is related to different sources of variation [78].

**TABLE 5.1** – Number of coefficient for linear, quadratic and cubic models

| Number of factors | Linear model | Quadratic model | Cubic model |
|---|---|---|---|
| **2** | 3 | 6 | 10 |
| **3** | 4 | 10 | 20 |
| **4** | 5 | 15 | 35 |
| **5** | 6 | 21 | 56 |
| **6** | 7 | 28 | 84 |
| **7** | 8 | 36 | 120 |

This allows to effectively chose the significant terms in the model since individual statistics are calculated for them. Each term and the overall model are intended to be significant when they result in p-values which are small and generally lower than 0.05 because the null hypothesis of no factor or interaction effect is false in this case; additionally, the adjusted R-squared is expected to be close to 1, being it a measure of the model capability in accounting the variation of the dependent variable [73].

## 5.5 DESIRABILITY

Once a study has been done to model the response variables, the optimum combination of the input factors is addressed to produce a desired output, within the processing domain. Irrespective of the subject being investigated, either the minimum or the maximum of a certain function is required in the optimization, with possible additional constraints depending on specific needs.

Many procedures are feasible to solve constrained non linear optimization problems, such as successive linear programming, successive quadratic programming, penalty and barrier function methods, augmented Lagrangian factors [79]. The desirability function method is widely used in industry for the numerical optimization of multiple response processes and has been considered for welding too [13, 80]. It is usually recommended being it simple and normally available in software; flexibility is also benefited in giving importance for individual responses, according to customer needs [13].

The basic idea is that a product or a process with multiple quality features, is completely unacceptable if even just one of them drops outside its desired limits. Referring to welding, usual constraints involve the fused zone, the bead width and the amount of indications to be minimized; the tensile strength to be maximized; additional goals are generally set for specific shape-factors, depending on the material being welded. In practice, each estimate response $Y_i$ is turned into a dimensionless utility $d_i$ ranging from 0 to 1, namely from a completely undesirable output to the highest or ideal response. Moreover, being $w_i$ the awarded weight ranging from 0.1 to 10, the shape of the desirability function is adjusted and, depending on the specific goal, is given as following. For the goal of maximum:

$$d_i = \begin{cases} 0 & Y_i \leq \text{Low}_i \\ \left(\dfrac{Y_i - \text{Low}_i}{\text{High}_i - \text{Low}_i}\right)^{w_i} & \text{Low}_i < Y_i < \text{High}_i \\ 1 & Y_i \geq \text{High}_i \end{cases} \tag{5.3}$$

Similarly, for the goal of minimum:

$$d_i = \begin{cases} 1 & Y_i \leq \text{Low}_i \\ \left(\dfrac{\text{High}_i - Y_i}{\text{High}_i - \text{Low}_i}\right)^{w_i} & \text{Low}_i < Y_i < \text{High}_i \\ 0 & Y_i \geq \text{High}_i \end{cases} \tag{5.4}$$

For $T_i$ as a target:

$$d_i = \begin{cases} \left(\dfrac{Y_i - \text{Low}_i}{\text{T}_i - \text{Low}_i}\right)^{w_{1i}} & \text{Low}_i < Y_i < T_i \\ \left(\dfrac{\text{Y}_i - \text{High}_i}{\text{T}_i - \text{High}_i}\right)^{w_{2i}} & T_i < Y_i < \text{High}_i \\ 0 & \text{otherwise} \end{cases} \tag{5.5}$$

Emphasis on the upper bound, the lower one or the target is given by the weight field. In particular, as shown in **figure 5.4**, when a higher weight is awarded to the function of maximum, a significant increase of the response is required towards its highest possible value so to achieve a considerable increase of desirability. Conversely, when a higher weight is awarded to the function of minimum, a significant decrease of the response is required towards its lowest value so to achieve a considerable increase of desirability.

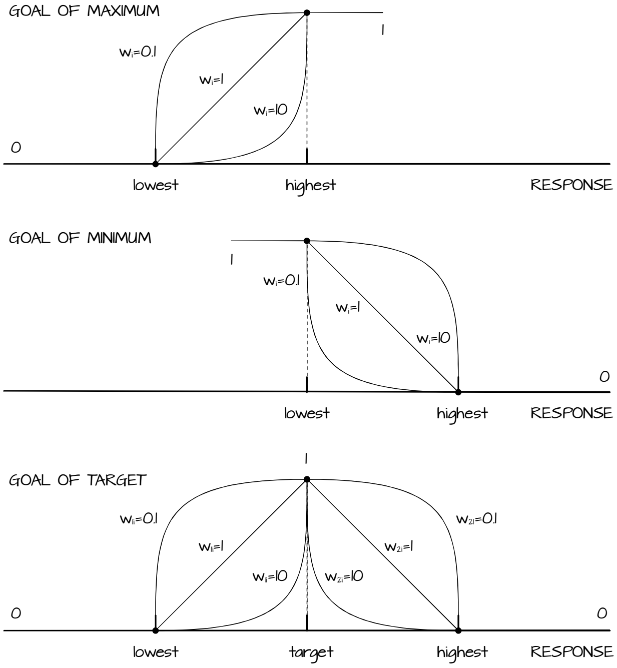

**FIGURE 5.4 –** Desirability as a function of the response, for given goals and weights

The corresponding curves for the goal of target are hence conveniently altered by the proper weight such that the highest desirability is achieved as the response approaches the target. For no specific goal, with the only constraint of the response to be within a range, the following condition applies:

$$d_i = \begin{cases} 1 & \text{Low}_i < Y_i < \text{High}_i \\ 0 & \text{otherwise} \end{cases} \tag{5.6}$$

Goals are combined via geometric mean into an overall desirability function $D$ which is a dimensionless measure of performance:

$$D = [d_1(Y_1) \cdot d_2(Y_2) \cdot \cdots \cdot d_h(Y_h)]^{\frac{1}{h}} \tag{5.7}$$

with $h$ denoting the number of total responses to be examined. As for any single desired output $d_i$ the overall desirability function ranges between 0 and 1, from a completely undesirable value to an ideal overall response. If many outputs are measured, the mission to get them all within specification becomes impossible [81]; then, only vital few responses are considered.

Alternatively, each response can be awarded a relative importance $m$ such that the overall desirability function becomes:

$$D = [d_1{}^{m_1}(Y_1) \cdot d_2{}^{m_2}(Y_2) \cdot \cdots \cdot d_h{}^{m_h}(Y_h)]^{\frac{1}{\sum m_i}} \tag{5.8}$$

If all of the responses are awarded the same importance $M$, hence the form (5.7) is brought back:

$$D = \left[d_1{}^{M}(Y_1) \cdot \cdots \cdot d_h{}^{M}(Y_h)\right]^{\frac{1}{h \cdot M}} = [d_1(Y_1) \cdot \cdots \cdot d_h(Y_h)]^{\frac{1}{h}} \tag{5.9}$$

When approaching the problem of numerical optimization with automatic procedures, several processing conditions are suggested with their corresponding desirability. The combination providing the highest overall desirability is generally considered for further investigation. In particular, the process is performed according to the recommended set-up, and a reasonable good agreement with the predicted desired output is expected for the response variables.

# 6

# WELDING ALUMINUM ALLOY 2024

## 6.1 INTRODUCTION

Weight reduction is one of the most effective ways to enhance efficiency and improve fuel mileage in vehicles and aircraft [82]. Therefore, aluminum alloys are widely used both in the automotive, military, aeronautic and aerospace industries [45] thanks to their electrical conductivity and excellent resistance to corrosion, although the tensile strength, the Young modulus and the hardness are much lower compared with steel.

Aluminum alloys are divided into two major categories: wrought compositions and cast compositions. Different nomenclatures have been developed [83], the Aluminum Association system being the most widely recognized. In particular, nine alloy groups are defined for each category; special interest has been shown in aerospace for wrought compositions alloys of the 2xxx family. Furthermore, among all of the commercial high strength heat-treatable and age-hardenable aluminum alloys, whose mechanical properties can be improved by a controlled cycle of heating and cooling, AA 2024 is widely common; its nominal chemical composition [83] is given in **table 6.1**.

Indeed, as for any other heat-treatable alloy, high strength is produced by finely dispersed precipitates which result from aging, since alloying elements, which decrease in solubility with decreasing temperature, are added in a proper concentration exceeding their equilibrium solid solubility at room temperature. Copper is generally added to increase strength following solution heat treatment and quenching; as little as approximately 0.5% magnesium is effective in changing aging characteristics [83].

**TABLE 6.1** – AA 2024 nominal chemical composition (wt.%)

| Cu | Mg | Mn | Si | Fe | Zn | Ti | Cr | Al |
|---|---|---|---|---|---|---|---|---|
| 3.80 ÷ 4.90 | 1.20 ÷ 1.80 | 0.30 ÷ 0.90 | 0.50 | 0.50 | 0.25 | 0.15 | 0.10 | Balanced |

## 6.2 ALUMINUM WELDING

A number of methods are capable of joining aluminum and its alloys: in particular, gas arc welding, resistance welding, friction welding, stud welding, electron and laser beams are employed. Unfortunately, irrespective of the technology being used, several challenges are involved due to possible cracking, porosity susceptibility and softening in the fused zone [83, 84, 85]. In particular, a large HAZ is produced in gas welding and significant hot cracking is observed [86]. On the other hand, although the metal is not melted in friction stir welding, thus resulting in less micro structural changes with additional partial recovery in strength due to the high shear stresses which are induced by tool motion, a counterproductive reduction in corrosion resistance is noticed [87], slower welding rates apply and several challenges arise in tool design when joining thin sheets [88].

Laser welding of aluminum alloys is worth investigating to benefit from a wide range of advantages, although additional specific issues arise as a consequence of high thermal conductivity and low absorptance [89]. Methods such as high frequency beam oscillation [90] and laser-arc hybrid welding [91] have been suggested indeed to improve laser weldability of aluminum alloys.

## 6.3 EXPERIMENTAL PROCEDURE

Referring to literature or ad hoc explorative trials, proper welding conditions were set for BOP or butt welded specimens in order to discuss specific issues in laser welding of AA 2024. As preventive measure to remove residual moisture on the surfaces to be welded, pickling was carried out for 3 min at room temperature with 2% hydrofluoric and 15% nitric acid in distilled water mixture [83]; further degreasing with acetone was performed just before welding. Given the need to minimize any gap between the plates in square butt joining (cf. par. 4.2), a system-integrated camera is employed when setting the welding path; an excellent pose and a repeatability robot accuracy of 0.03 mm can additionally save the alignment during the process.

**TABLE 6.2** – Mechanical preparation: details for grinding and polishing AA 2024

| Runs | Grinding/polishing medium | Wheel speed [rpm] | Processing time [min] |
|---|---|---|---|
| 2 | P400 paper | 100 | 1 |
| 2 | P800 paper | 100 | 1 |
| 2 | P1200 paper | 100 | 1 |
| 1 | 6 µm diamond suspension | 50 | 2 |
| 1 | 3 µm diamond suspension | 50 | 2 |
| 1 | 1 µm diamond suspension | 50 | 2 |

A check of the focus position was preliminary performed (cf. par. 3.5). Welding points were spotted using a single rectangular pulse input with a peak power of 1.8 kW for 50 ms to tighten the abutting plates. Beads in continuous wave emission mode were then produced using a Trumpf Tru-Disk 2002 with a BEO D70 focusing optics (cf. **table 2.2**).

The samples were mounted in phenols and polished. The steps for mechanical preparation, with a constant load of 10 daN between the rotating plate and the sample holder in both automatic grinding and polishing, are given in **table 6.2**; when needed for special purpose of porosity observation, simple manual grinding with P800 SiC paper was performed on longitudinal sections. Chemical etching was performed at room temperature for 10 s using Keller's solution consisting in 1% hydrofluoric, 4% hydrochloric and 3% nitric acid in distilled water [83]. Imperfections were measured via Nikon NIS-Elements imaging software. A LEO EVO 50, with LaB6 gun SEM and a resolution of 4 nm at 30 keV, equipped with an EDS Oxford INCA Energy 300 was used to check the resulting composition of the bead; the system is capable of providing information starting from elements with atomic number which are higher than 4; the analysis was performed with a 20 keV primary energy and a 100 pA probe current. Eventual bead characterization was conducted with a Leica VM HT Auto for Vickers micro hardness testing, a General Electric CRx Flex CR Scanner for X-rays examination and an MTS Insight 30 for tensile testing.

## 6.4 SYSTEM SET-UP

Specific tests were conducted to discuss the main issues in laser welding of AA 2024. Special care must be taken for gas flow as boundary condition at the key-hole input, since it may significantly affect the dynamics of the process [2, 40].

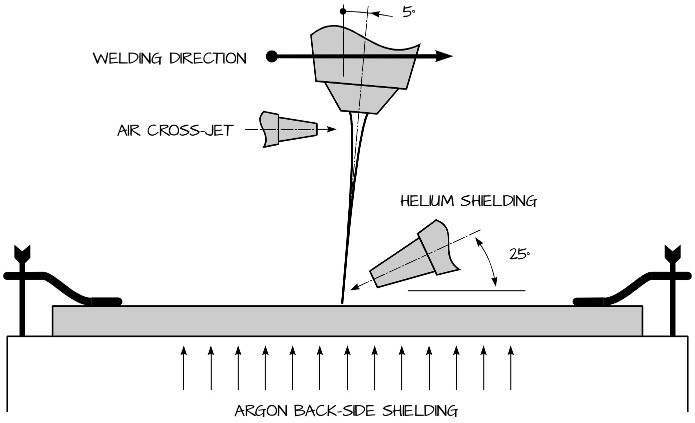

**FIGURE 6.1** – Laser welding set-up: suggested scheme for aluminum processing

Many studies have dealt with plume generation and overall stability in welding aluminum alloys indeed, depending on physical properties of the shielding gas and nozzle geometries [92, 93, 94]. As a carryover from usual practice of welding steel, copper nozzles are employed for plasma suppression [45] and have been proven to be effective also in bead shielding from oxidation, so no additional diffusers are needed. Convincing results were achieved when welding AA 2024 using a 25° tilted trailing nozzle [95].

As expected (cf. par. 3.4), argon upper supply was proven to end up in less absorptance due to plasma interaction, whilst better results were achieved using helium, having it a higher ionization potential so allowing a better coupling of the beam with the metal surface; in addition, finer spatter droplets were produced compared with argon [92]. A flow rate of 30 l/min was chosen for helium supply. Nevertheless, when needed, argon provides good back-side shielding, since no interaction is in place between the laser and the gas flow. As normal welding procedure, proper time delays are set both before and after welding, to effectively prepare an inert atmosphere and to better shield the bead crown when switching off the laser beam; furthermore, a high speed compressed air cross-jet is blown to protect the optics from spatters. The scheme for the suggested set-up is shown in **figure 6.1**, the beam angle applying as common practice for highly reflective materials (cf. par. 3.6); in particular, referring to preliminary trials, a forward tilting inclination, which is intended to focus the beam into the weld pool, has proven to be beneficial in terms of spatters, compared with positive backward angles.

## 6.5 GENERAL ISSUES IN LASER-MATERIAL INTERACTION

One of the main reasons of incomplete fusion of the base material and consequent defects in the welding bead, is the possible presence of natural oxide on the metal to be joined. Aluminum has a strong chemical affinity for oxygen indeed, therefore it oxidizes immediately upon exposure to air: aluminum oxide melts at approximately 2050 °C, whereas the melting point of the base alloy is 600° C, so any oxide on the base metal must be properly removed [83, 92]. This would also prevent from oxidic inclusions in the weld metal [96]. Stainless steel brushes are preferred to avoid rust contamination of the joint; moreover, when a power brush is used, then a light pressure should be applied because high forces can result in embedding the oxide or possible contaminants into the surface, thus increasing, rather than eliminating, the risk of discontinuities in the weld [83].

Once the task has been accomplished, specific additional issues must be taken into account when welding aluminum alloys with laser beams, basically as a consequence of high thermal conductivity and low absorptance. Although the melting temperature of aluminum is much lower compared with any ferrous alloy, irrespective of the alloying elements, higher irradiance is required to effectively melt the base metal due to its high reflectivity, which ranges between 0.86 and 0.90 for pure aluminum at laser wavelength between 0.9 and 1.0 µm [97]; the reflectivity of aluminum as a function of the operation wavelength [5] is shown in **figure 6.2**, in comparison with corresponding trend

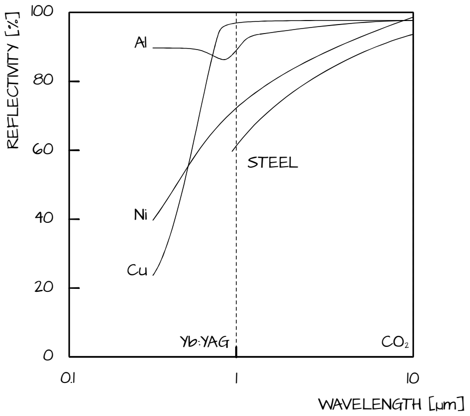

**FIGURE 6.2** – Reflectivity of metals as a function of operation wavelength

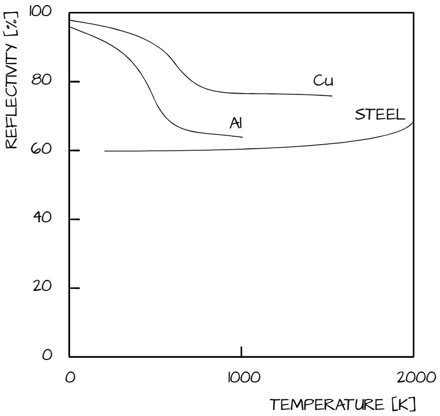

**FIGURE 6.3** – Reflectivity of metals as a function of temperature, for YAG radiation

of common metals. In general, the beam energy which is absorbed by a specific material increases with decreasing operation wavelength [10]; therefore, YAG lasers provide better coupling than $CO_2$ sources. However, the purer is the aluminum alloy, the higher is its reflectivity [98].

Absorptance can be enhanced in a variety of methods [2] such as the application of absorbent powders [10]; in particular, the reflectivity is a function of the thermal state of the material and, as shown in **figure 6.3** for YAG radiation, it decreases as temperature increases [5].

The result of a BOP test on a 3.2 mm thick plate is shown in **figure 6.4**: with a power of 1.2 kW and a welding speed of 6 mm/s in focused condition, fusion was not produced at the beginning of the welding path, whilst a key-hole mode welding condition started once the reflectivity had decreased during the process as a consequence of heating up. In order to allow the key-hole to develop since the start of the welding path, a threshold value of 18.4 kW/mm$^2$ irradiance has to be overcome [3].

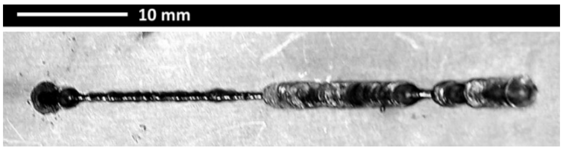

**FIGURE 6.4** – BOP test sample: no key-hole development below the threshold irradiance

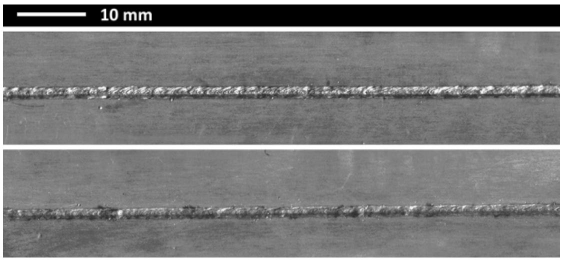

**FIGURE 6.5 –** Butt welding samples: top- and back-side bead aspect

Reflectivity is an issue which demands specific changes in the normal processing set-up anyway. Therefore, in order to prevent the focusing optics from damages due to back reflection as a consequence of low absorptance, a sideways tilting angle, in the order of degrees, is generally used to position the laser head [5]. The pre welding entry spot, which is provided at the beginning of the welding path to better tighten the samples, was proven to also act in locally reducing the reflectivity so that deep penetration is enhanced [95]; therefore, it is suggested to be performed in lap joints and BOP also, where no actual tightening is needed. Cleaning the lenses is convenient anyway to prevent reduction of the input radiation due to dust or metal drops resulting from previous processes [88].

In addition to low absorptance, energy transfer from the beam to the metal is further worsen since thermal conductivity is 120 W/mK for AA 2024, so approximately six times higher compared with steel. Irrespective of the heat source for welding, aluminum is hence very sensitive to any heat input fluctuation during the process, whilst a steady input is required to prevent variation in penetration and fusion [83]. However, when using a laser beam, higher welding speeds are possible compared with traditional methods, therefore the total processing time is shortened and both the bead crown and root are found to be constant along the welding line. As an example, top- and back-side aspects of AA 2024 beads are shown in **figure 6.5**, for 1.25 mm thick samples, 1.6 kW power level, 60 mm/s welding speed in focused condition.

## 6.6 POROSITY EVOLUTION

Many issues with aluminium welds arise due to an unfavourable distribution of pores [99], whose type depends on the process being performed.

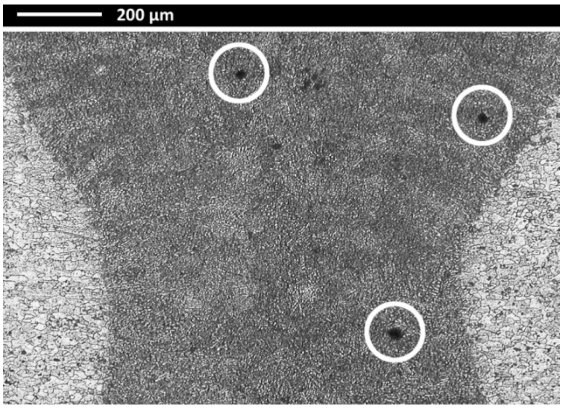

**FIGURE 6.6 –** Micro pores in the cross-section of a butt welded aluminium sample

In particular, it has been pointed out that two types of pores arise. Micro pores of spherical shape, whose mean diameter ranges between 50 and 200 µm [100], do not normally result in the rejection of welded parts at quality checks [101]: they are ascribed to hydrogen and other common gases which are released and trapped in the solidifying alloy as their solubility in liquid metal is much higher compared with that one in solid state [49, 101]. As an example, a cross-section with micro pores, as resulting from butt welding a 1.25 mm thick sample using a power of 1.6 kW and a welding rate of 80 mm/s in focused condition [80] is shown in **figure 6.6**. High temperatures which are experienced in the weld pool allow a large amount of hydrogen to be absorbed; as the weld

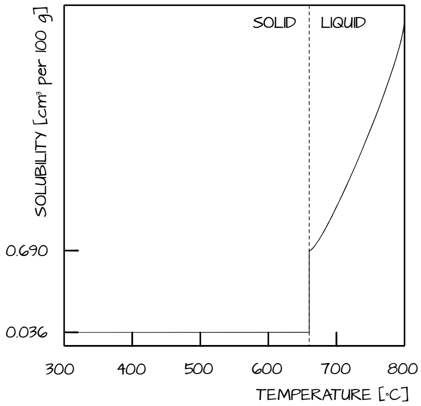

**FIGURE 6.7 –** Hydrogen solubility in aluminium as a function of temperature

pool solidifies, the solubility of hydrogen greatly decreases as shown in **figure 6.7** for pure aluminum. This difference in solubility is the driving force for porosity formation because the percentages of hydrogen exceeding the effective solubility limit end up in forming gas pores, if not escaping the solidifying weld [83]. For such reasons, gas mixture with even minimum hydrogen content are excluded from shielding [18]; moreover, preventive measures must be taken to carefully remove from the base metal any source of hydrogen or foreign material, such as milling and machining lubricant which could produce inclusions in the bead [83]. Since an adequate seam preparation is deemed to be vital for sound beads, cleaning of both sides of the joint when preparing surfaces for deep penetrative welding is recommended. Pickling, solvent degreasing or slight pre heating are usually carried out indeed. However, the welding position may either help or hinder the expulsion of gas bubbles: in general, vertical-up welding of aluminum produces the least amount of pores as the solidifying weld pool provides an easy escape for gases; conversely, overhead welding results in the greatest amount due to the floating direction and the convection patterns [83].

Macro pores, instead, which are also referred to as macro cavities, ranging in size between 300 and 600 μm [100], are usually visible to the unaided eye, seriously affect the mechanical properties of the bead and are therefore the main ones to be investigated. They are less circular than hydrogen-occluded pores and locate along the welding bead centre-line [49, 3]. Imperfect collapses of the key-hole during welding, as a consequence of large differences in boiling and melting points of the base metal and the main alloying elements is addressed. In particular, gas occlusions and non stable key-holes are favoured by a high magnesium content [100] which is expected to also influence welding of 2xxx family alloys, although being lower compared with 5xxx family: it is inferred that a change is produced in the key-hole pressure balance equation because vaporization is a non equilibrium process.

The loss in magnesium content, and therefore the final amount of pores, depends on the processing parameters and is clearly noticed via EDS in the transverse bead cross-section. An average loss of magnesium in the order of 53% was estimated when BOP welding 3.2 mm thick plates with a power of 1.6 kW, a welding speed of 10 mm/s with 0.5 negative defocusing [4]. In order to better discuss the issue, a cross-section with pores was considered and appropriate sites of interest were scanned.

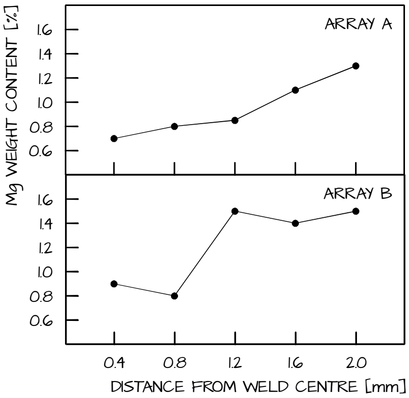

**FIGURE 6.8** – Magnesium content as a function of distance from weld centre; 3.2 mm thick plate

The magnesium content as a function of the distance from the welding axis of the bead is shown in **figure 6.8**: it drops when moving from the base metal, where a nominal reference value of 1.56% is detected on average, towards the fused zone. Specific steepness depends on the scanning array positioning across the bead border line: in particular, array A and B approximately locate at 0.5 and 1 mm depth with respect to the top surface, as shown in **figure 6.9**.

Notably, the local magnesium concentration for sites in the bulk of the weld metal is uniform, thus confirming that vigorous convective mixing actually occurs in the molten metal [5] as the key-hole develops.

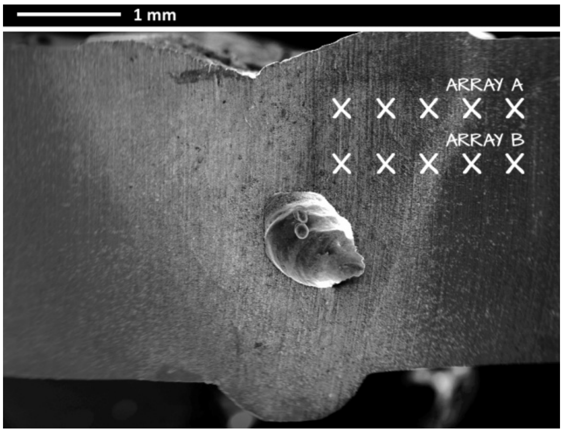

**FIGURE 6.9** – EDS scanning strategy for magnesium content inspection; 3.2 mm thick plate

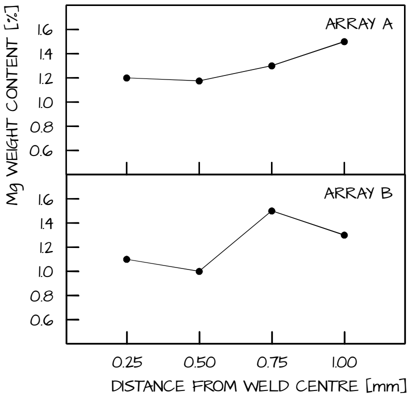

**FIGURE 6.10** – Magnesium content as a function of distance from weld centre; 1.25 mm thick sheet

Higher welding speeds and lower thermal inputs are required to match the quality requirements when welding 1.25 mm thick sheets of the same alloy. The magnesium content as detected via EDS analysis is shown in **figure 6.10** for a butt welded joint with a power of 1.6 kW, a welding speed of 80 mm/s in focused condition [80]; array A and B in this case approximately locate at 0.3 and 0.6 mm depth with respect to the top surface, as shown in **figure 6.11**.

A 1.16% residual magnesium content is measured in the bulk. Vaporization of the alloying elements is lower due to shorter interaction time between laser and material; no macro pores are found in random cross-sections.

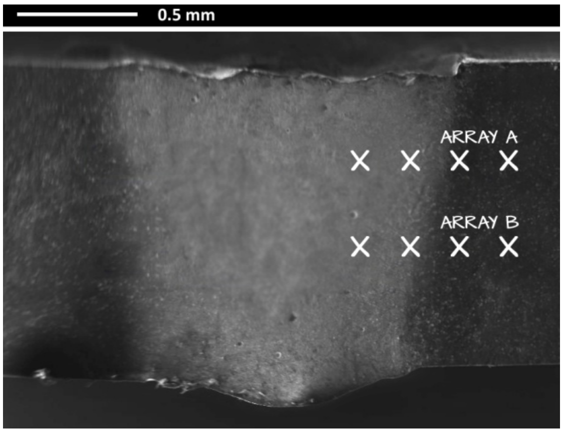

**FIGURE 6.11** – EDS scanning strategy for magnesium content inspection; 1.25 mm thick sheet

Since the bead width is significantly narrow, the mean crown being 1.5 mm wide, a proper longitudinal cut is not feasible for a reliable observation of macro pores; nevertheless, larger beads on thicker plates showed that any significant content of pores is statistically detected even in the cross-sections [95]; therefore, one could assume the examined welding set actually allows the process to be performed in much more stable conditions.

### 6.6.1 THERMAL INPUT DEPENDENCE

A significant influence on macro porosity is ascribed to the thermal input. Longitudinal sections of two 3.2 mm thick specimens which were processed with 160 and 200 J/mm thermal input [3] are shown in **figure 6.12**. A 6 mm (i.e. 0.25 in) long zone both at the beginning and at the end of the welding bead was excluded from measurements in order to neglect any transitory effect due to key-hole opening and closure. Provided that fully penetrative conditions are accomplished, lower thermal inputs result in increasing porosity: the mean amount is close to the limit of 5% with respect of the total fused zone, which is the allowed limit according to international specifications [66], so welding is performed in critical conditions which would easily end up in bead rejection at quality checks. It is well known that the melted material flow in the weld pool heads towards the root [5] thus resulting in bubble ejection in fully penetrative welds. The process is enhanced when higher thermal inputs are provided [3]. Conversely, it is inferred that a higher thermal input in incomplete penetrative welds do only increase the loss of volatile elements such as magnesium which has been proven to favour the key-hole instability thus leading to porosity [2].

An amount of 15% porosity was observed with a much lower thermal input of 80 J/mm [95]. Results with a 240 J/mm thermal input were also investigated;

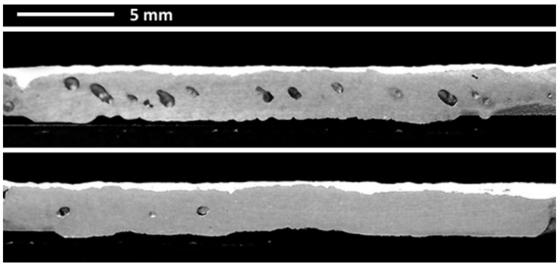

**FIGURE 6.12 –** Macro pores in longitudinal sections: 160 and 200 J/mm thermal input

nevertheless, given the maximum output power level for the welding system in place, this requires very low welding speeds resulting in non uniform beads, to be excluded from the analysis [3].

### 6.6.2 DEFOCUSING EFFECT

As for any metal alloy, a defocused laser beam is thought to improve the weld quality in aluminum joints in term of porosity and enhanced penetration depth [49]. The effects of different focal positions were studied on 3.2 mm thick plates in butt configuration.

Once the 18.4 kW/mm$^2$ threshold value is provided with constant power of 1.8 kW and welding speed of 10 mm/s, a key-hole mode develops with 1 mm negative defocusing; conversely, a 1 mm positive defocusing only melts the surface and no key-hole mode develops. As expected, the welding outcome is different although the same defocusing shift applies and although the beam divergence is considered to be low for the system in place. The porosity trend as a function of the focus position is shown in **figure 6.13**; a power of 1.8 kW and a welding speed of 10 mm/s are taken as constant; a maximum standard deviation of 1.5 was measured for porosity. Notably, when positively defocusing to 0.5 mm, the resulting porosity is due to incomplete penetration, since bubble ejection is hindered as convective patterns in the weld pool do not reach the back-side surface; therefore, gas driven towards the tip are trapped after solidification [2]. On the other hand, a reduction is achieved with 0.5 mm negative defocusing, compared with focused conditions. Nevertheless, when further negatively defocusing to 1 mm, pressure terms in the balance are affected in such a measure that the stable solution for the equilibrium radius of the key-hole is significantly moved. To support the assumption, the cross-section which have been produced with a 10 mm step are shown in **figure 6.14**

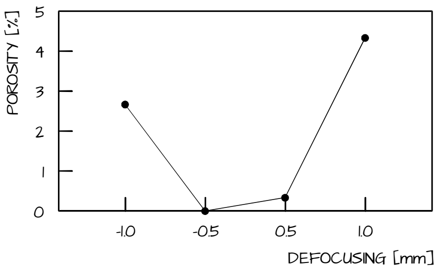

**FIGURE 6.13** – Porosity trend in bead longitudinal section as a function of the focus position

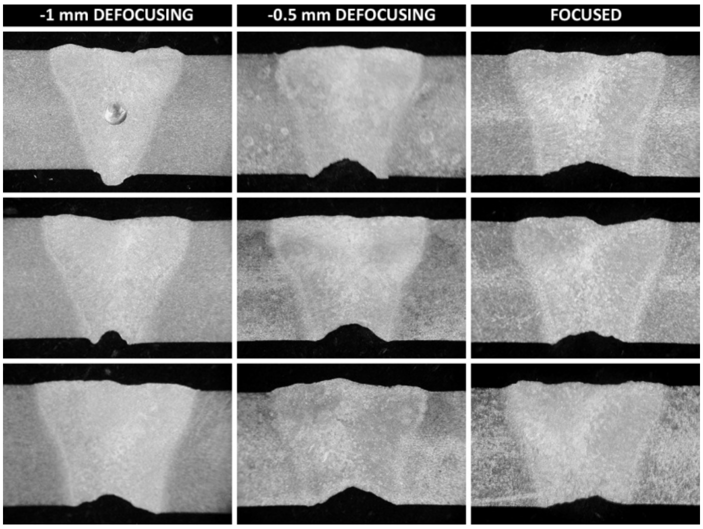

**FIGURE 6.14 –** Bead profiles, with 10 mm step along the welding direction, for different focusing

in different focusing conditions: the bead profile is clearly irregular along the welding direction when negatively defocusing to 1 mm, and pores are clearly noticed in the cross-section. This is enough to assess that AA 2024 is highly susceptible to minimal deviation of the focus position.

### 6.7 SOFTENING IN THE FUSED ZONE

Since the mechanical properties in aluminum alloys do not only depend on the alloying elements, but on the heat treatment also, it is worth noting that AA 2024 in T3 state was considered, the designation applying to cold worked products whose strength is improved after solution treatment and eventual room temperature aging for stabilization [83].

Referring to **figure 6.15**, the dark particles at grain boundaries in the base material are $Cu_2Mn_3Al_{20}$, $CuMgAl_2$ and $Cu_2FeAl_7$ precipitates [83] resulting from preliminary solution heat treatment and artificial aging, whilst columnar growth of the grains in the direction of the thermal gradient is experienced in the fused zone [95]. Changes also take place in the HAZ, although fusion did not occur. Indeed, when considering any heat treatable alloy, as AA 2024 is, dissolution or growth of strengthening precipitates result, depending on the aluminum family [84]: this leads to worsening of the weld properties anyway.

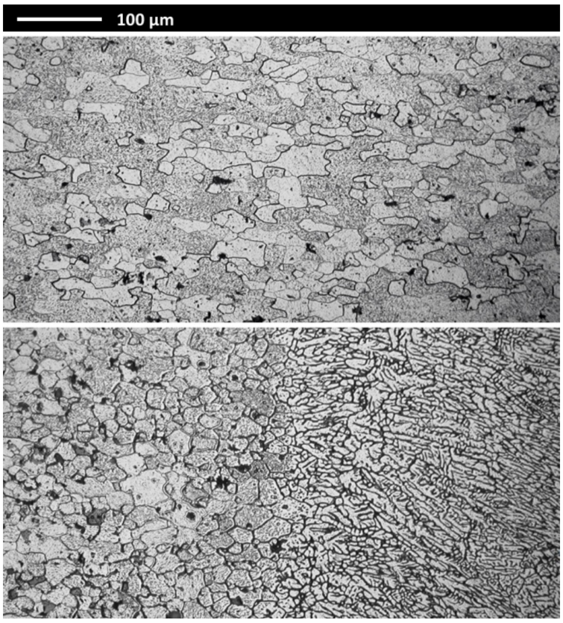

**FIGURE 6.15 –** AA 2024 T3, micrograph: base metal (above) and HAZ at the bead interface (below)

Namely, the response in the HAZ for 2xxx family follows dissolution, whereas the primary modification for 6xxx family is growth of the precipitates, although a slight increase in hardness typically occurs near the fusion zone. The global effect is commonly referred to as HAZ and fused zone degradation. It has been suggested that friction stir welded joints of the 2xxx family could be significantly improved in tensile strength by post weld heat treatments [102] which are therefore assumed to be a valid recovery method for laser welding also. However, softening can be controlled below a significant extent by using a low heat input process: in this view, laser welding is deemed to be a favourable joining technology for 2xxx family aluminum alloys [85].

Vickers micro hardness tests were carried out to highlight the effects of laser thermal cycles in softening the welding zone. Indentations were made at mid thickness [65], with a load of 0.98 N (i.e. 0.1 kgf), for a dwell period of 15 s with a speed of 60 µm/s [67]; tests were performed one week after welding to allow the stabilization of the properties after natural aging [83]. As an example, the micro hardness trend as a function of the distance from the weld centre is shown in **figure 6.16** for a 1.25 mm thick butt welded specimen obtained with a power of 1.4 kW, a welding speed of 80 mm/s and 0.5 positive defocusing.

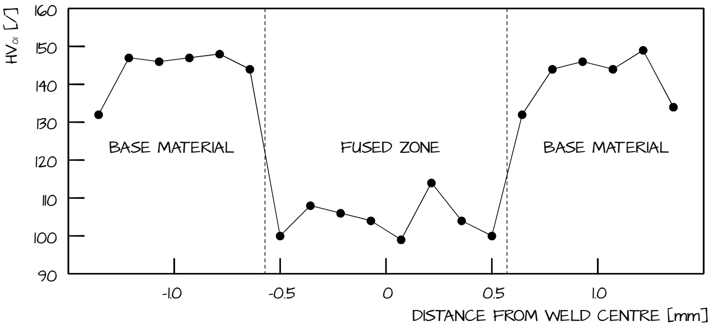

**FIGURE 6.16** – Vickers micro hardness in the cross-section as a function of distance from weld centre

As expected, a decrease in micro hardness is noticed from 145 $HV_{0.1}$ in the base metal to an average 105 in the fused zone. When temperatures in the HAZ exceed the solvus curves, respective phases are dissolved; at a position which is close to the fusion zone, where higher temperatures are experienced, substantial dissolution of the strengthening phases is therefore supposed to have place [83]. Nevertheless, transition values were not observed between the base metal and the fused zone, such that it is not possible to clearly assess the extent of the HAZ, which is hence assumed to be less wide than the distance between two consecutive indentations, that is to say 150 µm according to the referred specification.

Interestingly, when welding 3.2 mm thick samples with higher thermal inputs, no differences in micro hardness values were found, thus suggesting that any drop in the properties is basically the result of a threshold point for precipitates dissolution being overcome, irrespective of the welding parameters. Anyway, a longer interaction between the metal and the heat source affects the HAZ which, for example, ranged from 200 to 250 µm when welding was performed with a power of 1.6 kW, a speed of 10 mm/s in focused conditions [95].

### 6.8 OPTIMIZATION OF BUTT WELDED JOINTS

Satisfactory results in welding AA 2024 thin sheets under 2 mm in thickness had been achieved using Nd:YAG and $CO_2$ laser sources [103]. A 3-level experimental plan with governing factors power $P$, welding speed $s$ and focus position $f$ was arranged in order to find an optimal processing combination of parameters to weld 1.25 mm thick sheets via Yb:YAG disk-laser [80].

**TABLE 6.3** – DOE: factor levels for AA 2024 butt welding

| | **-1** | **0** | **+1** |
|---|---|---|---|
| **P [W]** | 1400 | 1600 | 1800 |
| **s [mm $s^{-1}$]** | 50 | 65 | 80 |
| **f [mm]** | -0.5 | 0 | 0.5 |

The factor levels of the experimental plan are given in **table 6.3**; the beam geometry and the specific irradiance threshold to be overcome were taken into account to choose the ranges. Referring to a face-centred CCD, the welding conditions to be tested are listed in **table 6.4**.

As suggested in specific guidance for electron and laser beam welding of aluminium [66], three types of common imperfections were found to need special considerations: excessive penetration $EP$, sagging $S$ and misalignment $M$ (cf. **figure 4.4**); imperfections such as undercuts or shrinkage grooves were occasionally produced. Crown width $CW$ on the upper surface, root width $RW$ on the back-side and the extent of the fused zone $FZ$ (cf. **figure 4.3**) were considered to describe the bead profile. Mean values are listed in **table 6.5**, although the checks were separately referred to each single measurement, so to prevent possible misleading compensation in the arithmetic mean.

**TABLE 6.4** – DOE: Welding conditions to be tested in a face-centred CCD scheme

| **Condition** | **P [W]** | **s [mm $s^{-1}$]** | **f [mm]** |
|---|---|---|---|
| **1** | 1400 | 50 | -0.5 |
| **2** | 1800 | 50 | -0.5 |
| **3** | 1400 | 80 | -0.5 |
| **4** | 1800 | 80 | -0.5 |
| **5** | 1400 | 50 | 0.5 |
| **6** | 1800 | 50 | 0.5 |
| **7** | 1400 | 80 | 0.5 |
| **8** | 1800 | 80 | 0.5 |
| **9** | 1600 | 65 | 0 |
| **10** | 1600 | 65 | 0.5 |
| **11** | 1600 | 65 | -0.5 |
| **12** | 1600 | 80 | 0 |
| **13** | 1600 | 50 | 0 |
| **14** | 1800 | 65 | 0 |
| **15** | 1400 | 65 | 0 |

**Table 6.5 –** DOE: response variables, mean values for each testing condition

| Condition | EP [mm] | S [mm] | M [mm] | CW [mm] | RW [mm] | FZ [mm$^2$] |
|---|---|---|---|---|---|---|
| **1** | 0.10 | 0.07 | 0.06 | 1.80 | 1.36 | 1.93 |
| **2** | 0.04 | 0.06 | 0.06 | 1.53 | 1.03 | 1.54 |
| **3** | 0.07 |  | 0.02 | 1.37 | 0.84 | 1.33 |
| **4** | 0.13 | 0.08 | 0.01 | 1.40 | 1.15 | 1.49 |
| **5** | 0.10 | 0.10 | 0.02 | 2.03 | 1.41 | 2.24 |
| **6** | 0.14 | 0.18 | 0.01 | 1.84 | 2.04 | 2.38 |
| **7** | 0.01 | 0.04 | 0.02 | 1.51 | 0.90 | 1.40 |
| **8** | 0.16 | 0.11 | 0.01 | 1.57 | 1.26 | 1.67 |
| **9** | 0.11 | 0.09 | 0.02 | 1.59 | 1.34 | 1.71 |
| **10** | 0.11 | 0.10 | 0.04 | 1.76 | 1.37 | 1.87 |
| **11** | 0.09 | 0.06 | 0.02 | 1.54 | 1.30 | 1.62 |
| **12** | 0.14 | 0.01 | 0.03 | 1.50 | 1.14 | 1.57 |
| **13** | 0.17 | 0.22 | 0.01 | 1.78 | 1.63 | 2.00 |
| **14** | 0.10 | 0.18 | 0.01 | 1.51 | 1.40 | 1.65 |
| **15** | 0.13 | 0.09 | 0.02 | 1.57 | 1.31 | 1.66 |

With respect to the thickness being investigated, the stringent quality category, which is the best one possible according to the referred specification, is met for $EP$ and $M$ being their values lower than 0.39 and 0.13 mm, respectively, although one should assume anyway misalignment being affected by improper clamping of the plates rather than by the specific processing condition. Reference quality levels for $S$ are not general instead, being them related to $EP$, as a trade-off between sagging and excessive penetration is allowed in the specification, provided some conditions on sheet thickness $t$ and crown width are met. For stringent quality levels to be matched, the rule:

$$S \leq 0.1\, t + EP \tag{6.1}$$

apply for $CW$ below 0.625 mm, as it actually is in the experimental plan. The constraint is effectively met. When occasionally produced, undercuts and shrinkage grooves did match their corresponding quality requirement. Therefore, given their compliance with the standard, the processing conditions were considered to feed the optimization them all.

A shape-factor $SF$ for the bead cross-section was defined. Since no necking zones were found, the root to crown width ratio was considered, irrespective of the bead profile at mean height:

$$SF = \frac{RW}{CW} \tag{6.2}$$

Models for both the fused zone and the shape-factor were produced involving quadratic interactions among the governing factors; the corresponding p-values from the ANOVA were considered as indicators of significance: for the overall models, p-values of 0.0341 and below 0.0001 were achieved, respectively. As for example, the response surfaces for the fused zone for each level of the welding speed, as obtained via Design Expert software, are shown in **figure 6.17**. Interestingly, power has a quite moderate effect compared with speed and defocusing. A similar behaviour results for the shape-factor.

Specific criteria were then defined for the optimization. In principle, a goal of minimum is required for the extent of the fused zone, whose mechanical features are well known to be low compared with the base metal. Additional constraints involving the shape-factors are required: beads whose root width is close to the crown one must be rejected, being this condition indicative of welding occurring between conduction and key-hole regime, whilst a proper key-hole is preferred for the purpose of deep penetration and high aspect ratio; also, rejection is advised for beads whose root results in being too narrow, this shape hampering the expulsion of vapour and favouring porosity [95]. Hence, an optimal range between 0.5 and 0.7 was chosen for the shape-factor. The optimization procedure was then carried out. The first five solutions as suggested when considering the overall desirability functions are given in **table 6.6**. An optimal combination with a power of 1.4 kW power, a speed of 80 mm/s with 0.5 positive defocusing is suggested and is also considerably robust without significant variation both in the responses and the desirability output, even when affected by minor changes in defocusing. The condition was actually tested in the experimental plan as condition number 7 (cf. **table 6.4**). No macro pores were found via RT.

**TABLE 6.6 –** Optimization: suggested solutions with corresponding responses and desirability

| | P [W] | s [mm $s^{-1}$] | f [°] | RW/CW | FZ [$mm^2$] | Desirability |
|---|---|---|---|---|---|---|
| **1** | 1400 | 80 | 0.50 | 0.54 | 1.35 | 0.901 |
| **2** | 1400 | 80 | 0.49 | 0.55 | 1.35 | 0.900 |
| **3** | 1400 | 80 | 0.48 | 0.56 | 1.35 | 0.900 |
| **4** | 1400 | 80 | 0.45 | 0.57 | 1.35 | 0.899 |
| **5** | 1400 | 80 | 0.44 | 0.57 | 1.35 | 0.898 |

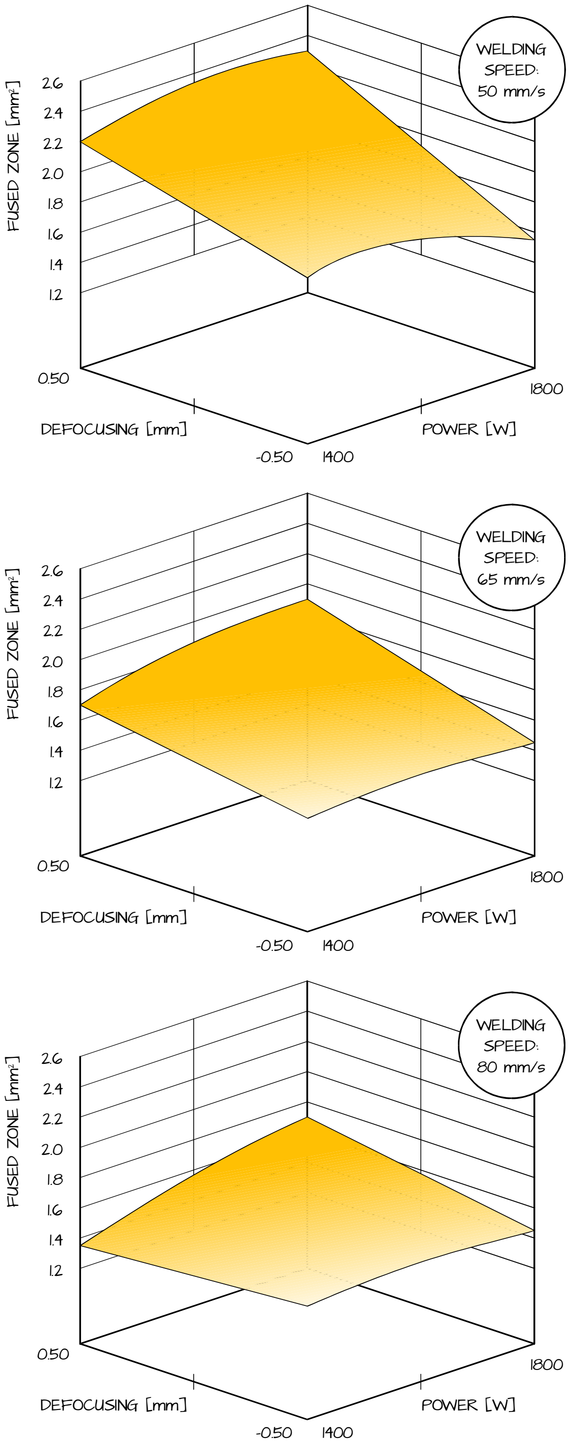

**FIGURE 6.17 –** Response surfaces for the extent of the fused zone for each level of welding speed

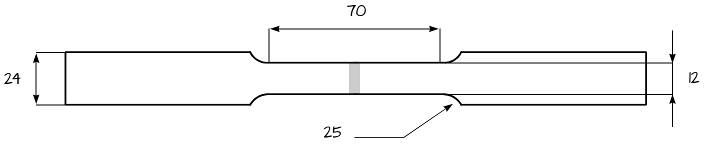

**FIGURE 6.18 –** Tensile specimen for aluminum square butt joint testing; dimensions in millimetres

The eventual assessment of the suggested condition was performed via tensile testing. In accordance with the referred specification [70], the dimensions of the tensile specimens are shown in **figure 6.18**; tests were performed at a crosshead speed of 0.015 mm/s.

As a consequence of degradation in the fused zone, although the failure mode depends on the alloy type as well as on its preliminary heat treatment and the welding condition, fracture is expected to have place in the bead. Nevertheless, it is widely accepted in several researches about different aluminum alloys [103, 104, 105] that any welding bead showing an UTS above 66% of the base alloy is acceptable. Values of percent elongation at break and UTS are given in **table 6.7**; the UTS is compared with original and non welded samples also, where 480 MPa are withstood, as expected according to material data sheet [83]. No plastic strain is experienced since a percent elongation at break of 18% would be normally expected from a non welded sample.

Fracture in each tested specimen started from the weld and grew towards the interface between the weld and the base material, where a steep discontinuity occurs in the mechanical features, as shown from the Vickers micro hardness trend; top- and back-side fracture surfaces are shown in **figure 6.19**. Interestingly, an average value of 77% the UTS of the base alloy resulted; an improvement was then benefited considered that lower values, below 69%, had been achieved with a Nd:YAG source on 0.8 mm thick sheet and a similar value was expected when alternatively considering a $CO_2$ source [103].

**TABLE 6.7 –** Tensile tests output for AA 2024 welded samples

| Test | UTS [MPa] | UTS/UTS$_0$ [%] | Elongation at break [%] |
|---|---|---|---|
| **1** | 385 | 80 | 1 |
| **2** | 369 | 77 | 1 |
| **3** | 357 | 74 | 1 |

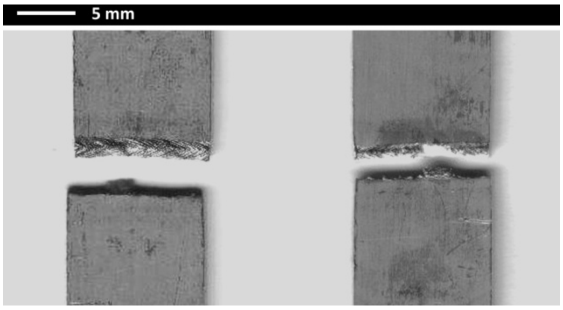

**FIGURE 6.19 –** AA 2024 butt welded sample: top- and back-side fracture surfaces

## 6.9 OPTIMIZATION OF LAP WELDED JOINTS

Being capable of joining materials by one-side access, laser welding is particularly useful for lap joining, since the beam is delivered on the top-laying sheet metal while the heat is being transferred, as the process goes on, to the under-laying plate. The process was investigated [88] with respect to 2024 aluminum alloy thin sheets as a promising alternative to friction stir welding [54]. A 4-factor study with power $P$, welding speed $s$, focus position $f$ and beam angle $\alpha$ was considered. Aiming to provide a general overview of the process to clarify the main effects and the interactions at a first stage of study, two levels for each factor were selected and a complete factorial plan was proposed: therefore, all of the possible combinations of factors and levels were tested, for a total of 16 configurations. Preliminary BOP trials suggested which level to be used for each factor.

Since deep penetration is achieved on 1.25 mm thick plates using a power of 1.8 kW to be coupled with a welding rate of 80 mm/s, and given the need to overlap two 1.25 mm thick plates, lower welding rate and/or higher power level must be chosen. With respect to the defocusing range, the beam

**TABLE 6.7 –** DOE: factor levels for AA 2024 lap welding

| | **-1** | **+1** |
|---|---|---|
| **P [W]** | 1800 | 2000 |
| **s [mm $s^{-1}$]** | 35 | 45 |
| **f [mm]** | -1.25 | 0 |
| **α [°]** | -15 | -5 |

**TABLE 6.8** – DOE: Welding conditions to be tested in a complete factorial plan

| Condition | P [W] | s [mm $s^{-1}$] | f [mm] | α [°] |
|---|---|---|---|---|
| **1** | 1800 | 35 | -1.25 | -15 |
| **2** | 1800 | 35 | -1.25 | -5 |
| **3** | 1800 | 35 | 0 | -15 |
| **4** | 1800 | 35 | 0 | -5 |
| **5** | 1800 | 45 | -1.25 | -15 |
| **6** | 1800 | 45 | -1.25 | -5 |
| **7** | 1800 | 45 | 0 | -15 |
| **8** | 1800 | 45 | 0 | -5 |
| **9** | 2000 | 35 | -1.25 | -15 |
| **10** | 2000 | 35 | -1.25 | -5 |
| **11** | 2000 | 35 | 0 | -15 |
| **12** | 2000 | 35 | 0 | -5 |
| **13** | 2000 | 45 | -1.25 | -15 |
| **14** | 2000 | 45 | -1.25 | -5 |
| **15** | 2000 | 45 | 0 | -15 |
| **16** | 2000 | 45 | 0 | -5 |

geometry must be considered for the irradiance threshold to be overcome. A base condition of focused beam and a negative 1.25 mm defocusing, with the focus hence ideally locating at the interface between the overlapping plates, were considered; sufficient irradiance is thus provided to melt the alloy. Forward beam angles with respect to the welding direction were used, being them beneficial to reduce the spattering. Hence, 5° and 15° negative beam angles were chosen. The levels for each factor are summed up in **table 6.7**; a complete view of the testing conditions is provided in **table 6.8**. Three replications were performed for each test, for a total of 48 runs; a random testing procedure was also arranged. Blocks were arranged with respect to the beam angle.

Assisting and shielding helium on the upper surface was delivered with 30 l/min flow rate; no shielding was needed on the backside surface of the joint, as the idea is to deal with a realistic lap joint configuration where no access is allowed on the back-side; 80 mm long lap welded joints were produced in continuous wave emission. At first sight, the effect of laser beam angle on spattering on the top-side plate is detectable: specimens which were processed with 15° angle are less affected by spatters compared with those ones with 5° angle, other factors being equal.

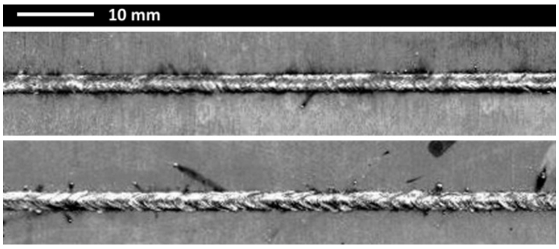

**FIGURE 6.20** – AA 2024 lap welded samples: top-side aspects in condition 5 (above) and 6 (below)

A proper beam angle may therefore aesthetically improve the beads; the need for post processing operations is hence reduced. Top-side appearances of the welds in conditions 5 and 6 are shown in **figure 6.20**. Three cross cuts for each bead were considered to be measured. As one may already expect, it is clear from the cross-sections that melting is easier for the upper than the lower sheet because the former behaves as heat sink for the latter. Nevertheless, melting in the lower plate was always produced, although with different depth, in each testing condition. With respect to the shape, three types of cross-sections can be distinguished, as shown in **figure 6.21**, and will be referred to as type-1 when presenting root concavity $RC$; type-2 when presenting excessive penetration $EP$; type-3 when penetration depth $PD$ does not range throughout the entire thickness, although a small distortion due to thermal effects is detected in this case on the bottom of the plate. Type-2 beads are slim and lean compared with type-1; $RC$ and $EP$ are mutually exclusive. Macrographs of the real cross-section for each type of bead are also shown in **figure 6.22** for conditions 12, 4 and 8. No undercuts were noticed, whilst reinforcement $R$ was always produced. Crown width $CW$, mean width $MW$ at the interface and root width $RW$ were also measured (cf. **figure 4.3**). As no boundaries of the heat affected zones were detected from micrographs, only the extent of the fused zone $FZ$ was considered. Mean values of geometric features and imperfections are listed in **table 6.9**.

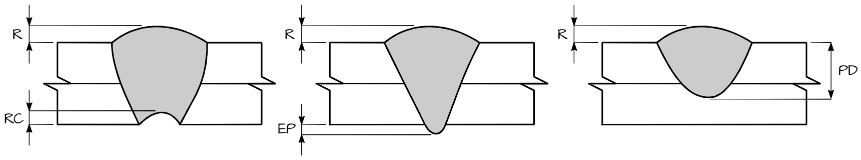

**FIGURE 6.21** – Cross-section types for lap welded beads: schemes

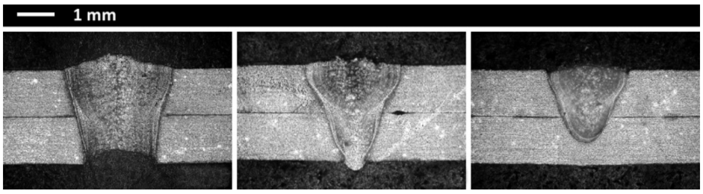

**FIGURE 6.22 –** Cross-section types for lap welded beads: macrographs

Being 2.5 mm the thickness of the resultant assembly, stringent quality requirements were met for each tested conditions in terms of reinforcement as $R$ was lower than 0.575 mm [66]. Referring to type-1, the quality level for $RC$ was found to be different depending on the processing condition, although the intermediate quality was met at least, being $RC$ not higher than 0.500 mm; referring to type-2, the quality level for $EP$ was stringent for most of the cases and intermediate for two of them. Referring to type-3, the specification allows lack of penetration in percentage on the total thickness, so moderate level is met when $PD$ is 1.875 mm at least; butt joints should be rejected for lower penetration, whereas the target is deemed to be quite conservative for lap welding since no transversal interface is present, compared with butt joining.

**TABLE 6.9 –** DOE: response variables, mean values for each testing condition

| Cond. | Cross-section type | RC [mm] | EP [mm] | PD [mm] | R [mm] | CW [mm] | MW [mm] | RW [mm] | FZ [mm$^2$] |
|---|---|---|---|---|---|---|---|---|---|
| **1** | 3 | | | 1.91 | 0.10 | 2.42 | 1.07 | | 2.93 |
| **2** | 1 | 0.26 | | 2.50 | 0.31 | 2.58 | 1.74 | 1.45 | 5.04 |
| **3** | 1 | 0.06 | | 2.50 | 0.19 | 2.52 | 1.78 | 1.52 | 5.23 |
| **4** | 2 | | 0.27 | 2.50 | 0.21 | 2.65 | 1.65 | 0.78 | 4.76 |
| **5** | 3 | | | 1.60 | 0.10 | 2.15 | 0.74 | | 2.27 |
| **6** | 2 | | 0.23 | 2.50 | 0.10 | 2.22 | 1.36 | 0.89 | 3.82 |
| **7** | 3 | | | 2.41 | 0.31 | 2.23 | 1.39 | | 3.67 |
| **8** | 3 | | | 2.14 | 0.14 | 2.30 | 1.45 | | 3.48 |
| **9** | 2 | | 0.28 | 2.50 | 0.24 | 2.67 | 1.46 | 0.56 | 4.62 |
| **10** | 1 | 0.32 | | 2.50 | 0.50 | 2.90 | 2.19 | 1.77 | 6.34 |
| **11** | 1 | 0.22 | | 2.50 | 0.13 | 2.72 | 2.15 | 2.23 | 6.38 |
| **12** | 1 | 0.35 | | 2.50 | 0.35 | 2.94 | 2.17 | 1.67 | 5.88 |
| **13** | 3 | | | 2.09 | 0.14 | 2.37 | 1.15 | | 3.12 |
| **14** | 1 | 0.29 | | 2.50 | 0.43 | 2.40 | 1.72 | 1.56 | 4.84 |
| **15** | 2 | | 0.23 | 2.50 | 0.30 | 2.34 | 1.70 | 1.48 | 4.92 |
| **16** | 1 | 0.18 | | 2.50 | 0.35 | 2.47 | 1.61 | 1.22 | 4.53 |

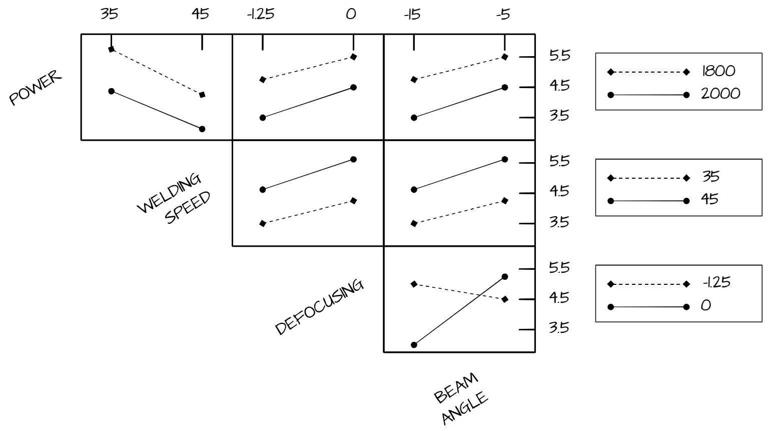

**FIGURE 6.23** – Interaction plots for the extent of the fused zone

Eventually, any welding condition in the experimental plan was adequate to make the quality requirements be matched.

The interactions among the processing factors were examined. In particular, any effect was related to the extent of the fused zone which is often considered to be a reasonable response variable to be investigated as it affects the bead ultimate tensile strength [95], as discussed for butt welded samples. The interaction plots are shown in **figure 6.23**. As one may expect, $FZ$ increases with increasing power or decreasing welding speed, so with increasing thermal input. Data lines are nearly parallel when referred either to power and speed; a correlation between defocusing and beam angle is expected instead, as the trends change when comparing focused to defocused conditions. The beam geometry adequately explains the difference. Given that a laser beam is symmetrically hyperbolic with respect to its waist (cf. par. 2.5), the irradiation area on the upper surface would be elliptic in general when tilting the laser head, and a different spatial intensity distribution would be achieved along the radius. Although the irradiance on the upper sheet was proven to still be adequate to allow the process to start, the eccentricity of the spot is higher when using a tilting angle of 15°. As shown in **figure 6.24**, this effect is enhanced when defocusing, as the intersection between the laser beam and the surface plane locates where the beam divergence is higher.

When coupled with certain levels of power and welding rate, the beam angle produces a variation in the energy profile which may prevent welding from being fully penetrative. The advantages of a collimated beam with very low divergence, as provided with a thin disk source, are thus evident since the beam radius does not undergo significant variations within moderate propagation distances; therefore the variation of the spatial intensity distribution from a focused condition to a defocused one is lower when tilting the beam. Indeed, three out of five type-3 beads were obtained when coupling 1.25 mm negative defocusing with the wider beam angle; the remaining two having the lowest thermal input of the experimental plan, so incomplete fusion predictably occurred.

The effects of defocusing and beam angle seem to compensate each other when moving from a focused condition with an angle of 5° to a defocused condition with 15°, as the extent of the fused zone is similar. No correlation was found to model either $EM$, $RC$ and $EP$; this is inferred to be due to a series of processes and noise factors which are in place on the top- and back-side surfaces of the plates due to gas shielding interaction and vortex flux structure affecting the melted pool. Nevertheless, $CW$ and $MW$ were considered in pair: given the fact that certain welding conditions brought to non penetrative welds where no measurements of $RW$ were possible, the $MW$ to $CW$ ratio was defined to portray the cross-section shape as a function of the processing parameters. As found for the fused zone, similar trends were confirmed by the interaction plots; the eccentricity and the intersection surfaces as a consequence of the tilting angle and defocusing are then thought to also control the bead shape.

Moderate requirements were met at least when considering the pores on longitudinal cross-sections. Two conditions with no porosity were successfully achieved when welding with a power of 1.8 kW, a speed of 35 mm/s, negative

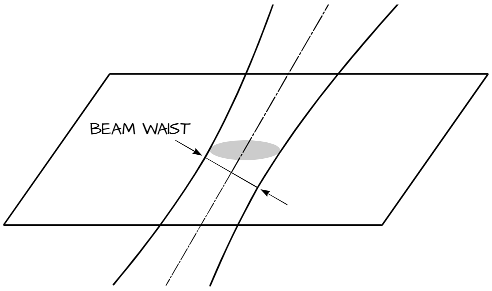

**FIGURE 6.24 –** Effect of defocusing: intersection between the laser beam and the surface plane

defocusing and a beam angle of 15°; and a power of 2.0 kW, a speed of 35 mm/s, a focused beam and a beam angle of 5°. Although the corresponding thermal input is different, the same effect on porosity formation is determined as the response of the material and the key-hole stability are obviously affected by focusing and tilting.

### 6.10 CONCLUSIONS

A number of laser-related issues are in place when welding 2024 aluminum alloy. A proper scheme for shielding and blowing the metal plume away was suggested, consisting in a trailing tilted nozzle with air cross-jet flow; the laser beam was delivered with a tilting angle of 5° in order to prevent damages to the optics due to possible back reflections. Clear advantages in coupling the laser beam with the base metal were achieved when shielding with helium compared with argon.

Proper preparation of the joint is required in order to remove aluminum oxide which may result in incomplete fusion of the abutting surfaces, and any foreign material which may produce inclusions in the bead. The need for a threshold irradiance of 18.4 $kW/mm^2$ arise as a consequence of high thermal conductivity and low absorptance at laser wavelength. Both the thermal input and the defocusing effects were proven to be effective in improving the joint quality in terms of macro pores, which are related to magnesium loss during welding thermal cycles, since a drop in magnesium concentration is found via EDS moving from the base metal towards the fused zone in the transverse cross-section. Higher thermal inputs in deep penetrative welding conditions were found to be appropriate to enhance convective vortex structure in the fused zone, thus easing the ejection of vapours; defocusing was proven to be decisive in moving the key-hole stable condition, although AA 2024 is highly susceptible to minimal focus deviation.

As a consequence of rapid heating and cooling, dissolution of strengthening precipitates occurs in the bead and the heat affected zones, so a drop in the Vickers micro hardness results in the bead. Nevertheless, when tensile testing the welded samples referring to an optimum parameter combination as suggested via desirability function, convincing values of ultimate tensile strength which are higher than 66% of the base metal were achieved, thus giving grounds for concrete application.

When considering thin sheets in overlapping configuration, wider angles of beam tilting resulted in less spattering on the upper surface, therefore providing better aesthetic features, which may be required for certain applications in order to reduce any need for post processing operations. Moreover, coupled effects due to beam angle and focus position significantly affect the joint features in terms of both the extent of the fused zone and bead cross-section, as a consequence of the position of the intersection between the laser beam and the upper surface of the plate. The advantages of a beam with very low divergence, as provided with a thin disk source, are evident such that the beam diameter does not undergo significant variations along the propagation axis.

# 7

# WELDING TITANIUM ALLOY TI-6AL-4V

## 7.1 INTRODUCTION

Titanium alloys are chosen in aerospace thanks to high strength in combination with low density and good tensile properties [106]. In particular, when the operating temperature exceeds 130 °C, titanium alloys can successfully replace aluminum-based materials [107]. Ti-6Al-4V accounts for more than half of all titanium tonnage in the world and no other titanium alloy is deemed to threaten a such dominant position [48]; it is normally and extensively employed for turbine disks, compressor blades, airframe and space capsule structural components, rings for jet engines, pressure vessels, rocket engine cases, helicopter rotor hubs, fasteners, engine exhausts. Additionally, medical and surgical devices are also produced thanks to its high biocompatibility [108].

Ti-6Al-4V is a two allotropic phase $\alpha+\beta$ alloy, aluminum acting as the alpha stabilizer and vanadium as the beta stabilizer. The chemical composition [106] is given in **table 7.1**. Strengthening is achieved through heat treatment or thermo-mechanical processing, although the best combination of properties results from solution heat treatment and rapid quenching and aging [48].

Conventional welding methods for titanium alloys are tungsten inert gas welding and plasma arc welding [109]. Research had focused on $CO_2$ [6, 110] and Nd:YAG lasers [48] to enhance the bead quality. In comparison with traditional technologies, tight beams are effective indeed in reducing the mean grain size in the fused zone; the overall mechanical quality of welded titanium is hence improved since the growth in the grain size is deemed to be the reason for the decrease in tensile strength after welding [111].

**TABLE 7.1** – Ti-6Al-4V nominal chemical composition (wt.%)

| **Al** | **V** | **Fe** | **$O_2$** | **$H_2$** | **C** | **$N_2$** | **Ti** |
|---|---|---|---|---|---|---|---|
| 5.5 ÷ 6.8 | 3.5 ÷ 4.5 | 0.4 | 0.2 | 0.015 | 0.08 | 0.05 | Balanced |

Nevertheless, for the purpose of bead protection to produce sound joints, shielding and assisting gases are crucial in laser welding [48]; moreover, a significant reduction in ductility can occur as a consequence of aluminum oxides and micro pores. In particular, as few as 2% total porosity yields a 85% decrease in the UTS of the joint compared with the base metal [111]. With respect to the micro hardness in the fused zone, a remarkable increase in the order of 140 HV occurs compared with the base metal; no clear trends in the mean value are observed with the welding speed [48], although an increase with the laser peak power has been reported [111].

## 7.2 ARRANGEMENT OF THE EXPERIMENTAL PLAN

Butt welding of 3 mm thick plates of Ti-6Al-4V titanium alloy was investigated. Laser power $P$ and welding speed $s$ were considered and a shift $f$ of the focus position was included in the experimental plan: in particular, negative defocusing was preferred because a reduction of the grain size resulted [112] when locating the beam focus beneath the metal surface.

The ranges for both power and defocusing were decided in order to overcome the threshold value of $10^6$ W/cm$^2$ for key-hole development [39] even when combining low power with strong defocusing. Sensible values for welding speed were found via BOP testing aiming to produce fully penetrative beads with no significant excessive penetration on the lower surface. Three levels were chosen for each leading variable, as listed in **table 7.2**, and a face-centred CCD structure was referred to. The resulting testing conditions to be explored are listed in **table 7.3**.

**TABLE 7.2** – DOE: factor levels for Ti-6Al-4V butt welding

| | **-1** | **0** | **+1** |
|---|---|---|---|
| **P [W]** | 1500 | 1750 | 2000 |
| **s [mm $s^{-1}$]** | 15 | 20 | 25 |
| **f [mm]** | -3.0 | -1.5 | 0 |

**TABLE 7.3** – DOE: Welding conditions to be tested in a face-centred CCD scheme

| Condition | P [W] | s [mm $s^{-1}$] | f [mm] |
|---|---|---|---|
| **1** | 1500 | 15 | -3 |
| **2** | 2000 | 15 | -3 |
| **3** | 1500 | 25 | -3 |
| **4** | 2000 | 25 | -3 |
| **5** | 1500 | 15 | 0 |
| **6** | 2000 | 15 | 0 |
| **7** | 1500 | 25 | 0 |
| **8** | 2000 | 25 | 0 |
| **9** | 1500 | 20 | -1.5 |
| **10** | 2000 | 20 | -1.5 |
| **11** | 1750 | 15 | -1.5 |
| **12** | 1750 | 25 | -1.5 |
| **13** | 1750 | 20 | -3 |
| **14** | 1750 | 20 | 0 |
| **15** | 1750 | 20 | -1.5 |

Three replications runs were performed to check the statistical dispersion. Both allocation of samples and production of the specimens were random.

The crown width $CW$, the root width $RW$ and the extent of the fused zone $FZ$ (cf. **figure 4.3**) were considered. In particular, an appropriate shape-factor was defined as the root to crown ratio to model the bead profile, aiming to involve a specific constraint at the optimization stage, as discussed in the case of aluminum alloys (cf. par. 6.8). Moreover, given that the extent of the HAZ is clearly noticed in the cross-section, its width was measured at both sides of the fused zone, on top- and back-side surfaces; the mean values $HAZ_{up}$ and $HAZ_{low}$ were referred for each testing condition. As concerning the imperfections, the evaluation was required for right and left undercut $UC$, reinforcement $R$ and excessive penetration $EP$ at the key-hole root (cf. **figure 4.4**). The mean grain size in the fused zone was additionally considered.

## 7.3 EXPERIMENTAL DETAILS

Welding was performed in continuous wave emission using a Trumpf Tru-Disk 2002, Yb:YAG thin disk laser source with a Trumpf BEO D70 focusing optics (cf. **table 2.2**). A preliminary procedure to check the focus position with respect to the surface of the plates to be welded was conducted (cf. par. 3.5).

**TABLE 7.4 –** Mechanical preparation: details for grinding and polishing Ti-6Al-4V

| Runs | Grinding/polishing medium | Wheel speed [rpm] | Processing time [min] |
|---|---|---|---|
| 2 | P1200 paper | 300 | 5 |
| 1 | P2500 paper | 300 | 5 |
| 2 | 3 µm diamond suspension | 450 | 5 |
| 2 | 1 µm diamond suspension | 500 | 5 |

Helium with a flow rate of 20 l/min was preferred as assisting gas for plume removal via a trailing copper nozzle, whilst argon was considered for both top- and back-side shielding [6, 39] via a side diffuser and a grooved box, respectively; the welding set-up in its basic scheme was hence used (cf. **figure 3.4**). The gas flow rate, the welding direction, the nozzle angle and the diffuser positioning were chosen based on trial experiments.

Possible burrs were removed using abrasive paper in order to improve the primary fit up of the plates; cleaning from residual moisture which could result in severe embrittlement of the alloy [113] was performed by pickling with 5% hydrofluoric and 30% nitric acid in distilled water mixture, for 5 min at room temperature [106]. A welding point was spotted both at the beginning and the end of the welding path. Three cross-cuts were examined for each bead; the steps for mechanical preparation are given in **table 7.4**; constant loads of 10 and 8 daN between the rotating plate and the sample holder were used in grinding and polishing, respectively; ultrasonic cleaning was carried out for 20 min at a temperature of 80 °C before diamond polishing. Chemical etching was eventually conducted for 90 s at room temperature with a solution of 10% hydrofluoric and 15% nitric acid in distilled water [106]. The geometry, the imperfections and the mean grain size along three directions in random cross-section were measured via Nikon NIS-Elements imaging software.

## 7.4 RESULTS AND DISCUSSION

Visual inspections were conducted immediately after welding. Based on the fact that uniform, smooth and shiny beads were produced, shielding was assumed to be appropriate and effective [18]. Moreover, no spatters were observed on the top-side. As an example, the top- and back-side aspect for the specimen in condition of the CCD central point are shown in **figure 7.1**. The corresponding macrograph is given in **figure 7.2**.

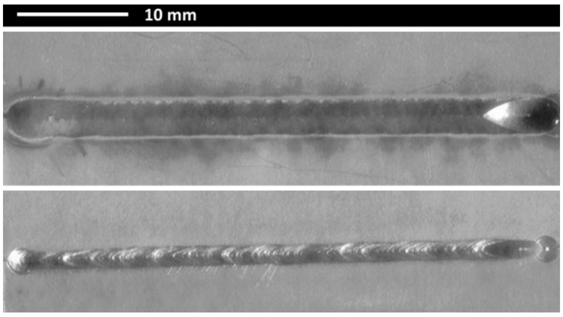

**FIGURE 7.1 –** Butt welding samples: top- and back-side bead aspect

Micro pores towards the bead root were occasionally observed in the samples: their size is not deemed to hamper the strength of the joint since comparable pores in the same alloy in the same thickness had not affected the resulting tensile strength of the welded structure [114], and fracture was experienced in the gage length, 25 mm at least away from the welding bead, with moderate elongation and limited shrinkage. With the additional assumption that any significant content of pores would be statistically detected even in random cross-sections, the beads can be considered to be structurally sound.

The mean values resulting from three cross cuts for each replication are given in **table 7.5**; missing data for $RW$, $HAZ_{low}$ and $EP$ are due to incomplete penetration of the corresponding condition, as the highest speed in conjuction with the lowest power failed to produce a fully penetrative bead.

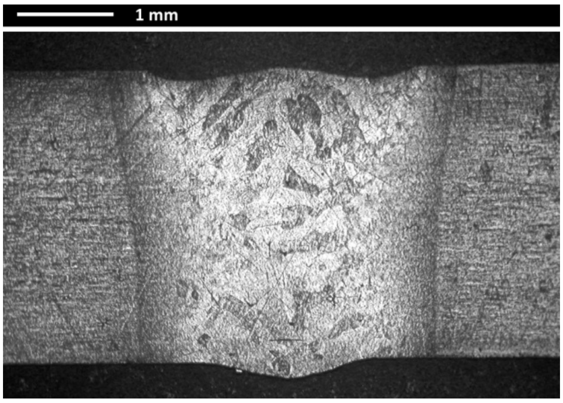

**FIGURE 7.2 –** Bead cross-section for the CCD central point

**TABLE 7.5 –** DOE: response variables, mean values for each testing condition

| Cond. | CW [µm] | RW [µm] | $HAZ_{up}$ [µm] | $HAZ_{low}$ [µm] | UC [µm] | R [µm] | EP [µm] | FZ [$mm^2$] | Grain size [µm] |
|---|---|---|---|---|---|---|---|---|---|
| **1** | 3190 | 985 | 4076 | 2260 | 25 | 140 | 61 | 10.27 | 168 |
| **2** | 3826 | 3419 | 4810 | 4477 | 52 | 123 | 167 | 15.07 | 177 |
| **3** | 2414 | | 3014 | | 66 | 25 | | 5.63 | 140 |
| **4** | 3077 | 1790 | 3643 | 2508 | 100 | -8 | 257 | 6.13 | 154 |
| **5** | 3122 | 1730 | 3758 | 2503 | 50 | 61 | 210 | 6.28 | 210 |
| **6** | 3017 | 2401 | 3296 | 3076 | 96 | 117 | 60 | 7.51 | 385 |
| **7** | 3389 | 2869 | 3799 | 3579 | 76 | 134 | 96 | 9.00 | 145 |
| **8** | 4185 | 4078 | 4760 | 4712 | 79 | 158 | 38 | 12.66 | 240 |
| **9** | 2525 | 493 | 2852 | 1660 | 55 | 76 | -31 | 4.48 | 152 |
| **10** | 3048 | 2611 | 3386 | 3055 | 155 | 107 | 179 | 7.87 | 186 |
| **11** | 2990 | 1682 | 3615 | 2399 | 86 | 75 | 237 | 5.93 | 234 |
| **12** | 3737 | 2963 | 4343 | 3801 | 118 | 137 | 199 | 9.50 | 147 |
| **13** | 4161 | 3615 | 4785 | 4420 | 79 | 145 | 150 | 11.30 | 161 |
| **14** | 2963 | 1728 | 3514 | 2359 | 138 | 125 | 210 | 5.80 | 210 |
| **15** | 3281 | 2503 | 3954 | 3227 | 105 | 64 | 229 | 8.29 | 187 |

The stringent quality requirements were met for the imperfections, although referring to standards for steel [115], since a specific international guidance for laser welding of titanium and its alloys is not available.

### 7.4.1 MICRO STRUCTURE

Special interest is given to the micro structure of titanium alloys, given that the final structure and the phase distribution resulting from cooling are considered to be closely related to the mechanical properties of the weld [113, 116].

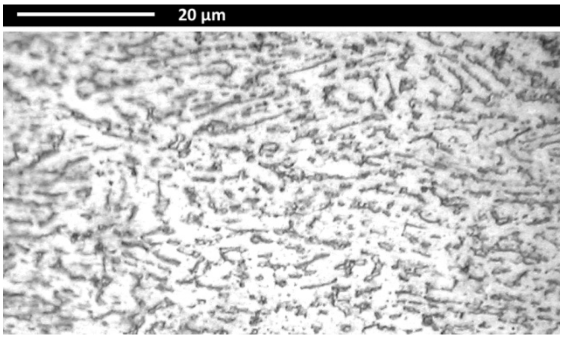

**FIGURE 7.3 –** Ti-6Al-4V, micrograph: base metal

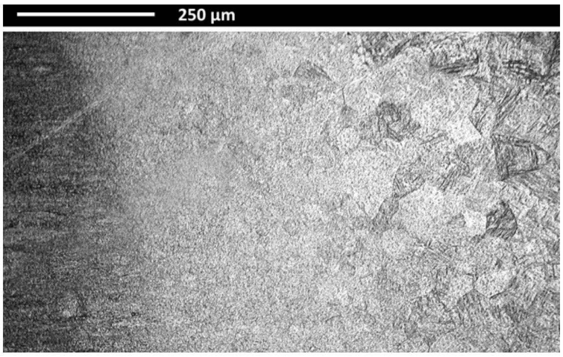

**FIGURE 7.4 –** Ti-6Al-4V, micrograph: heat affected zone

The base metal is composed of a dark β phase in a bright α matrix, which is a typical annealed structure, whose corresponding micrograph is shown in **figure 7.3**. Namely, the body-centred cubic structured β phase distributes along the boundaries of the hexagonal close-packed structured α phase [117].

Laser beam welding promotes a diffusionless transformation of the β phase into a martensitic α' micro structure; high self-quenched rates occur during the process indeed, and a value of 410 °C/s, which is required to attain a completely martensitic micro structure for Ti-6Al-4V alloy [118], is certainly overcome both in the fused zone and in the HAZ [114]. As a result, the corresponding hardness increases when compared with the reference value of the base metal [109]. In particular, the HAZ is a mixture of α' and primary α phases, as matching a structure which is quenched from a region below the β-transus temperature; the corresponding micrograph is shown in **figure 7.4**.

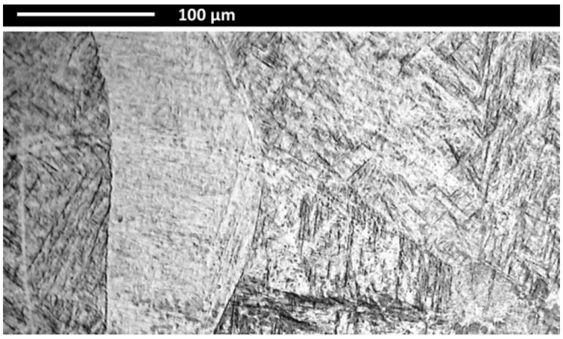

**FIGURE 7.5 –** Ti-6Al-4V, micrograph: fused zone

The fused zone mainly consists of acicular α’ martensite instead; the micrograph is shown in **figure 7.5**; a similar structure results when quenching from the β phase region above the β-transus [48].

### 7.4.2 MAIN EFFECTS

The effect of the focus position is not univocal for the responses of the experimental plan. Notably, as shown in **figure 7.6**, with respect to the extent of the fused zone as a function of the thermal input, defocusing has no effect at all on the resulting trends which are approximately comparable, hence irrespective of the focus position.

Therefore, when defocusing is neglected and the extent of the fused zone is studied as a mere function of laser power and welding speed as separate input parameters, different testing conditions end up in being overlapped for the purpose of the examination. In this case, the response of the metal to the laser beam is easier to be discussed and the expected basic relationships of the interaction between laser and material are confirmed, in accordance with existing literature on the subject of titanium welding [48], such that any increase in the laser power yields a proportional increase on $FZ$ and, similarly, any increase in the welding speed results in a corresponding decrease on $FZ$, as shown in **figure 7.7**.

Although not directly affecting the extent of the fused zone, the focus position has its clear influence on both the crown and the root width of the bead, so the profile in the cross section actually depends on defocusing.

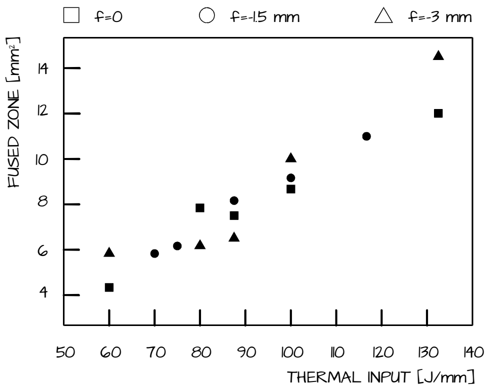

**FIGURE 7.6** – Extent of the fused zone as a function of the thermal input: effect of defocusing

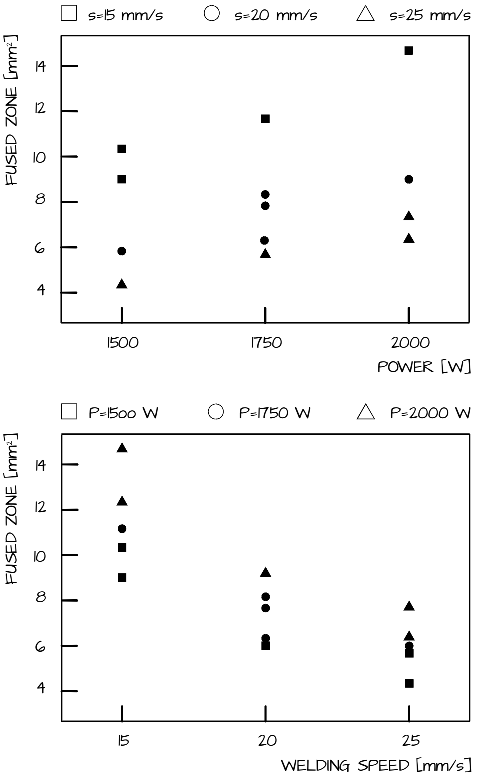

**FIGURE 7.7 –** Extent of the fused zone as a function of power and welding speed as separate inputs

As an example to support this finding, for a given thermal input of 88 J/mm, as obtained with a power of 1750 W and a welding speed of 20 mm/s, the response to a focused beam is compared with the response to a defocused one; the corresponding macrographs are shown in **figure 7.8**.

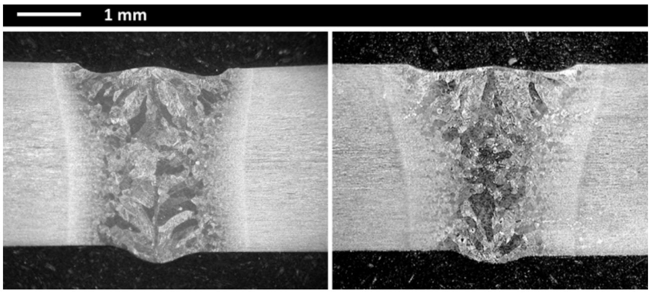

**FIGURE 7.8 –** Bead profile as resulting from a focused beam (left) and a defocused one (right)

## 7.5 OPTIMIZATION OF THE RESPONSES

Since the quality requirements were met for each possible imperfection in the beads of the experimental plan, modeling was fed with all of the welding conditions. Statistical significance was not adequate for undercut, reinforcement and excessive penetration, so the corresponding models were neglected. Furthermore, low significance resulted for the HAZ width both at the top- and the back-side also, thus depriving the optimization of a main response; nevertheless, it is assumed that a proper constraint of minimization on the fused zone extent would also act in reducing the HAZ. The resulting p-values and adjusted R-squared values to assess significance and reliability of each model are listed in **table 7.6**.

A deeper analysis is now worth performing considering the models for the variables to be involved in the optimization. As concerning the shape-factor, the corresponding response surfaces are shown in **figure 7.9**, for a given speed of 20 mm/s and a given negative defocusing of 3 mm: an increase in the laser power or a decrease in the welding speed yields a corresponding increase in the shape-factor, since the root width approaches the crown width; conversely, a decrease in the laser power or an increase in the welding speed yields a corresponding decrease in the shape-factor, as the typical shape of the key-hole is approached.

With respect to mean grain size instead, the corresponding response surfaces are shown in **figure 7.10**, for a given power of 2.0 kW and a given speed of 20 mm/s: as expected when designing the experimental plan, a decrease in the mean grain size is noticed when defocusing. Moreover, the grain size clearly ascends with an increase in power, as reported in literature [111] for both the HAZ and the weld metal, due to an increase in the thermal input; interestingly, this behavior is much more evident when a focused beam applies.

**TABLE 7.6** – ANOVA output: p-values and adjusted R-squared values for the response variables

| Response variable | p-value | Adjusted R-squared |
|---|---|---|
| **CW** | < 0.0001 | 0.952 |
| **RW** | < 0.0001 | 0.923 |
| **FZ** | < 0.0001 | 0.933 |
| **RW/CW** | < 0.0001 | 0.829 |
| **Grain size** | < 0.0001 | 0.903 |

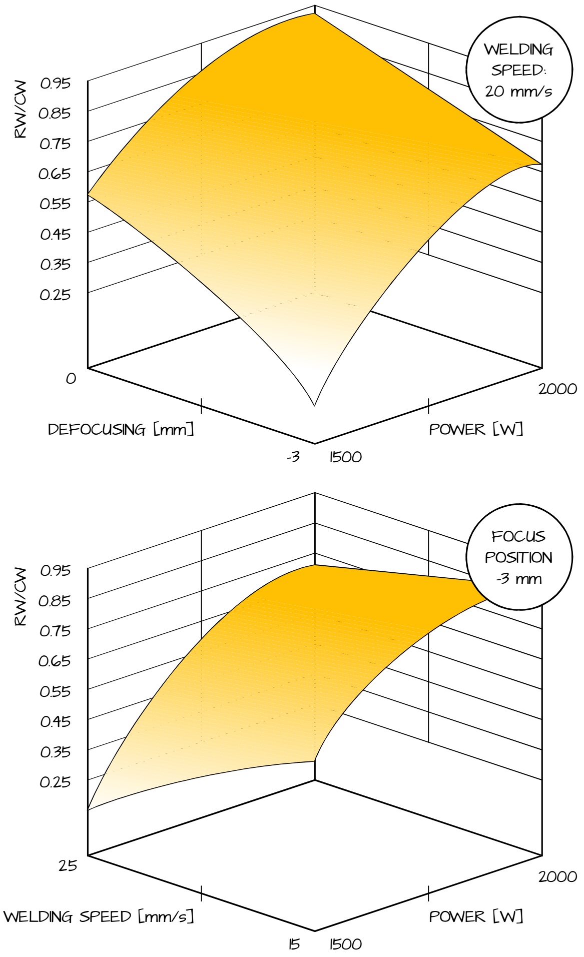

**FIGURE 7.9 –** Response surfaces for the extent of the fused zone for given speed and defocusing

A goal of minimization was required for both the extent of the fused zone and the mean grain size, such that the smallest possible area of the base metal would be affected and the smallest possible mean grain size would be achieved for the purpose of mechanical strength. Furthermore, an optimal range between 0.5 and 0.7 was chosen for the shape-factor, as discussed in the case of aluminum alloys (cf. par. 6.8); this would shift the optimum solution towards a processing set-up providing a key-hole with high aspect ratio to be additionally balanced with a proper constraint on the root width in order to ease the expulsion of vapour which would result in porosity formation otherwise.

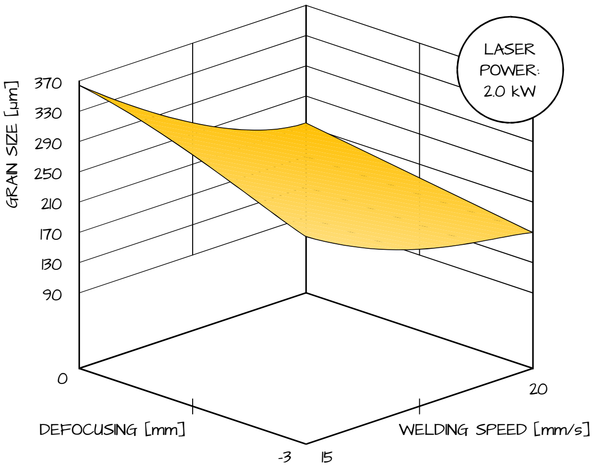

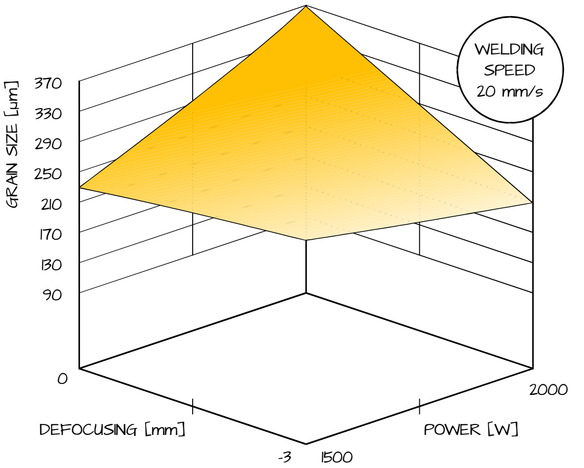

**FIGURE 7.10** – Response surfaces for mean grain size for given power and speed

A higher importance in the numerical optimization was awarded to the constraint involving the grain size. Predictably, the suggested optimum welding set-up would move towards a condition of negative defocusing. An optimal welding condition with a power of 1820 W, a speed of 23 mm/s with 3 mm of negative defocusing is suggested, with an overall desirability of 92%.

## 7.6 CONCLUSIONS

Welding of 3 mm thick plates of Ti-6Al-4V titanium alloy was investigated in square butt welding configuration. Uniform, smooth and shiny beads were produced. The fused zone consisted of acicular α’ martensite because the welding thermal cycles resulted in quenching the alloy from the β phase region above the β-transus; a mixture of α’ and primary α phases was found in the HAZ instead, as matching a structure which is quenched from a region below the β-transus temperature.

Stringent quality was met for imperfections such as undercut, reinforcement and excessive penetration. The trend of the extent of the fused zone was not affected by the focus position, although a clear effect of defocusing on the crown and the root width was noticed, with a resulting influence on the bead profile in the cross-section. A decrease of the laser power, or an increase of the welding speed, yields a corresponding decrease in the root to crown width ratio, as the typical shape of the key-hole is approached; a decrease in the mean grain size was noticed when defocusing.

When requiring a constraint of minimization for both the extent of the fused zone and the mean grain size, with an additional goal of target for the shape-factor, a solution with a power of 1820 W, a speed of 23 mm/s with 3 mm of negative defocusing was found with an overall desirability of 92%.

# 8

# DISSIMILAR WELDING HAYNES + INCONEL

## 8.1 INTRODUCTION

The development of super alloys dates back in the early 1940s, when available conventional materials were inadequate to meet the demanding stress, temperature and environmental requirements for critical propulsion system in aero gas turbine applications [119] for combustion zone components, afterburners, tailpipes, casing, liner, exhaust ducts, bearing housing and many others [120, 121]. A gas turbine scheme with corresponding qualitative trend for the operating temperatures as a function of the position in the engine is shown in **figure 8.1**: temperatures above 1200 °C are experienced in the combustion chamber. With respect to gas turbines in their whole life cycle, new technologies have been constantly developed in the aerospace, in a bid to reduce operating and designing costs, which are normally accounted to engines in measure of 40% [122].

Thanks to thermal treatments of solid solution and precipitation hardening, super alloys normally exhibit a combination of increased mechanical strength and creep rupture properties at operating temperature which are close to their melting point [123], as well as resistance to environmental attack including oxidation. These features make them suitable for chemical and metallurgical processing, energy generation, oil and gas extraction and refining also [124].

Base elements in super alloys are generally nickel and cobalt, while property enhancement is mainly achieved by the addition of aluminum, chromium, iron, molybdenum, titanium and tungsten. Alloying elements may segregate to the grain boundaries or lead to precipitation of a finely dispersed hardening phase

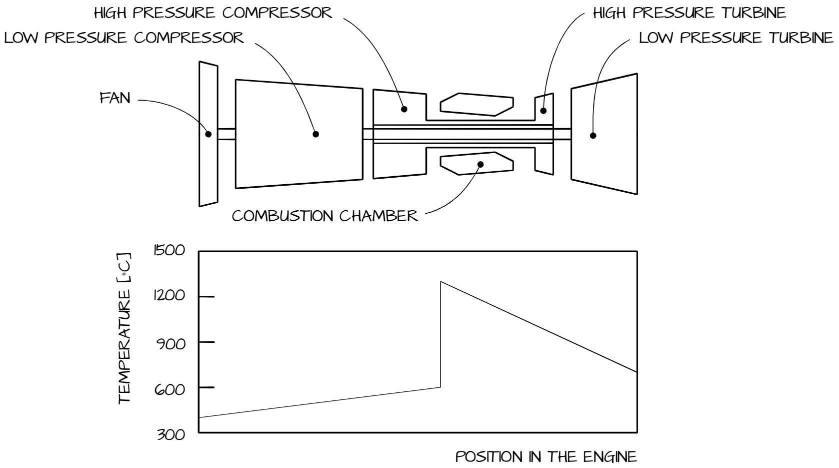
HIGH PRESSURE COMPRESSOR
LOW PRESSURE COMPRESSOR
HIGH PRESSURE TURBINE
LOW PRESSURE TURBINE
FAN
COMBUSTION CHAMBER
TEMPERATURE [°C]
1500
1200
900
600
300
POSITION IN THE ENGINE

**FIGURE 8.1** – Gas turbine scheme: operating temperatures as a function of the position in the engine

in the base matrix; as a consequence, the material is significantly improved in strength [120]. Nevertheless, super alloys are usually processed for property optimization, so they can be used as wrought or cast, to be chosen depending on the application; for a given nominal composition, different structures result from deformation processing or casting indeed. That is: wrought super alloys have generally finer grain sizes as well as improved tensile and fatigue properties; on the other hand, cast alloys have coarser grain sizes, significant alloy segregation and improved creep and rupture characteristics [125].

Haynes 188 and Inconel 718, whose nominal chemical compositions are listed in **table 8.1** and **table 8.2**, are among the most common and representative aerospace super alloys. Both of them are widely used in established military and commercial gas turbine engines, and they are generally preferred among

**TABLE 8.1** – Haynes 188 nominal chemical composition (wt.%)

| Ni | Cr | W | Fe | Mn | Si | C | La | Co |
|---|---|---|---|---|---|---|---|---|
| 22 | 22 | 14 | 2 | 1.25 | 0.35 | 0.10 | 0.03 | Balanced |

**TABLE 8.2** – Inconel 718 nominal chemical composition (wt.%)

| Cr | Fe | Nb | Mo | Ti | Al | Cu | C | Ni |
|---|---|---|---|---|---|---|---|---|
| 19 | 18.5 | 5.1 | 3 | 0.9 | 0.5 | 0.15 | 0.08 | Balanced |

other age-hardenable ones such as Waspaloy, René 41, Inconel X750 and Udimet 700 which have been reported to suffer from post welding heat treatment cracking [126]. Nevertheless, new processing welding methods are addressed special consideration to both improve quality and reduce costs. In particular, special interest has been shown in dissimilar welding.

## 8.2 SUPER ALLOYS WELDING

Arc welding is considered to be the conventional joining method for super alloys, although high stress levels result in the bead, thus limiting certain practical applications [127]. Electron beam welding has been proposed [119, 128]. This first allows to prevent possible contamination from the material of the electrode [2]; nevertheless, in addition to any common issue the technology implies (cf. par. 1.3), it has been pointed out that two beam passes are needed in general for Inconel welding, the first one being fully penetrative and the second one to be performed for cosmetic reasons, with lower thermal input and larger beam size to reduce the surface undercut resulting from the first pass [128]. A single pass would limit the overall processing time instead, as well as prevent fusion misalignment which may result from a gap between the centre-lines of two beam passes from opposite sides of the joint [52].

Moreover, micro fissuring in the heat affected zone as well as a high amount of brittle intermetallic niobium rich Laves phase, which are well recognized to be detrimental to mechanical properties [129], are noticed both in arc and electron beam welding of Inconel [12, 130]. Although post weld solution treatments have been considered to approach the issue of Laves phases [131], dissolution is rather difficult to achieve because of the poor diffusivity of large niobium atoms [12].

Relative advantages would arise from using any welding technology with lower thermal inputs: laser beam welding is then naturally suggested. With respect to this technique, undesired curvature of the bead surface and consequent cavity upon solidification have been reported when welding Haynes [127]; the occurrence of weld instability [132] and micro fissuring as well [126] must be addressed when considering Inconel, whose properties are generally kept in laser welded joints even at high operating temperature [122]. Dissimilar joining of Haynes 188 and Inconel 718 has been performed with linear friction welding [133], which is expected to result in larger beads.

## 8.3 ARRANGEMENT OF THE EXPERIMENTAL PLAN

Reasons to prevent defocusing on super alloys are pointed out in literature with respect to experimental welding of Inconel 718 with $CO_2$ lasers, as focus positions above or below the upper surface resulted in porosity, spatters or concave welds [14]. As a consequence, any stand-off of the focal position was discarded in the experimental plan. The influence of the laser beam angle was considered instead. Therefore, a 3-factor study with power $P$, welding speed $s$ and beam angle $\alpha$ with respect to the welding direction was arranged in fractional design.

Sensible outer limits of the range to be explored for each factor were found via ad hoc BOP extensive trials on base metals, as well as referring to previous studies on similar super alloys [134]: in principle, fully penetrative beads with no oxidation and no significant drop-through are aimed. Limits are then in place for the outer domain, so a face-centred CCD scheme was planned; factor levels for each processing parameter and corresponding testing conditions are shown in **table 8.3** and **table 8.4**, respectively.

Further considering two additional tests for the CCD central point and three runs for each condition, a total of 51 welding beads specimens was produced. Both the run order and the allocation of the sheets to each test were random. Nevertheless, blocks were considered with respect to the beam angle.

Aiming to develop a welding procedure which would be both feasible and effective for actual components, the conditions to be satisfied for acceptance of welds and therefore the output parameters to be measured were defined referring to customer specifications. The idea is to first perform successive NDT such as visual examinations, FPI and RT. Since cracks and porosity can be a factor due to rapid cooling in laser welding [119], the total number of indications $NI$ was considered as the response variable coming from NDT. Before cutting the specimens, the buckling distortion angle $\beta$ between the

**TABLE 8.3 –** DOE: factor levels for Haynes + Inconel dissimilar welding

| | **-1** | **0** | **+1** |
|---|---|---|---|
| **P [W]** | 1000 | 1200 | 1400 |
| **s [mm $s^{-1}$]** | 30 | 45 | 60 |
| **α [°]** | -10 | 0 | 10 |

**TABLE 8.4** – DOE: Welding conditions to be tested in a face-centred CCD scheme

| Condition | P [W] | s [mm $s^{-1}$] | α [°] |
|---|---|---|---|
| **1** | 1000 | 30 | -10 |
| **2** | 1000 | 30 | 10 |
| **3** | 1000 | 45 | 0 |
| **4** | 1000 | 60 | -10 |
| **5** | 1000 | 60 | 10 |
| **6** | 1200 | 30 | 0 |
| **7** | 1200 | 45 | -10 |
| **8** | 1200 | 45 | 0 |
| **9** | 1200 | 45 | 10 |
| **10** | 1200 | 60 | 0 |
| **11** | 1400 | 30 | -10 |
| **12** | 1400 | 30 | 10 |
| **13** | 1400 | 45 | 0 |
| **14** | 1400 | 60 | -10 |
| **15** | 1400 | 60 | 10 |

welded plates is an interesting variable to be measured in order to consider the heating effect. The appearance of the bead cross-section was then considered. A peculiar shape profile, which is generally referred to as dumbbell-like cross-section [12] and is shown in **figure 8.2**, is expected when welding super alloys with argon shielding: a necking zone is noticed indeed, approximately halfway between the bead crown and root. A description of this shape, with corresponding limits to be matched for crown width $CW$, necking width $NW$ and root width $RW$ is given in the referred customer specification. The dimensional limits for specific common imperfections and shape dimensions are also provided. In particular, checks are required for undercut $UC$, shrinkage groove $SG$, reinforcement $R$, excessive penetration $EP$, incompletely filled

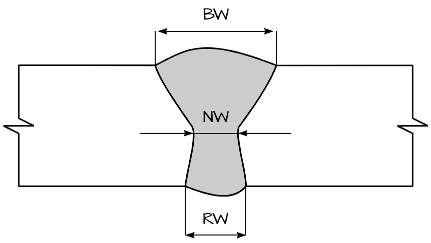

**FIGURE 8.2** – Dumbbell-like cross section as expected when welding super alloys

groove $IFG$, root concavity $RC$ and linear misalignment $M$ (cf. **figure 4.4**). Additional measurements for the extent of the fused zone $FZ$ were considered to model the response, although no prescriptions at all are suggested, as for the buckling distortion angle; nevertheless both $FZ$ and $\beta$ are expected to be crucial in the optimization.

## 8.4 EXPERIMENTAL DETAILS

Sheets of 1175 °C bright annealed Haynes 188 and 980 °C solution treated Inconel 718, 1.5 mm thick, were considered. A Trumpf Tru-Disk 2002 Yb:YAG disk-laser with BEO D70 focusing optics (cf. **table 2.2**) was employed. A check for the focus position was preliminary carried out (cf. par. 3.5).

For super alloys successful welding, different inert gases such as helium [14], or adequate mixture of argon and helium, of not less than 99.995% purity by volume have been suggested to shield the weld pool, thus preventing contamination. Argon was considered in this study as it would provide an ideal compromise between effectiveness and economic needs in industrial environments. A special device for gas supply was designed to upgrade the welding head; a 30° tilted trailing nozzle, with 7.8 mm outlet diameter was employed: assisting gas at 15 l/min flow rate was supplied to blow the ionized metal plume away from the interaction zone between the beam and the material; at the same time, top-side shielding to prevent oxidation during cooling was achieved through a side diffuser with 2 mm gap to the top surface of the joint. Both the nozzle and the diffuser move with the laser head, whilst a fixed grooved box provides back-side shielding as the beads are aimed to be produced in fully penetrative conditions. The welding system set-up in its basic scheme was therefore considered (cf. **figure 3.4**); with respect to beam tilting, the usual convention of positive anticlockwise angles applies (cf. **figure 3.6**) such that negative tilting is intended to focus the beam in the pool; argon flow rate, welding direction, nozzle angle and diffuser positioning were based on trial experiments.

### 8.4.1 PRE WELDING PROCEDURES

Appropriate marks were engraved on each sheet via vibrating tools to track the specimens. Given that square joints in butt configuration are to be produced, frontal milling was performed on the butting edges in order to generate uniformly smooth surfaces thus preventing possible differences among the specimens and consequent uneven gaps; possible burrs were removed using abrasive paper. Austenitic stainless steel wire brushes were used to clean the abutting surfaces; further degreasing with acetone-wetted swab was performed just before welding once sheets had been flat clamped on the grooved box. Then, the welding path was set: a system-integrated camera was employed for the purpose of fit up (cf. par. 6.3). A welding point was spotted both at the beginning and the end of the joint, using a single rectangular pulse input with a peak power of 800 W for 10 ms, to better tighten the samples and prevent slippage during melting. No pre heating was performed, being it pointless when welding super alloys, provided that cold base material is brought up to room temperature to prevent condensation issues [119]. A 5 s waiting period was set in order to allow the argon to adequately prepare the welding area. Eventually, 100 mm long welds were produced in single pass in continuous wave emission mode. An additional 5 s waiting period was set for the diffuser to complete shielding the joint.

### 8.4.2 POST WELDING PROCEDURES

Since the aim of the work is the evaluation of as-welded joints, no mechanical finishing was performed after welding, although allowed according to the specifications to meet misalignment, reinforcement and excessive penetration limits, provided it does not result in reducing the original thickness in the base material or affecting the metallurgical characteristics of the bead.

Visual inspections were carried out to check both the shielding effectiveness and the joint penetration. FPI and RT were performed; a 13 mm (i.e. 0.5 in) long zone both at the beginning and at the end of the bead was excluded from measurements, in order to neglect any transitory effect due to opening and closure of the weld pool. Then the buckling distortion angle was measured using a DEA Global Image Clima coordinate measuring machine.

To perform the metallographic analysis, each butt sample was cross-cut at half-length, perpendicularly to the welding direction, then mounted in phenols and polished to mirror finish with SiC paper and grinding diamond paste on polishing cloths. An appropriate procedure was appointed to address the challenge of polishing dissimilar metals when mounted together; the steps for mechanical preparation are listed in **table 8.5**; both automatic grinding and polishing were carried out with a constant load of 10 daN between the rotating plate and the sample holder.

**TABLE 8.5 –** Mechanical preparation: details for grinding and polishing Haynes + Inconel

| Runs | Grinding/polishing medium | Wheel speed [rpm] | Processing time [min] |
|---|---|---|---|
| 1 | P400 paper | 120 | 1 |
| 1 | P800 paper | 120 | 1 |
| 1 | P1200 paper | 120 | 1 |
| 1 | 9 µm diamond suspension | 80 | 2 |
| 1 | 6 µm diamond suspension | 80 | 2 |
| 1 | 3 µm diamond suspension | 80 | 2 |

Chemical etching was carried out for 5 min at room temperature with Kalling reagent number 2 solution, consisting of 5 g cupric chloride in 100 ml hydrochloric acid and 100 ml ethanol solution [120]. Etched specimens were eventually blow dried and observed via optical microscopy using Nikon NIS-Elements imaging software for imperfections and geometry evaluations.

## 8.5 RESULTS AND DISCUSSION

Visual inspections were carried out on both sides of the bead: no spatters were observed; bead width both on the upper crown and the lower root were found to be constant along the welding line; also no discoloration, and therefore no oxidation, were detected on the top-side surface neither on the back-side one, thus confirming adequate flow rate and diffuser positioning. As an example, upper and lower bead surfaces for the CCD central point specimen are shown in **figure 8.3**. Uninterrupted fusion throughout the complete length of the joint must be achieved when welding from the upper side of the joint, unless otherwise designated: this caused rejection for the specimens in condition 5, which did not comply with the complete penetration requirement and

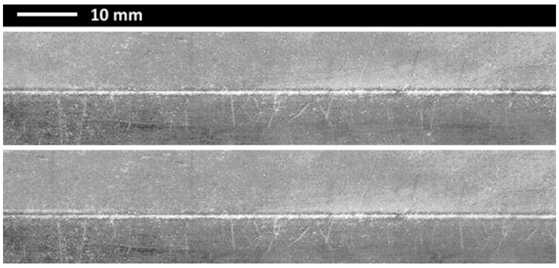

**FIGURE 8.3 –** Dissimilar welding samples: top- and back-side aspect; Haynes above, Inconel below

**TABLE 8.6** – DOE: response variables, mean values for each testing condition

| Cond. | NI [/] | β [°] | CW [μm] | NW [μm] | RW [μm] | UC [μm] | SG [μm] | R [μm] | EP [μm] | IFG [μm] | RC [μm] | M [μm] | FZ [mm$^2$] |
|---|---|---|---|---|---|---|---|---|---|---|---|---|---|
| **1** | 13 | 0.33 | 1399 | 708 | 1195 | 29.1 | 2.1 | 7.72 | 35.7 | | | 26.9 | 1.71 |
| **2** | 17 | 1.20 | 1494 | 594 | 851 | 44.3 | 3.4 | | 21.2 | 12.7 | | 48.0 | 1.48 |
| **3** | 2 | 0.69 | 931 | 457 | 792 | 74.2 | 22.7 | 10.38 | 5.1 | | | 22.2 | 0.96 |
| **4** | 22 | 1.56 | 880 | 378 | 497 | 115.1 | 10.1 | | 14.8 | 64.0 | | 10.9 | 0.85 |
| **5** | Excluded due to lack of penetration | | | | | | | | | | | | |
| **6** | 0 | 0.00 | 1284 | 711 | 1286 | 69.3 | 51.5 | | 5.5 | 32.9 | | 26.9 | 1.55 |
| **7** | 0 | 0.40 | 1061 | 509 | 948 | 51.7 | 5.5 | | | 20.4 | 2.4 | 9.4 | 1.17 |
| **8** | 0 | 0.00 | 959 | 493 | 923 | 78.9 | 36.1 | | | 6.50 | 6.1 | 20.9 | 1.02 |
| **9** | 13 | 1.39 | 1224 | 478 | 675 | 46.2 | 0.00 | 36.31 | 9.6 | | | 6.3 | 1.12 |
| **10** | 2 | 0.48 | 875 | 460 | 779 | 24.6 | 0.0 | | 0.00 | 4.81 | 0.00 | 3.0 | 0.90 |
| **11** | 0 | 0.00 | 1320 | 785 | 1453 | 57.4 | 27.1 | 5.29 | 25.7 | | | 32.1 | 1.82 |
| **12** | 0 | 0.37 | 1604 | 865 | 1404 | 85.2 | 12.0 | | 17.6 | 36.9 | | 12.5 | 2.01 |
| **13** | 0 | 0.15 | 1027 | 519 | 1020 | 53.3 | 17.9 | | | 26.7 | 9.6 | 20.1 | 1.11 |
| **14** | 0 | 0.00 | 924 | 470 | 884 | 46.2 | 26.4 | | 14.6 | 12.0 | | 17.3 | 1.03 |
| **15** | 0 | 1.31 | 1091 | 464 | 801 | 44.2 | 0.00 | | 4.1 | 12.4 | | 26.5 | 1.10 |
| **Limits** | | | 3150 | 953÷1690 | 1650 | 150 | 150 | 330 | 330 | 250 | 250 | 75.0 | |

consequently did not undergo further analysis; besides, measurements for certain chosen response variables would not be possible. Notably, the condition 5 is actually on the edge of the CCD domain.

The evaluation of the response variables was carried out on the remaining fully penetrative specimens. The resulting outputs are given in **table 8.6**, with corresponding limits for quality compliance; mean values are listed, although quality checks were referred to each single measurement, as compensation in the arithmetic mean would lead to misjudgments otherwise.

No indications of surface porosity neither cracks resulted from FPI along the whole bead, while evidence of inclusions or subsurface porosities was detected via RT. According to the specification, when welding nickel alloys, indications are allowed for stringent quality class compliance, provided they lay below a maximum size of 0.3 mm in diameter or length, a minimum distance of 10 times the size of the largest adjacent indication and an accumulative length of 0.3 mm per 25 mm of weld. A number of 6 specimens did not comply with this; nevertheless, NDT did never completely reject a certain welding condition, as one replication at least was accepted. Moreover, although any NDT outcome is generally treated as acceptance/rejection depending on limits for allowable indications, the proposal is to consider all of the beads anyway in the analysis, provided they are fully penetrative, thus to offer a much more robust model to characterize the effects of the processing parameters: the assumption is that proper optimization criteria would eventually exclude any welding condition which does not meet the specification. Interestingly, the specimens with the highest number of NDT indications also did not meet the referred specification in terms of allowed maximum size and minimum distance between consecutive indications; this actually supports the choice of total amount of indications as significant response variable to be discussed.

A macrograph of the dumbbell-like cross-section for the specimen in the central point condition is shown in **figure 8.4**: as a consequence of whirling flow of the melted metal when a key-hole welding condition is produced [5], Haynes and Inconel were found to be mixed in the fused zone. Several aspects are influenced by the cooling rate, since the scale of the dendritic structure is in inverse proportion to the solidification cooling rates, for any heavily alloyed material which solidifies in dendritic mode, as Inconel 718 actually is; consequently, a fine dendritic structure results in the weld fusion zone when using laser sources [12].

All of the welded specimens complied with quality checks in terms of shrinkage groove, reinforcement, excessive penetration, incompletely filled groove and root concavity. As one may expect, reinforcement and incompletely filled groove on the upper surface are mutually exclusive, as well as excessive penetration and root concavity on the back-side. As two replications at least

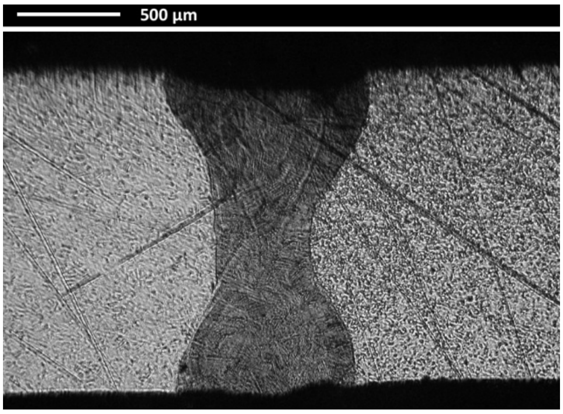

**FIGURE 8.4 –** Cross-section for the CCD central point; Haynes on the left, Inconel on the right

were accepted after dimensional checks on defects, none of the processing conditions was rejected at all; a single out-layer of 107 µm for misalignment in condition 5, plus two out-layers of 183 and 169 µm for undercut in conditions 3 and 9, respectively, were found.

The dumbbell-like shape of the bead cross-section was considered at the next step. Both $CW$ and $RW$ met the specification, interestingly with considerable tolerance with respect to the corresponding threshold values; in particular 36% and 63% narrower width were obtained on average for crown and root, respectively. This drives to a much smaller fused zone and, as a consequence, the resulting necking zone is significantly thinner and it ends up to be shifted when compared with the assigned range in the referred specification. In a way which is consistent with the principle of the normative, a lower limit of 30% and an upper one of 60% with respect of the crown width are suggested in order to provide a more realistic reference to judge even tighter beads as resulting when performing laser welding instead of arc welding.

## 8.6 OPTIMIZATION OF THE RESPONSES

With the only exclusion of condition 5 due to lack of penetration, all of the examined welding conditions which have been examined in the experimental plan are adequate to make the quality requirements be matched in terms of compliance to NDT, limits for each possible imperfection and shape geometry. The ANOVA was therefore carried out upon the responses.

### 8.6.1 MODELING THE RESPONSE VARIABLES

Misalignment was deemed to result from improper clamping; therefore, the analytic model was neglected and the corresponding measurements were used with the only purpose of quality checks. Shape-factors $CW/NW$ and $CW/RW$ were defined at this stage in order to give a synthetic description of the bead profile in the cross-section, thus easing both the modeling of the bead dumbbell-like shape and the definition of the optimization constraints. A lack-of-fit test with step-wise regression method was used to eliminate any non significant term in each model [75] whose overall significance was eventually assessed in terms of p-values and adjusted R-squared. Once modeled, the undercut, the shrinkage groove, the reinforcement, the excessive penetration, the incompletely filled groove and the root concavity did not show adequate significance and were then neglected.

**TABLE 8.7** – ANOVA output: p-values and adjusted R-squared values for the response variables

| Response variable | p-value | Adjusted R-squared |
|---|---|---|
| **NI** | < 0.0001 | 0.438 |
| **β** | < 0.0001 | 0.896 |
| **CW/NW** | < 0.0001 | 0.723 |
| **CW/RW** | < 0.0001 | 0.881 |
| **FZ** | < 0.0001 | 0.877 |

It is inferred that a random influence arise due to both the upper and lower gas fluxes, which directly interact with the fused metal, although supplied at constant flow rate to result in perfect shielding. On the other hand, good modeling answers were provided for the number of indications, the buckling angle, the extent of the fused zone and the shape-factors; the resulting p-values and adjusted R-squared values are listed in **table 8.7**. The ANOVA-significant response variables were considered to feed the optimization process with the corresponding constraints.

### 8.6.2 CONSTRAINT CRITERIA FOR OPTIMIZATION

With respect to the bead aspect, each constraint for optimization was awarded different importance on a technological basis. In principle, the minimization of the fused zone is required, aiming to reduce the amount of material which is directly affected by the laser beam; an importance of 2 was awarded, since previous measurements on cross-section crown and root widths had already shown an excellent agreement with the specification.

With respect to the shape, instead, any constraint must be consistently referred to the actual behavior of the alloy in the cross-section, this meaning that a demand for a steep key-hole is not feasible; nevertheless, an ideal regular rectangular geometry with no necking zone and with adequate fusion on both the upper and the lower surface should be achieved, so both the shape-factors were targeted to 1, although a higher importance of 4 against 2 was awarded to the factor involving $NW$, being it related to the zone where stresses would be critical in case of improper shape with significant necking. Maximum importance was rated for the goal of minimization of total indications and the buckling angle, the former relating to possible weakening in the bead, the latter being an evidence of residual thermal stresses which are detrimental to the operating life of the welding bead.

**TABLE 8.8** – Optimization: suggested solutions with corresponding responses and desirability

| | P [W] | s [mm $s^{-1}$] | α [°] | NI | β [°] | CW/NW | CW/RW | FZ [$mm^2$] | Desirability |
|---|---|---|---|---|---|---|---|---|---|
| **1** | 1345 | 55.7 | -7.47 | 0 | 0.00 | 1.98 | 1.00 | 0.98 | 0.888 |
| **2** | 1345 | 55.8 | -7.52 | 0 | 0.00 | 1.98 | 1.00 | 0.98 | 0.887 |
| **3** | 1249 | 48.5 | -1.84 | 0 | 0.07 | 1.94 | 1.00 | 0.99 | 0.887 |
| **4** | 1247 | 48.1 | -1.88 | 0 | 0.06 | 1.94 | 1.00 | 0.99 | 0.887 |
| **5** | 1245 | 48.0 | -1.90 | 0 | 0.06 | 1.94 | 1.00 | 0.99 | 0.887 |

Under these constraints, the optimization procedure was approached with penalty functions. The first five solutions of the optimization process are listed in **table 8.8** with the corresponding modeled responses and the values of desirability function. An optimal processing condition with a power of 1350 W, a speed of 55 mm/s and a negative tilting angle of 7.5° is clearly suggested because the highest desirability is reached, with no expected buckling distortion; a second optimum with similar outputs would result when considering a power of 1250 W, a speed of 48 mm/s and a negative tilting angle of 2.0°. The first solution is considered for further investigation.

## 8.7 MECHANICAL ASSESSMENT OF THE OPTIMAL PROCESSING CONDITION

The processing parameters of the optimal solution were set to produce new 100 mm long welding beads, to be eventually checked with respect to the referred customer specification; additional specimens to be tested in terms of tensile strength were produced. All of them were examined via NDT, and no

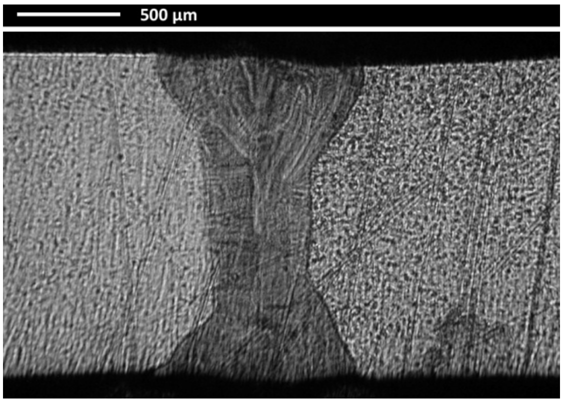

**FIGURE 8.5** – Cross-section in suggested optimum condition; Haynes on the left, Inconel on the right

indications were found. Furthermore, no buckling distortions were noticed and any random cross-section successfully matched the limits for defects and geometry in the referred specification. As an example, a cross-section is shown in **figure 8.5**; mean values of 958 µm for $CW$, 517 µm for $NW$ and 951 µm for $RW$ were measured, within a 1.03 mm$^2$ mean $FZ$. Significant differences are spotted in the cross-section, compared with a non optimal specimen such as the one which is produced in the CCD central point condition (cf. **figure 8.4**): comparable values are now obtained for $CW$ and $RW$ as a consequence of relative high importance having been awarded to the constraint involving the $CW/RW$ factor when optimizing the process.

### 8.7.1 VICKERS MICRO HARDNESS TESTS

An evidence of the HAZ in the etched specimens is clearly noticed via optical microscopy, at the Haynes side only, as shown in **figure 8.6**, and is supposed to have a mean extent of less than 20 µm. Nevertheless, since it has been suggested that metallographic etching is not enough for adequate and persuasive evaluation of the HAZ [128], and in order to embrace the material response at the Inconel side, Vickers micro hardness was tested at mid thickness according to the corresponding normative [65].

A suitable indenting load is required to measure the hardness distribution of the weld. An indenting load of 0.05 kgf was proven to be inappropriate as significant deviations were observed in the testing field due to microstructure variations among the grains [128]; on the other hand, an indenting load of 0.300 kgf resulted in larger indentations which were not capable of

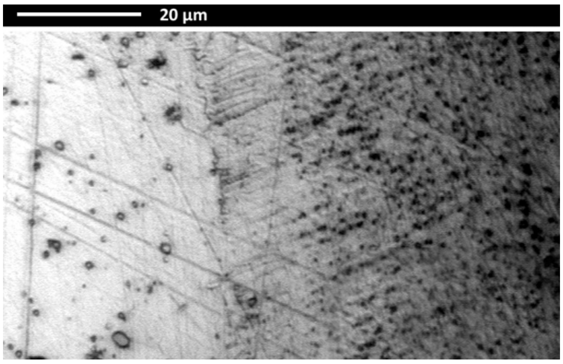

**FIGURE 8.6 –** Heat affected zone at the Haynes side

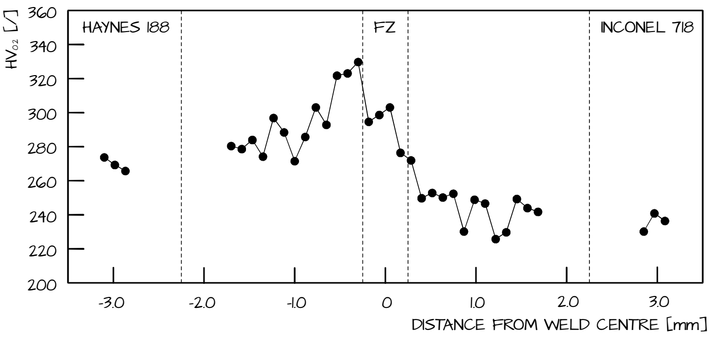

**FIGURE 8.7** – Vickers micro hardness in the cross-section as a function of distance from weld centre

differentiating a narrow expected HAZ, given the requirement to ensure a minimum gap between indentations, to prevent the indented areas to overlap. An indenting load of 0.200 kgf was therefore deemed to be appropriate to adequately satisfy both the needs for reliable and proper measurements. The micro hardness profile across the section is shown in **figure 8.7**. Values of 270 and 240 $HV_{0.2}$ were obtained on average for as-received Haynes and Inconel, respectively. An increasing trend was noticed at the Haynes side towards the fused zone; a 330 $HV_{0.2}$ peak was achieved at the boundary of the fused zone, where peculiar grain morphology had been pointed out via metallographic analyses. The base values were more quickly recovered at the Inconel side instead. As a consequence of mixing, micro hardness in the fused zone itself was lower compared with the Haynes HAZ, although higher compared with the Inconel side anyway.

### 8.7.2 TENSILE TESTS

Analytic results of fatigue fracture surfaces in $CO_2$ welded Inconel 718 specimens had shown failings at HAZ and fusion zone, with crack starting from micro fissures [14].

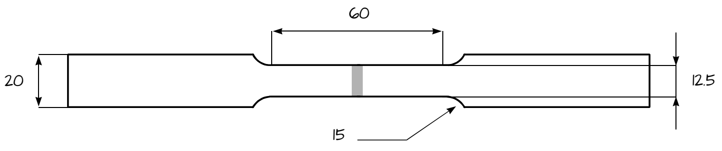

**FIGURE 8.8** – Tensile specimen for aluminum square butt joint testing; dimensions in millimetres

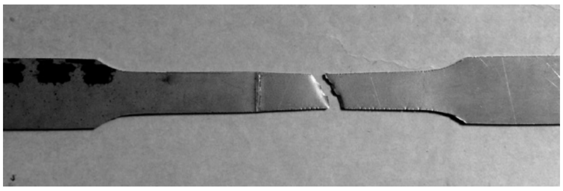

**Figure 8.9** – Fracture in hybrid welded Haynes + Inconel tensile specimen

Since an issue related to possible brittle Laves phase had been highlighted in super alloy welding [12], tensile testing is required to eventually characterize the mechanical quality of the joint. In accordance with AWS specifications [71] as requested for the real application of a hybrid Haynes and Inconel structure, three tensile specimens were milled to a required size, as shown in **figure 8.8**, then tested with 6 MPa/s increasing load at room temperature.

Fracture in the base material occurred, at the Inconel side, 15 mm at least away from the welding bead, as shown in **figure 8.9**. Therefore, the outcome matched the results of Vickers micro hardness testing, where lower values were noticed for Inconel compared with Haynes. Furthermore, the issue of micro fissures and Laves phase in the HAZ is assumed to be overcome; otherwise, fracture would have been experienced in the weld. The corresponding stress-strain diagram is shown in **figure 8.10**; the yield point is clearly spotted. The values of mechanical properties at room temperature in the hybrid structure of welded Haynes and Inconel as obtained from tensile testing are listed in **table 8.8** in comparison with the base metals.

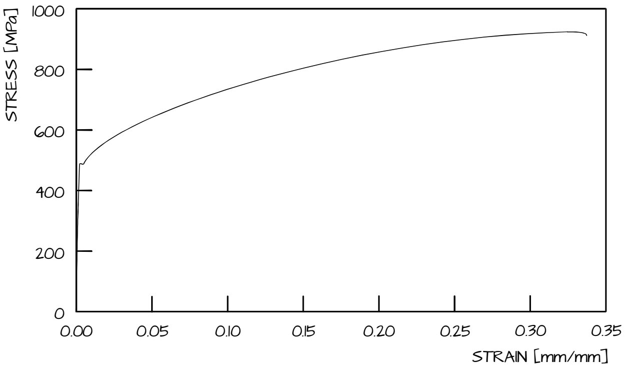

**Figure 8.10** – Stress-strain diagram for hybrid welded Haynes + Inconel specimen

**TABLE 8.8** – Tensile tests output for hybrid welded Haynes + Inconel specimen

| | Haynes 188 | Inconel 718 | Hybrid welded specimen |
|---|---|---|---|
| **Young modulus [GPa]** | 232 | 211 | 218 |
| **Yield strength [MPa]** | 465 | 550 | 470 |
| **Ultimate tensile strength [MPa]** | 945 | 965 | 928 |
| **Elongation [% in 51 mm]** | 52.9 | 30 | 32 |

## 8.8 CONCLUSIONS

Many issues are expected when welding dissimilar metals. Nevertheless, convincing results were provided to give grounds to process improvements in industrial environments because dissimilar autogenous laser beam welding of Haynes 188 and Inconel 718 was successfully addressed with no pre heating, neither need for mechanical finishing. No spatters neither oxidation were detected both on the top- and back-side of the bead, since adequate shielding was provided thanks to a properly designed device for gas supply.

Dimensional limits for indications, specific common defects and shape dimensions, as provided into industrial customer specification, were effectively met. Considerable tolerances were matched with respect to the threshold values for crown and root width. An optimal processing set with a power of 1350 W, a speed of 55 mm/s and a negative beam angle of 7.5° was found. The resulting specimen featured a tight HAZ which is supposed to have an extent of less than 20 µm according to metallographic etching. The eventual mechanical assessment highlighted an increasing trend in Vickers micro hardness at the Haynes side only, whilst mixed values were achieved in the fused zone; furthermore, tensile testing suggested that micro fissures and Laves phase, which are common when using arc or electron beam sources, were overcome as fracture was experienced in the base metal, at the Inconel side, at convincing distance from the joint.

# 9

# DISSIMILAR WELDING HASTELLOY + RENÉ

## 9.1 INTRODUCTION

René 80 is a cast super alloy for stator nozzle guide vanes (NGV), where severe operating conditions are experienced in terms of both tension and compression, low and high cycle fatigue, hot corrosion and oxidation. Hastelloy X is a wrought super alloy instead, and is preferred for transition ducts, combustor cans and flame holders [83]. Both of them are nickel-based; nominal chemical compositions are listed in **table 9.1** and **table 9.2**.

As for any alloy of nickel, chromium and molybdenum, the weld metal which results from fused Hastelloy X does not properly wet the sidewalls of the seam to be welded; when performing arc welding, a control is hence required for both the arc and the filler metal so to prevent incomplete fusion and penetration [134]. With respect to René 80, porosity is expected to be an issue, according to preliminary laser BOP trials. When processing gas turbines for aeronautic applications, Hastelloy X covers are welded on René 80 NGV via

**TABLE 9.1 –** René 80 nominal chemical composition (wt.%)

| Cr | Co | Ti | W | Mo | Al | C | Ni |
|---|---|---|---|---|---|---|---|
| 14 | 5.9 | 5 | 4 | 4 | 3 | 0.15 | Balanced |

**TABLE 9.2 –** Hastelloy X nominal chemical composition (wt.%)

| Cr | Fe | Mo | Co | Mn | Si | W | C | B | Ni |
|---|---|---|---|---|---|---|---|---|---|
| 22 | 18 | 9 | 1.5 | 1 | 1 | 0.6 | 0.10 | 0.008 | Balanced |

electron beam welding. Interest has arisen in alternatively considering laser sources, so common issues with respect to geometry and possible defects must be investigated [135].

## 9.2 ARRANGEMENT OF THE EXPERIMENTAL PLAN

As usual, a 3-factor study with power $P$, welding speed $s$ and focus position $f$ was arranged. Nevertheless, few numbers of samples were available for testing. Therefore, considering the need for two runs at least for statistical significance, only two levels were chosen for each factor; this is not deemed to hamper the study, at a first stage analysis at least. Ranges to be explored for the operating factors were found via ad hoc preliminary trials and are listed in **table 9.3**. Hence, a $2^3$ complete testing plan results; the conditions to be explored are listed in **table 9.4**; a total of 16 welding specimens was produced.

The response variables to be discussed are referred to a generic bead cross-section, as shown in **figure 9.1**. The following outputs were considered: the bead crown width $CW$ and the reinforcement $R$ on the upper surface, the penetration depth $PD$ in the René 80, the bead width at the interface between the materials, both at the Hastelloy X side ($W_{HSTX}$) and the René 80 side ($W_{René}$). Based on the output of preliminary trials, the difference at the interface

**TABLE 9.3** – DOE: factor levels for Hastelloy + René dissimilar welding

| | **-1** | **+1** |
|---|---|---|
| **P [W]** | 1000 | 1200 |
| **s [mm s$^{-1}$]** | 15 | 20 |
| **f [mm]** | -2 | 2 |

**TABLE 9.4** – DOE: Welding conditions to be tested in a complete testing plan

| **Condition** | **P [W]** | **s [mm s$^{-1}$]** | **α [°]** |
|---|---|---|---|
| **1** | 1000 | 15 | -2 |
| **2** | 1000 | 15 | 2 |
| **3** | 1000 | 20 | -2 |
| **4** | 1000 | 20 | 2 |
| **5** | 1200 | 15 | -2 |
| **6** | 1200 | 15 | 2 |
| **7** | 1200 | 20 | -2 |
| **8** | 1200 | 20 | 2 |

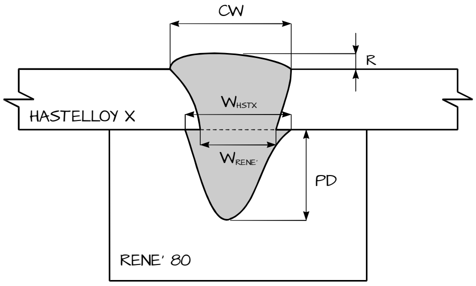
CW
R
HASTELLOY X
$W_{HSTX}$
$W_{RENE'}$
PD
RENE' 80

**FIGURE 9.1** – Cross-section for Hastelloy + René lap welding

position is deemed to be due to occasional improper clamping as well as different thermal properties between the metals being welded. Additionally, the extent of the fused zone $FZ$ was measured; furthermore, analyses on porosity content and possible cracks were carried out and the number of indications $NI$ in the cross-section was considered.

## 8.3 EXPERIMENTAL DETAILS

Apart from being few in number since coming from waste products, the samples of René 80 are complex in geometry as well. A special fixturing, with no practical application in the actual industrial process, was then required for the specific purpose of the experimental plan, in order to reduce any possible starting gap between the materials: as shown in **figure 9.2**, a clamping mask is conveniently screwed on a base plate so to better tighten a 1 mm thick sheet

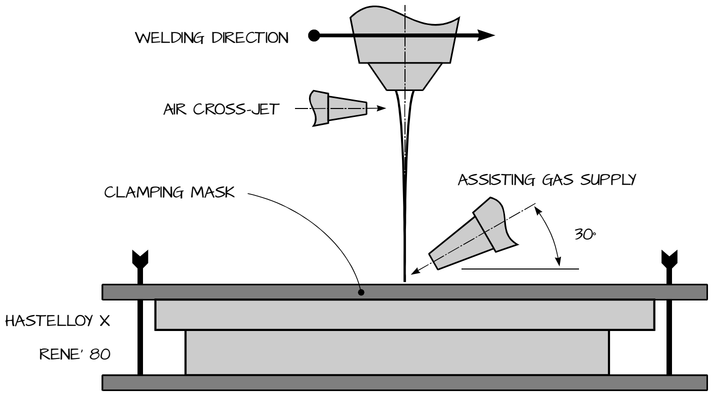
WELDING DIRECTION
AIR CROSS-JET
CLAMPING MASK
ASSISTING GAS SUPPLY
30°
HASTELLOY X
RENE' 80

**FIGURE 9.2** – Laser welding set-up: clamping and bead shielding for Hastelloy + René welding

of Hastelloy X on a sample of René 80; a slot was suitably produced via frontal milling on the upper surface of the mask for the laser beam to reach the metals. A trailing copper nozzle with a tilting angle of 30° to both shield the bead with argon and remove metal plume was employed, with a flow rate of 15 l/min; the diffuser for additional shielding was not needed. Both the Hastelloy and René samples were cleaned with acetone just before welding.

The overlapping welds were then produced in continuous mode emission with a Trumpf Tru-Disk 2002 disk laser (cf. **table 2.2**). The mechanical preparation of the samples was carried out (cf. **table 8.5**); cross-sections were chemical etched for 30 s at room temperature with a 60% hydrochloric, 20% nitric and 20% acetic acid solution [120]. Imperfections were measured via Nikon NIS-Elements imaging software. As waste René samples have complex geometries, a proper longitudinal cut was not feasible for a reliable examination of pores.

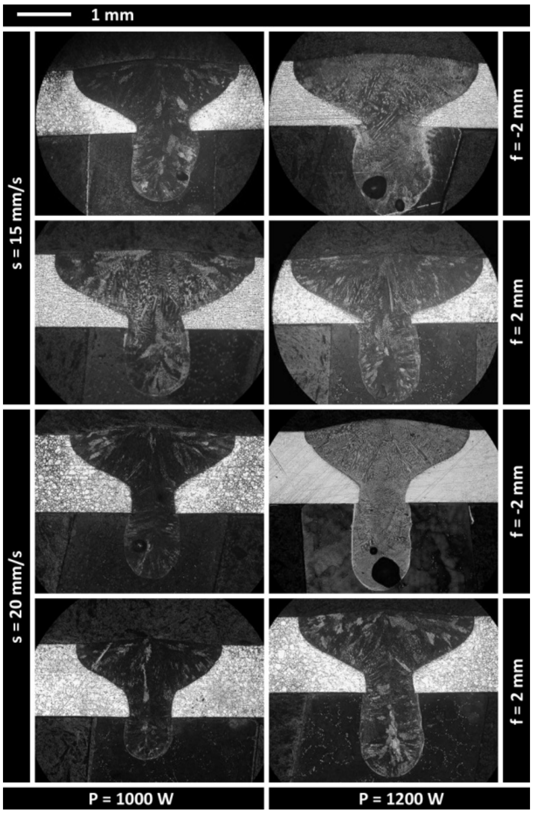

**FIGURE 9.3** – Bead cross-section samples for each testing condition

## 9.4 RESULTS AND DISCUSSION

No spatters were observed on the top-side surface, which also did not show any discoloration, and therefore no oxidation. Examples of the bead cross-sections for each testing condition are shown in **figure 9.3**. The response variables are listed in a comprehensive view in **table 9.5**.

Some preliminary findings are soon drawn. The bead was sometimes found to be asymmetric with respect to the welding axis due to local irregularities of the shape in the samples of René, which produced an unbalanced welding path; for the purpose of the evaluation of the response variables, this was not considered to significantly alter the penetration depth. Furthermore, as expected from preliminary trials, the bead width at the interface was different depending on the material side. As concerning the pores, when present, they were generally found at the René side. With respect to this issue, although referring to the cross-section instead of the longitudinal one, common acceptance criteria of international welding specifications were considered to account of the macro pores: normally, clustered pores having a random geometric distribution combine to bring about a single larger pore when mutual distance is lower than the largest concurrent pore.

**TABLE 9.5 –** DOE: response variables, values for each testing condition

| Cond. | CW [mm] | $W_{HSTX}$ [mm] | $W_{René}$ [mm] | PD [mm] | R [mm] | FZ [mm$^2$] | NI [/] | Pore max size [mm] |
|---|---|---|---|---|---|---|---|---|
| **1** | 2.61 | 0.88 | 1.03 | 1.09 | 0.13 | 3.00 | 3 | 0.38 |
| | 2.56 | 0.71 | 0.82 | 1.02 | 0.10 | 2.67 | 1 | 0.11 |
| **2** | 2.75 | 0.78 | 0.87 | 0.94 | 0.10 | 2.82 | | |
| | 2.75 | 0.72 | 0.83 | 1.05 | 0.11 | 2.84 | | |
| **3** | 2.17 | 0.59 | 0.66 | 0.88 | 0.11 | 2.00 | 1 | 0.18 |
| | 2.10 | 0.61 | 0.71 | 0.93 | 0.10 | 2.03 | 1 | 0.18 |
| **4** | 2.06 | 0.59 | 0.66 | 0.61 | 0.10 | 1.76 | | |
| | 2.08 | 0.65 | 0.71 | 0.60 | 0.05 | 1.72 | 2 | 0.14 |
| **5** | 2.84 | 0.88 | 1.20 | 1.43 | 0.12 | 3.74 | 2 | 0.73 |
| | 2.82 | 0.81 | 1.08 | 1.40 | 0.13 | 3.58 | 1 | 0.20 |
| **6** | 2.88 | 1.03 | 1.33 | 1.40 | 0.10 | 3.96 | | |
| | 2.95 | 0.73 | 0.95 | 1.23 | 0.10 | 3.31 | 1 | 0.21 |
| **7** | 2.30 | 0.65 | 0.77 | 1.21 | 0.16 | 2.56 | 2 | 0.61 |
| | 2.40 | 0.64 | 0.74 | 1.14 | 0.10 | 2.54 | 2 | 0.97 |
| **8** | 2.37 | 0.66 | 0.74 | 1.12 | 0.10 | 2.48 | | |
| | 2.39 | 0.67 | 0.76 | 1.08 | 0.08 | 2.44 | 1 | 0.14 |

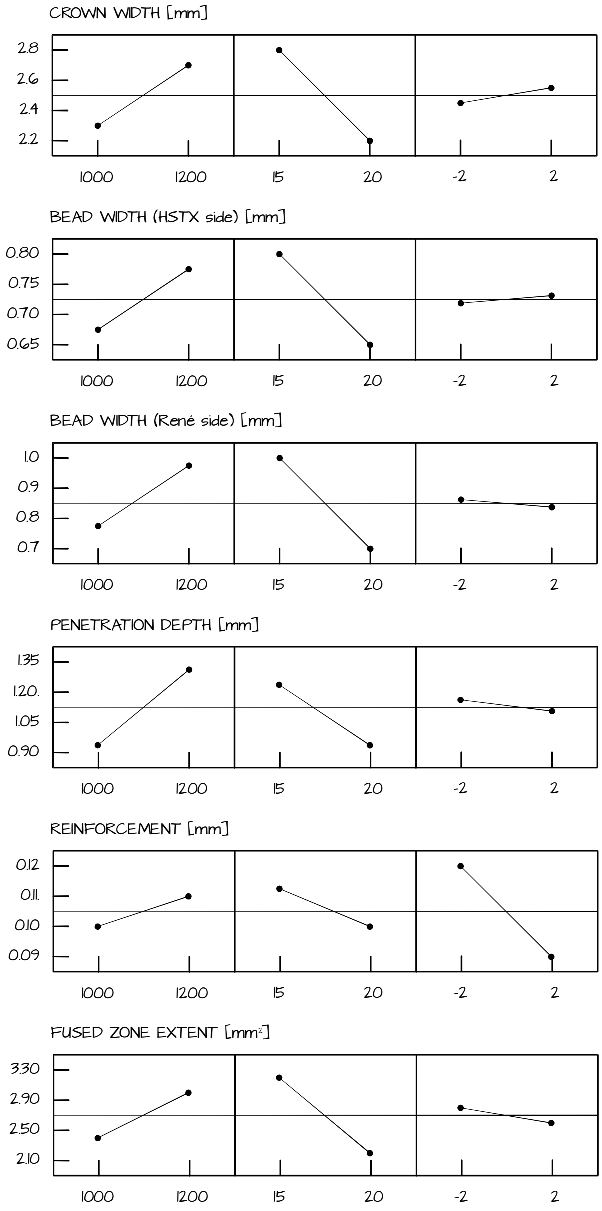

**FIGURE 9.4** – Main effects plot for each response variable

Aiming to a deeper analysis, the effects the governing parameters induce on the response variables were discussed via main effects plots, as shown in **figure 9.4**. Expected basic relationship were confirmed: any increase of power yields a proportional increase in each response.

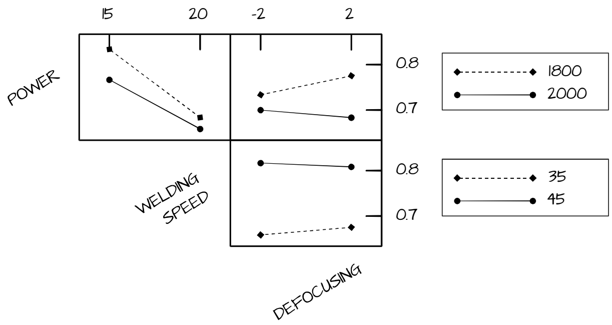

**FIGURE 9.5 –** Interaction plots for bead width at the Hastelloy side

Similarly, any increase in the welding speed results in a corresponding decrease in the referred variable. On the other hand, the effect of the focus position is far less decisive, although a decrease in the reinforcement and the penetration depth was achieved with positive defocusing. The interactions among the governing parameters were not evident from the interaction plots; as an example, the plots for the bead width at the Hastelloy side are shown in **figure 9.5**: since the lines are nearly parallel, only weak interactions are suggested. Therefore, although not theoretically required in a complete testing plan, the central point condition with a power of 1.0 kW, a speed of 17.5 mm/s with focused beam was additionally considered, so to investigate the actual intermediate set-up in the experimental domain. The resulting additional values of the response variables are listed in **table 9.6**.

## 9.5 OPTIMIZATION OF THE RESPONSES

With the addition of the cube central point condition, the ANOVA analysis was performed for both linear and quadratic contributes. The variables to be modeled were chosen among the complete set which had been originally defined. Actually, it makes sense to discuss a model for the penetration depth and the bead width interface, the latter having been referred to the Hastelloy

**TABLE 9.6 –** DOE: response variables, values for the central point condition

| **Cond.** | **CW [mm]** | **$W_{HSTX}$ [mm]** | **$W_{René}$ [mm]** | **PD [mm]** | **R [mm]** | **FZ [$mm^2$]** | **NI [/]** | **Pore max size [mm]** |
|---|---|---|---|---|---|---|---|---|
| **Centre** | 2.21 | 0.84 | 0.96 | 1.46 | 0.20 | 3.11 | 1 | 0.48 |
| | 2.53 | 0.82 | 1.05 | 1.44 | 0.16 | 3.43 | | |

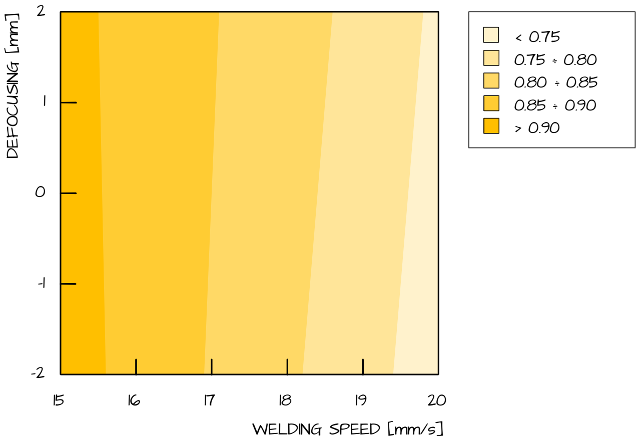

**FIGURE 9.6 –** Contour plot for defocusing against welding speed for bead width at the Hastelloy side

side, being it smaller when compared with the René side, so a conservative approach applies for weld functionality. Porosity would also be worth modeling; nevertheless, this was not feasible since the variable has strong peculiar character of unpredictability.

Once modeled, the variables were further discussed in terms of their response surface. As expected, given the output of the main effects plot regarding the bead width at the Hastelloy side, the focus position has no key effect on the interface. The resulting contour plot of focus position against the speed, which is the most significant parameter according to the ANOVA, is shown in **figure 9.6** when an intermediate power of 1.1 kW is considered: no significant differences in the response variable were recognized, for a given speed.

On the other hand, a number of contour plots must be considered for the penetration depth, which is separately affected by each governing input. The plots are shown in **figure 9.7**; the third additional parameter is taken at its intermediate level within the range. As expected from the main effects plots, the focus position is here crucial. Since a high bead width at the interface and a high penetration depth are needed for the purpose of joint reliability and continuity, an intermediate power in combination with low speed and negative defocusing is clearly suggested for better compliance with possible industrial requirements. This would also act in providing low porosity, since the investigations on the cross-sections had shown an increasing trend in the amount of pores when increasing both the power and the speed.

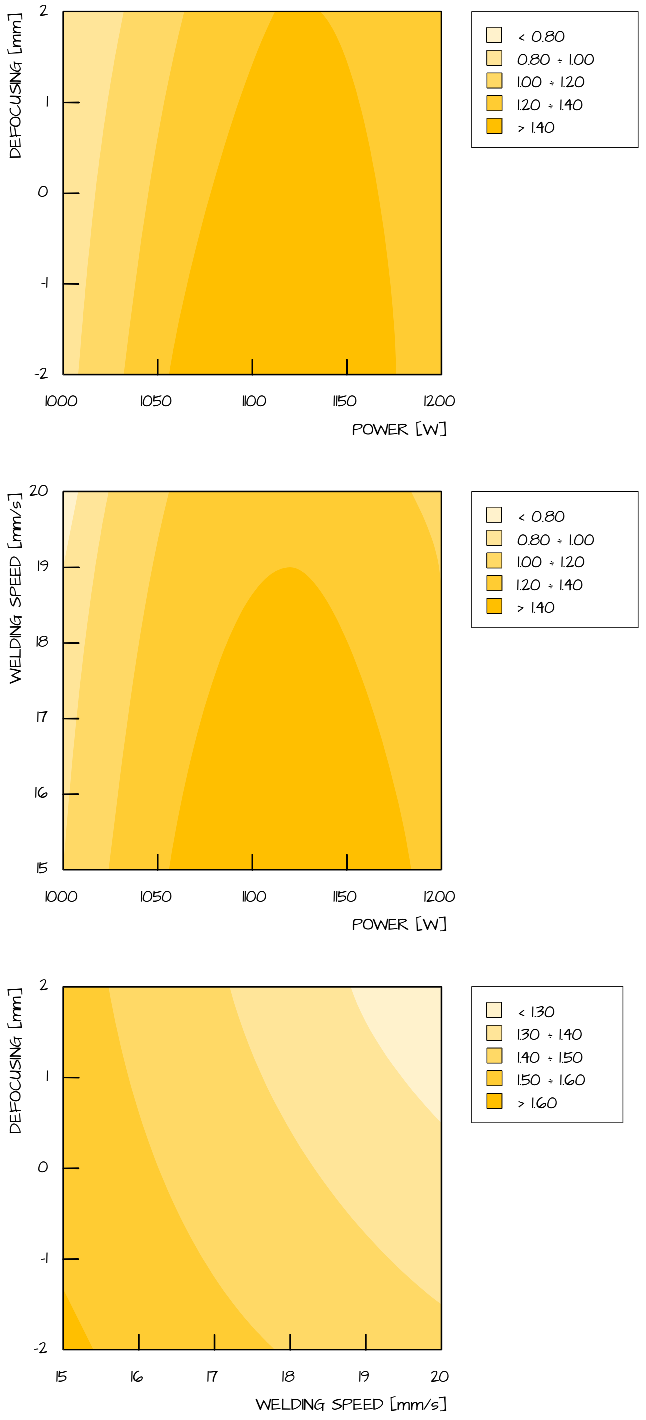

**FIGURE 9.7 –** Contour plots for penetration depth; third governing parameter at its intermediate

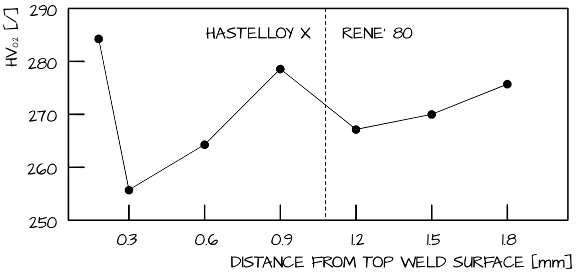

**Figure 9.8** – Vickers micro hardness in the cross-section as a function of distance from top surface

### 9.6 VICKERS MICRO HARDNESS TESTS

An indenting load of 0.2 kgf, for a dwell period of 15 s with a speed of 60 μm/s was employed; 215 and 340 $HV_{0.2}$ resulted for Hastelloy X and René 80, respectively. The measurements within the fused zone were performed in the bead cross-section, on the welding axis, moving from the top weld surface towards the bead tip; a 300 μm step was considered to comply with the referred specification about Vickers testing [67].

As an example, micro hardness trend as resulted in the bead cross-section for the sample in the central point condition is shown in **figure 9.8**. Apart from a single out-layer which is close to the top surface of the weld and is deemed to be due to possible high strength precipitates, quite uniform values of 250 $HV_{0.2}$ on average were achieved in the bulk of the fused zone where convective whirling patterns are in place [5].

### 9.7 CONCLUSIONS

Although few tests were possible on complex samples, coming them from waste products, convincing outcomes were achieved in order to suggest the use of laser beam welding as an alternative to electron beam welding for dissimilar joining of Hastelloy X on René 80 for NGV application.

Preliminary trials were needed to find a proper processing range as well as to properly fix a specific device for bead shielding and sample clamping. The bead was sometimes found to be asymmetric with respect to the welding axis; its width at the interface was different depending on the material side; when present, pores were generally found at the René side and common acceptance criteria of international welding specifications were considered to account of them. The bead features were referred to, with the aim of providing a window to combine the power, the welding speed and the focus position so to comply with possible industrial requirements on the bead width at the interface as well as on the penetration depth in the René. The suggested welding condition is expected to also provide a low content of porosity. Homogenization of the metals in the fused zone is deemed to take place according to Vickers micro hardness.

## ACKNOWLEDGEMENTS

My adviser and supervisor Prof. Fabrizia Caiazzo for wholehearted support, guidance and enthusiasm; Prof. Vincenzo Sergi for additional help and attention to detail.

Prof. Stefano Riemma and Prof. Alessandra Amendola as Ph.D. coordinators.

The team at the University of Salerno: Eng. Francesco Cardaropoli and Eng. Gaetano Corrado for co-working on the subject of this Ph.D. thesis; Dr. Roberto Criscuolo for practical suggestions, milling of pre welding sample and preparation of post welding tensile specimens.

Eng. Luigi Cuccaro, Eng. Gaetano De Chiara, Eng. Giuseppe Petrone, Eng. Angelo Schipani and Mr. Salvatore Cinque of Avio S.p.A. in Pomigliano d'Arco for valuable support, technical assistance and non destructive tests on super alloys welding.

Dr. Michele Di Foggia and Eng. Otello Natale of Europea Microfusioni Aerospaziali S.p.A. in Morra De Sanctis for X-ray tests.

Dr. Antonio Vecchione and Dr. Rosalba Tatiana Fittipaldi of CNR-SPIN U.O.S Salerno for energy dispersive spectrometry on aluminum alloys.

Prof. Gabriele Cricrì, Eng. Michele Perrella and Eng. Marcello Lepore of Industrial Department of the University of Salerno for tensile tests.

Dr. Rüdiger Paschotta of RP Photonics Consulting GmbH and Dr. Jochen Speiser of Institut für Strahlwerkzeuge for valuable help on the theoretical principles of disk laser; Mr. David Havrilla of Trumpf Inc. for a detailed insight into comparing thin disk versus fibre sources.

Eng. Ruben Greco, Eng. Federica Palma and Eng. Emiliano Pelosi for strong contribution to the results on these topics with their thesis work.

All of the colleagues at technical meetings and international conferences, as well as anonymous reviewers for significant remarks to improve this research and related papers.

# REFERENCES

[1] P. WANJARA, M. BROCHU, "Characterization of electron beam welded AA 2024", *Vacuum*, vol. 85, pp. 268-282 (2010).

[2] W. W. DULEY, *Laser welding*, John Wiley & Sons, New York (1998).

[3] V. ALFIERI, F. CAIAZZO, F. CARDAROPOLI, V. SERGI, "Investigation on porosity content in 2024 aluminum alloy welding by Yb:YAG disk laser", *Advanced Material Research*, vols. 383-390, pp. 6265-6269 (2012).

[4] V. ALFIERI, F. CAIAZZO, F. CARDAROPOLI, V. SERGI, "Porosity evolution in aluminum alloy 2024 BOP and butt defocused welding by Yb:YAG disk laser", *Engineering Review*, vol. 31, n. 2, pp. 125-132 (2011).

[5] W. M. STEEN, J. MAZUMDER, *Laser Material Processing*, Springer-Verlag, London (2010).

[6] F. CAIAZZO, F. CURCIO, G. DAURELIO, F. MEMOLA CAPECE MINUTOLO, "Ti6Al4V sheets lap and butt joints carried out by CO2 laser: mechanical and morphological characterization", *Journal of Materials Processing Technology*, vol. 149, pp. 546–552 (2004).

[7] S. CHEN, L. LI, Y. CHEN, J. HUANG, "Joining mechanism of Ti/Al dissimilar alloys during laser welding-brazing process", *Journal of Alloys and Compounds*, vol. 509, pp. 891–898 (2011).

[8] M. KREIMEYER, F. WAGNER, F. VOLLERTSEN, "Laser processing of aluminum-titanium-tailored blanks", *Optics and Lasers in Engineering*, vol. 43, pp. 1021-1035 (2005).

[9] E. CAPELLO, *Le lavorazioni industriali mediante laser di potenza*, Maggioli Editore, Santarcangelo di Romagna, Rimini (2008).

[10] J. N. PIRES, A. LOUREIRO, G. BÖLMSJO, *Welding robots: technology, system issues and applications*, Springer-Verlang, London (2006).

[11] S. KALPAKJIAN, S. R. SCHMID, *Manufacturing Engineering and Technology*, Pearson Education Canada, Don Mills, Ontario (2009).

[12] G. D. JANAKI RAM, A. VENUGOPAL REDDY, K. PRASAD RAOB, G. M. REDDY, J. K. SARIN SUNDARD, "Microstructure and tensile properties of Inconel 718 pulsed Nd:YAG laser welds", *Journal of Materials Processing Technology*, vol. 167, pp. 73-82 (2005).

[13] A. RUGGIERO, L. TRICARICO, A. G. OLABI, K. Y. BENYOUNIS, "Weld-bead profile and costs optimisation of the $CO_2$ dissimilar laser welding process of low carbon steel and austenitic steel AISI316", *Optics & Laser Technology*, vol. 43, pp. 82-90 (2011).

[14] J. K. HONG, J. H. PARK, N. K. PARK, I. S. EOM, M. B. KIM, C. Y. KANG, "Microstructures and mechanical properties of Inconel 718 welds by $CO_2$ laser welding", *Journal of Materials Processing Technology*, vol. 201, pp. 515–520 (2008).

[15] Y. KAWAHITO, M. KITO, S. KATAYAMA, "In-process monitoring and adaptive control for laser spot and seam welding of pure titanium", *Journal of Laser Micro/Nanoengineering*, vol. 1, n. 3, pp. 269-274 (2006).

[16] T. SIBILLANO, A. ANCONA, P. M. LUGARÀ, C. GIANCASPRO, "TR welding opto control for laser welding: from an innovative idea to an industrial reality", Proceedings of the 9th AITeM Conference, *Enhancing the Science of Manufacturing*, Torino (2009).

[17] AMERICAN WELDING SOCIETY, *Laser welding and cutting safety*, Doral (2009).

[18] *D70 Technical guide*, Trumpf Gruppe, Schramberg (2008).

[19] A. ISIDORI, *Il mondo dei robot: i protagonisti dell'automazione industriale*, Giunti Barbera, Firenze (1986).

[20] A. Geisen, J. Speiser, “Fifteen years of work on thin-disk lasers: results and scaling laws”, *IEEE Journal of Selected Topics in Quantum Electronics*, vol. 13, n. 3, pp. 598-609 (2007).

[21] “Thin disk laser technology”, L.O.G. Europe, lotoriel.co.uk.

[22] H. Schlüter, “Thin-disk-laser power scaling improves welding efficiency”, *Laser Focus World*, PennWell Corporation, laserfocusworld.com (2006).

[23] R. Paschotta, *Encyclopedia of laser physics and technology*, Wiley-VCH, Berlin (2008).

[24] *Encyclopaedia Britannica*, Encyclopaedia Britannica Inc. (2012).

[25] D. Halliday, R. Resnick, *Fundamentals of Physics*, John Wiley & Sons, New York (2010).

[26] T. Scheller, A. Bastick, M. Griebel, “Advantages of fibre lasers in 3d metal cutting and welding applications supported by a beam in motion (BIM) beam delivery system”, Proceedings of *SPIE 8239*, San Francisco (2012).

[27] B. Hunter, K. Leong, C. Miller, J. Golden, R. Glesias, P. Laverty, “Understanding high-power fiber-optic laser beam delivery”, *Journal of Laser Application*, vol. 8, pp. 307–316 (1996).

[28] CVI Melles Griot, “Gaussian beam propagation”, *All things photonics - The CVI Melles Griot technical guide*, vol. 2, n. 1, pp. 1-14 (2009).

[29] ISO Standard 11146-2:2005, *Lasers and laser-related equipment - Test methods for laser beam widths, divergence angles and beam propagation ratios* (2005).

[30] F. Dausinger, “Benefit of enhanced focusability of new YAG-lasers”, Proceedings of *EALA*, Bad Nauheim, Frankfurt (2002).

[31] A. Kemp, G. Valentine, D. Burns, “Progress towards high-power, high-brightness neodymium-based thin-disk lasers”, *Progress in Quantum Electronics*, vol. 28, pp. 305-344 (2004).

[32] N. P. Barnes, “Solid-state lasers from an efficiency perspective”, *IEEE Journal of Selected Topics in Quantum Electronics*, vol. 13, n. 3, pp. 435-447 (2007).

[33] A. Giesen, “Results and scaling laws of thin disk lasers”, Proceedings of *SPIE 5332, Solid State Lasers: Technology and Devices*, Bellingham (2004).

[34] M. Javadi-Dashcasan, F. Hajiesmaeilbaigi, H. Razzaghi, M. Mahdizadeh, M. Moghadam, “Optimizing the Yb:YAG thin disc laser design parameters”, *Optics Communications*, vol. 281, pp. 4753-4757 (2008).

[35] D. Havrilla, V. Rominger, M. Holzer, T. Harrer, A. Andreev, “Advanced welding techniques with optimized accessories for high brightness 1 µm lasers”, Proceedings of *SPIE 8603*, San Francisco (2013).

[36] X. Jin, P. Berger, T. Graf, “Multiple reflections and Fresnel absorption of gaussian laser beam in an actual 3d keyhole during deep-penetration laser welding”, *International Journal of Optics*, vol. 39, n. 21 (2012).

[37] Y. Cheng, X. Jin, S. Li, L. Zeng, “Fresnel absorption and inverse bremsstrahlung absorption in 3d keyhole during deep penetration $CO_2$ laser welding of aluminum 6016”, *Optics & Laser Technology*, vol. 44, pp. 1426-1436 (2012).

[38] P. Okon, G. Dearden, K. Watkins, M. Sharp, P. French, “Laser welding of aluminum alloy 5083”, Proceedings of *ICALEO 2002*, Scottsdale (2002).

[39] F. Caiazzo, E. Mastrocinque, G. Corrado, V. Sergi, “Regression modeling to predict the geometrical features of Ti6Al4V thin sheets butt joints welded by disk laser”, Proceedings of *SPIE 8433*, Bruxelles (2012).

[40] T. Klein, M. Vicanek, J. Kroos, I. Decker, G. Simon, “Oscillations of the keyhole in penetration laser beam welding”, *Journal of Physics D: Applied Physics*, vol. 27, pp. 2023-2030 (1994).

[41] J. KROOS, U. GRATZKE, G. SIMON, “Towards a self-consistent model of the keyhole in laser beam welding”, *Journal of Physics D: Applied Physics*, vol. 26, pp. 474-480 (1993).

[42] J. GRESES, P. A. HILTON, C. Y. BARLOW, W. M. STEEN, “Spectroscopic studies of plume/plasma in different gas environments”, Proceedings of *ICALEO 2001*, Jacksonville (2001).

[43] M. SANTOCHI, F. GIUSTI, *Tecnologia meccanica e studi di fabbricazione*, Casa Editrice Ambrosiana, Milano (2000).

[44] S. KATAYAMA, Y. KAWAHITO, M. MIZUTANI, “Elucidation of laser welding phenomena and factors affecting weld penetration and welding defects”, *Physics Procedia*, vol. 5, pp. 9-17 (2010).

[45] K. H. LEONG, K. R. SABO, P. G. SANDERS, W. J. SPAWR, “Laser welding of aluminum alloys”, Proceedings of *SPIE 1997, Lasers as Tools for Manufacturing II*, San Jose (1997).

[46] F. SEAMAN, “Role of shielding gas in laser welding”, technical paper MR77-982, Society of Manufacturing Engineers, Dearborn (1977).

[47] D. GREVEY, P. SALLAMAND, E. CICALA, S. IGNAT, “Gas protection optimization during Nd:YAG laser welding”, *Optics & Laser Technology*, vol. 37, pp. 647-651 (2005).

[48] X. CAO, M. JAHAZI, “Effect of welding speed on butt joint quality of Ti-6Al-4V alloy welded using high power Nd:YAG laser”, *Laser Optics in Engineering*, vol. 47, n. 11, pp. 1231-1241, (2009).

[49] M. PASTOR, H. ZHAO, R. P. MARTUKANITZ, T. DEBROY, “Porosity, underfill and magnesium loss during continuous wave Nd:YAG laser welding of thin plates of aluminum alloys 5182 and 5754”, *Welding Journal*, vol. 78, n. 12, pp. 207-216 (1999).

[50] Y. KAWAHITO, M. MIZUTANI, S. KATAYAMA, “Investigation of high-power fiber laser welding phenomena of stainless steel”, *Transactions of Joining and Welding Research Institute*, vol. 36, n. 2, pp. 11-16 (2007).

[51] Y. LIAO, M. YU, “Effects of laser beam energy and incident angle on the pulse laser welding of stainless steel thin sheet”, *Journal of Materials Processing Technology*, vol. 190, pp. 102-108 (2007).

[52] EN ISO 6520-1, *Welding and allied processes - Classification of geometric imperfections in metallic materials - Part 1: Fusion welding* (2007).

[53] G. SONG, L. LIU, P. WANG, “Overlap welding of magnesium AZ31B sheets using laser-arc hybrid process”, *Materials Science and Engineering A*, vol. 429, n. 1-2, pp. 312-219 (2006).

[54] L. CEDERQVIST, P. REYNOLDS, “Factors affecting the properties of friction stir welded aluminum lap joints”, *Welding Journal*, vol. 80, n. 12, pp. 281-287 (2001).

[55] D. CERNIGLIA, K. Y. JHANG, B. B. DJORDJEVIC, “Non-contact ultrasonic testing of aircraft lap joints”, Proceedings of *15th World Conference on NDT*, Roma (2000).

[56] EN 970, *Non-destructive examination of fusion welds - Visual examination* (1997).

[57] P. E. MIX, *Introduction to non destructive testing - A training guide*, John Wiley & Sons, Hoboken (2005).

[58] EN ISO 23277, *Non-destructive testing of welds - Penetrant testing* (2006).

[59] EN 1435, *Non-destructive testing of welds - Radiographic testing of welded joints* (2004).

[60] EN 12517-1, *Non-destructive testing of welds - Part 1: Evaluation of welded joints in steel, nickel, titanium and their alloys by radiography - Acceptance levels* (2006).

[61] EN 12517-2, *Non-destructive testing of welds - Part 2: Evaluation of welded joints in aluminum and its alloys by radiography - Acceptance levels* (2008).

[62] *Buyer's guide 2010 - Materials preparation and analysis*, Buehler Ltd, Lake Bluff (2010).

[63] L. M. GAMMON, R. D. BRIGGS, J. M. PACKARD, K. W. BATSON, R. BOYER, C. W. DOMBY, “Metallography and microstructures of titanium and its alloys”, *ASM Handbook*, vol. 9, pp. 899-917 (2004).

[64] G. F. VANDER VOORT, *Metallography: principles and practice*, McGraw-Hill, reprinted by ASM International, Materials Park (1999).

[65] EN ISO 9015-2, *Destructive tests on welds in metallic materials - Hardness test: Part 2 - Micro hardness testing on welded joints* (2011).

[66] EN ISO 13919-2, *Welding - Electron and laser beam welded joints - Guidance on quality levels for imperfections - Part 2: aluminum and its weldable alloys* (2003).

[67] EN ISO 6507-1, *Metallic materials - Vickers hardness test - Part 1: test method* (2005).

[68] B. K. AGARWAL, *X-ray spectroscopy*, Springer-Verlag, Berlin (1991).

[69] R. GRIEKEN, A. MARKOWICZ, *Handbook of X-ray spectrometry*, CRC Press, Taylor & Francis Group, Boca Raton (2002).

[70] EN ISO 4136, *Destructive tests on weld in metallic materials - Transverse tensile test* (2011).

[71] AWS B4.0, *Standard methods for mechanical testing of welds* (2007).

[72] EN ISO 6892-1, *Metallic materials - Tensile testing: method of test at ambient temperature* (2009).

[73] D. C. MONTGOMERY, *Design and Analysis of Experiment*, McGraw Hill, New York (2005).

[74] V. CZITROM, “One-factor-at-a-time versus designed experiments”, *The American Statistician*, vol. 53, n. 2, pp. 126-131 (1999).

[75] M. J. ANDERSON, P. J. Whitcomb, *Practical tools for effective experimentation*, Productivity Press, Portland (2000).

[76] K. Y. BENYOUNIS, A. G. OLABI, “Optimization of different welding processes using statistical and numerical approaches - A reference guide”, *Advances in Engineering Software*, vol. 6, pp. 483-496 (2008).

[77] R. H. MYERS, *Classical and modern regression with applications*, Duxbury Press, Boston (1990).

[78] R. G. MILLER, *Beyond ANOVA, basic of applied statistics*, John Wiley & Sons, New York (1985).

[79] G. DERRINGER, R. SUICH, “Simultaneous optimization of several response variables”, *Journal of Quality Technology*, vol. 12, n. 4, pp. 214-219 (1980).

[80] F. CAIAZZO, V. ALFIERI, F. CARDAROPOLI, V. SERGI, “Bead characterization of disk-laser butt welding of thin AA 2024 sheet”, Proceedings of *SPIE 8239*, San Francisco (2012).

[81] M. J. ANDERSON, P. J. WHITCOMB, *RSM Simplified: optimizing processes using response surface methods for design of experiments*, CRC Press, Taylor & Francis Group, Boca Raton (2005).

[82] W.S. MILLER, L. ZHUANG, J. BOTTEMA, A.J. WITTEBROOD, P. DE SMET, A. HASZLER, A. VIEREGGE, “Recent development in aluminium alloys for the automotive industry”, *Materials Science and Engineering A*, vol. 280, n. 1, pp. 37-49 (2000).

[83] J. R. DAVIS, *Aluminum and Aluminum Alloys*, ASM International, Materials Park (1993).

[84] H. AYDIN, A. BAYRAM, A. UGUZ, K. S. AKAY, “The effect of post-weld heat treatment on the mechanical properties of 2024-T4 friction stir-welded joints”, *Materials and Design*, vol. 31, p. 2568–2577 (2010).

[85] F. MALEK GHAINI, M. SHEIKHI, M. J. TORKAMANY, J. SABBAGHZADEH, “The relation between liquation and solidification cracks in pulsed laser welding of 2024 aluminium alloy”, *Materials Science and Engineering A*, vol. 519, p. 167–171 (2009).

[86] R. V. Preston, H. R. Shercliff, P. J. Withers, S. Smith, “Phisically-based constitutive modelling of residual stress development in welding of aluminium alloy 2024”, *Acta Materialia*, vol. 52, pp. 4973-4983 (2004).

[87] S. J. Kalita, “Microstructure and corrosion properties of diode laser melted friction stir weld of aluminum alloy 2024 T351”, *Applied Surface Science*, vol. 257, n. 9, pp. 3985-3997 (2011).

[88] F. Caiazzo, V. Alfieri, F. Cardaropoli, V. Sergi, “Characterization of lap joints laser beam welding of thin AA 2024 sheets with Yb:YAG disk-laser”, Proceedings of *SPIE 8433*, Bruxelles (2012).

[89] V. Alfieri, F. Caiazzo, F. Cardaropoli, V. Sergi, “Issues in disk-laser key-hole welding of 2024 aluminum alloy”, *Frontiers in Aerospace Engineering*, vol. 1, n. 1, pp. 37-45 (2012).

[90] M. Kraetzsch, J. Standfuss, A. Klotzbach, J. Kaspar, B. Brenner, E. Beyer, “Laser beam welding with high-frequency beam oscillation: welding of dissimilar materials with brilliant fiber lasers”, *Physics Procedia*, vol. 12, pp. 142-149 (2011).

[91] D. Zhang, X. Jin, L. Gao, H. Joo, K. Lee, “Effect of laser-arc hybrid welding on fracture and corrosion behaviour of AA6061-T6 alloy”, *Materials Science and Engineering A*, vol. 528, pp. 2748-2754 (2011).

[92] B. Hu, I. M. Richardson, “Autogenous laser keyhole welding of aluminium alloy 2024”, *Journal of Laser Application*, vol. 17, n. 2, pp. 70-80 (2005).

[93] A. Ancona, T. Sibillano, L. Tricarico, R. Spina, P. M. Lugarà, G. Basile, S. Schiavone, “Comparison of two different nozzles for laser beam welding of AA5083 aluminum alloy”, *Journal of Materials Processing Technology*, vol. 164-165, pp. 971-977 (2005).

[94] T. Sibillano, A. Ancona, V. Berardi, E. Schingaro, G. Basile, P. M. Lugarà, “A study of the shielding gas influence on the laser beam welding of AA 5083 aluminium alloys by in-process spectroscopic investigation”, *Optics and Lasers in Engineering*, vol. 44, n. 10, pp. 1039-1051 (2006).

[95] F. Cardaropoli, V. Alfieri, F. Caiazzo, V. Sergi, G. Campanile, “Laser welding of aluminum alloy AA 2024 by Yb:YAG disk laser”, Proceedings of *10th AITeM Conference, Enhancing the Science of Manufacturing*, Napoli.

[96] M. Nerádová, P. Kovačócy, “Welding of aluminum using a pulsed Nd:YAG laser”, *Acta Polytechnica*, vol. 50, n. 6, pp. 66-69 (2010).

[97] J. Bartl, M. Baranek, “Emissivity of aluminium and its importance for radiometric measurement”, *Measurement of Physical Quantities*, vol. 4, n. 3, pp. 31-36 (2004).

[98] J. M. Sanchez-Amaya, T. Delgado, L. Gonzalez-Rovira, F. J. Botana, “Laser welding of aluminium alloys 5083 and 6082 under conduction regime”, *Applied Surface Science*, vol. 255, n. 23, pp. 9512-9521 (2009).

[99] M. A. Sutton, B. Yang, A.P. Reynolds, R. Taylor, “Microstructural studies of friction stir welds in 2024-T3 aluminum”, *Materials Science and Engineering A*, vol. 323, pp. 160-166 (2002).

[100] A. Haboudou, P. Peyre, A. B. Vannes, G. Peix, “Reduction of porosity content generated during Nd:YAG laser welding of A356 and AA5083 aluminium alloys”, Materials Science and Engineering A, vol. 363, pp. 40-52 (2003).

[101] H. Zhao, T. DebRoy, “Macroporosity free aluminum alloy weldments through numerical simulation of key-hole mode laser welding”, *Journal of Applied Physics*, vol. 93, n. 12, pp. 10089-10096 (2003).

[102] C. Y. Chen, H. J. Liu, J. C. Feng, “Effect of post-weld heat treatment on the mechanical properties of 2219-O friction stir welded joints”, *Journal of Material Science*, vol. 41, pp. 297-299 (2006).

[103] A. D. Ludovico, G. Daurelio, L. A. C. De Filippis, A. Scialpi, F. Squeo, “Laser welding of the AA 2024-T3 aluminium alloy by using two different laser sources”, Proceedings of *SPIE 5777, XV International symposium on gas flow, chemical lasers, and high-power lasers*, Prague (2005).

[104] W. S. Chang, S. R. Rajesh, C. K. Chun, H. J. Kim, “Microstructure and mechanical properties of hybrid laser-friction stir welding between AA6061-T6 Al alloy and AZ31 Mg alloy”, *Journal of Materials Science and Technology*, vol. 27, n. 3, pp. 199-204 (2011).

[105] Y. J. Chao, X. Qi, W. Tang, “Heat transfer in friction stir welding - Experimental and numerical studies”, *Journal of Manufacturing Science and Engineering*, vol. 125, pp. 138-145 (2003).

[106] M. J. Donachie, *Titanium: a technical guide*, ASM International, Materials Park (2000).

[107] M. S. F. Lima, “Laser beam welding of titanium nitride coated titanium using pulse-shaping”, *Materials Research*, vol. 8, pp. 323-328 (2005).

[108] F. Cardaropoli, V. Alfieri, F. Caiazzo, V. Sergi, “Manufacturing of porous biomaterials for dental implant applications through Selective Laser Melting”, *Advanced Materials Research*, Vol. 535-537, pp. 1222-1229 (2012).

[109] Z. Sun, D. Pan, W. Zhang, “Correlation between welding parameters and microstructures in TIG, plasma and laser welded Ti-6Al-4V”, Proceedings of *6th International Conference on Trends in Welding Research*, Pine Mountain (2002).

[110] J. Mazumder, W. M. Steen, “Welding of Ti-6Al-4V by continuous wave $CO_2$ laser”, *Metal Construction*, vol. 12, n. 9, pp. 423-427 (1980).

[111] E. Akman, A. Demir, T. Canel, T. Sinmazçelik, “Laser welding of Ti6Al4V titanium alloys”, *Journal of Materials Processing Technology*, vol. 209, pp. 3705-3713 (2009).

[112] E. Mastrocinque, G. Corrado, F. Caiazzo, N. Pasquino, V. Sergi, “Effect of defocusing on bead-on-plate of Ti6Al4V by Yb:YAG disk laser”, *Advanced Materials Research*, Vol. 383-390, pp. 6258-6264 (2012).

[113] S. H. Wang, M. D. Wei, L. W. Tsay, “Tensile properties of LBW welds in Ti-6Al-4V alloy at evaluated temperatures below 450 °C”, *Materials Letters*, vol. 57, pp. 1815-1823 (2003).

[114] E. Mastrocinque, G. Corrado, F. Caiazzo, N. Pasquino, V. Sergi, F. Acerra, “Disk laser welding of Ti6Al4V alloy”, Proceeding of *21st International Conference on Production Research*, Stuttgart (2011).

[115] EN ISO 13919-1, *Welding - Electron and laser beam welded joints - Guidance on quality levels for imperfections - Part 1: steel* (1997).

[116] L. W. Tsay, C. Y. Tsay, “The effect of microstructures on the fatigue crack growth in Ti-6Al-4V laser welds”, *International Journal of Fatigue*, vol. 19, n. 10, pp. 713-720 (1997).

[117] S. Wang, X. Wu, “Investigation on the microstructure and mechanical properties of Ti-6Al-4V alloy joints with electron beam welding”, *Materials and Design*, vol. 36, pp. 663-670 (2012).

[118] T. Ahmed, H. Rack, “Phase transformation during cooling in α+β titanium alloys”, *Materials Science and Engineering A*, vol. 243, pp. 206-211 (1998).

[119] D. J. Tillack, “Welding superalloys for aerospace applications”, *Welding Journal*, vol. 1, pp. 28-32 (2007).

[120] J. R. Davis, *Nickel, Cobalt and their Alloys*, ASM International, Materials Park (2000).

[121] R. C. Reed, *The Superalloys, Fundamentals and Applications*, Cambridge University Press, New York (2006).

[122] F. Zapirain, F. Zubiri, F. Garciandìa, I. Tolosa, S. Chueca, A. Goiria, “Development of laser welding of Ni based superalloys for aeronautic engines applications (Experimental process and obtained properties)”, *Physics Procedia*, vol. 12, pp. 105-112 (2011).

[123] S. Petronic, S. Drecun-Nesic, A. Milosavljevic, A. Sedmak, M. Popovic, A. Kovacevic, "Microstructure changes of nickel-base superalloys induced by interaction with femtosecond laser beam", *Acta Physica Polonica A*, vol. 116, n. 4, pp. 550-552 (2009).

[124] R. Schafrik, R. Sprague, "Superalloy technology - A perspective on critical innovations for turbine engines", *Key Engineering Materials*, vol. 380, pp. 113-134 (2008).

[125] M. J. Donachie, S. J. Donachie, *Superalloys: a technical guide*, ASM International, Materials Park (2002).

[126] S. Gobbi, Li Zhang, J. Norris, K. H. Richter and J. H. Loreau, "High power CO2 and Nd-YAG laser welding of wrought Inconel 718", *Journal of Materials Processing Technology*, vol. 56, pp. 333-345 (1996).

[127] B. S. Yilbas, S. Akthar, "Laser welding of Haynes 188 alloy sheet: thermal stress analysis", *International Journal of Advanced Manufacturing Technology*, vol. 56, pp. 115-124 (2011).

[128] C. A. Huang, T. H. Wang, C. H. Lee, W. C. Han, "A study of the heat-affected-zone (HAZ) of an Inconel 718 sheet welded with electron-beam welding (EBW)", *Materials Science and Engineering A*, vol. 398, pp. 275-281 (2005).

[129] J. Gordine, "Some problems in welding Inconel 718", *Welding Journal*, vol. 11, pp. 480-484 (1971).

[130] A. Lingenfelter, "Welding of Inconel 718: a historical review", Proceedings of *Superalloy 718 Conference*, Warrendale (1989).

[131] W. J. Mills, "Effect of heat treatment on the tensile and fracture toughness behaviour of Inconel 718 weldments", *Welding Journal*, vol. 8 (1984).

[132] A. T. Egbewande, R. A. Buckson, O. A. Ojo, "Analysis of laser beam weldability of Inconel 718 superalloy", *Materials Characterization*, vol. 61, pp. 569-574 (2010).

[133] H. Y. Li, Z. W. Huang, S. Bray, G. Baxter, P. Bowen, "High temperature fatigue of friction welded joints in dissimilar nickel based superalloys", *Materials Science and Technology*, vol. 23, n. 12, pp. 1408-1418 (2007).

[134] F. Cardaropoli, V. Alfieri, F. Caiazzo, V. Sergi, "Hastelloy X and Haynes 188 laser welding by Yb:YAG disk laser", Proceeding of *9th International Conference on Advanced Manufacturing Systems and Technology, AMST 11*, Mali Losinj (2011).

[135] F. Caiazzo, G. Corrado, V. Alfieri, V. Sergi, L. Cuccaro, "Disk-laser welding of Hastelloy X cover on René 80 turbine stator blade", Proceeding of *High Power Laser Systems & Applications, HPLS&A 2012*, Istanbul (2012).